The Dissertation Committee for Alexander Michael Jentsch
certifies that this is the approved version of the following dissertation:

Studying Heavy-Flavor Quark Jets Using D^0+hadron Two-Dimensional Angular Correlations in Au+Au Collisions at $\sqrt{s_{\mathrm{NN}}} = 200$ GeV

Committee:

Christina Markert, Supervisor

Robert L. Ray, Co-Supervisor

Peter Onyisi

Timothy Andeen

Derek Haas

Studying Heavy-Flavor Quark Jets Using D^0+hadron Two-Dimensional Angular Correlations in Au+Au Collisions at $\sqrt{s_{\mathrm{NN}}} = 200$ GeV

by

Alexander Michael Jentsch

DISSERTATION

Presented to the Faculty of the Graduate School of

The University of Texas at Austin

in Partial Fulfillment

of the Requirements

for the Degree of

DOCTOR OF PHILOSOPHY

THE UNIVERSITY OF TEXAS AT AUSTIN

May 2019

To Claire.

Acknowledgments

There are a number of people I need to thank for the successful completion of my doctorate. First, my parents, who have always pushed me to do what I am passionate about, encouraged me when I felt like I could not get it done, and told me they were proud, no matter what. To my friends, especially Prabhat, Erin, Justin, and Ryan who let me bounce ideas off of them, spent time listening to (and groaning at) my terrible jokes, and provided valuable insight, both into the physics we were all studying, and into life in general. I also need to thank Christina, who helped give me a chance to do my graduate studies in the first place, and to Lanny, who really helped me to be a better and more careful scientist (and also drank the dark beers with me at happy hour). I also need to thank those no longer with us: Jerry Hoffmann, for his mentorship and friendship earlier in my graduate career, and giving me a job building detectors after undergrad, and my grandparents, Evan, Joan and Wayne, who were always supportive and cared deeply about my success. I wish they were here to celebrate with me now.

The most important person I need to thank is my wife, Claire, who provided me with love and support, challenged me when I didn't do right by others, and helped me to be a better man and scientist. I dedicate this thesis and this work to you, Claire.

Studying Heavy-Flavor Quark Jets Using D^0+hadron Two-Dimensional Angular Correlations in Au+Au Collisions at $\sqrt{s_{\rm NN}} = 200$ GeV

Publication No. _____

Alexander Michael Jentsch, Ph.D.
The University of Texas at Austin, 2019

Supervisors: Christina Markert
Robert L. Ray

The study of Quantum Chromodynamics (QCD) in conditions of extreme temperature and energy density has been accomplished over the past two decades using heavy-ion collisions at the Relativistic Heavy-Ion Collider (RHIC). Recently, the addition of the Heavy Flavor Tracker from 2014-2016 has granted the STAR experiment the ability to precisely reconstruct decay-vertices of secondary particles separated from the primary collision vertex by $\sim 30\mu m$. This enables the direct reconstruction of heavy-flavor quark (e.g. charm, bottom) mesons, which are useful for studying the hot and dense medium - known as the Quark-Gluon Plasma (QGP) - formed in heavy-ion collisions. Heavy-flavor quarks are useful for studying the QGP because they are formed in hard-scattering interactions that take place before the formation of the medium and then hadronize and decay outside the medium. This makes heavy-quarks sensitive to the entire evolution of the QGP, and therefore an ideal probe for its study.

In this analysis, correlations on relative azimuth and pseudorapidity between a charm-containing meson (D^0) and all other charged hadrons are presented. In particular, the near-side ($\Delta\phi < \frac{\pi}{2}$) jet-like peak is studied, with the D^0 serving as a proxy for charm-jet. Using a multi-parameter fit-model with no underlying physics assumptions, the widths and associated yield of the near-side peak are studied as a function of centrality. The evolution of this near-side correlation structure yields insight into the charm-jet interactions with the partonic medium.

These results are compared to PYTHIA and a trigger-associated light-flavor correlation analysis. The results imply significant interaction of the charm-quark with the medium via gluon radiation and collisions with neighboring partons, similar to what is observed for light-flavor correlations at a similar transverse momentum. Model predictions for heavy-ion collisions that include charm are needed for further understanding of these measurements.

Table of Contents

List of Tables

List of Figures

Chapter 1

Introduction and Motivation

As far as we currently understand, there are four fundamental forces of nature. They are the well-known gravitational force, the electromagnetic force, the weak nuclear force, and the strong nuclear force. Quantum Chromodynamics (QCD) is the theory describing the strong nuclear force, which is the force responsible for the binding together of atomic nuclei and the partons (quarks and gluons) residing in the individual nucleons (protons and neutrons). Decades of experiments indicate that partons are forever bound under the strong force within the confines of their respective hadrons, or particles made from partons.

However, lattice QCD predictions imply that under sufficient conditions ordinary hadronic matter could undergo a transition into a phase where the normally confined partons could become deconfined over nuclear distances, forming a new state of matter called the Quark-Gluon Plasma (QGP) [1, 2]. This state of matter is believed to have existed in the hot and dense early universe just micro-seconds after the Big Bang and possibly exists in the dense cores of neutron stars.

In 1983 it was proposed by Bjorken that the collision of two heavy nuclei at sufficiently high center-of-mass energy could provide the needed temperature and energy density to produce a QGP in a laboratory environment. However, the study of heavy-ion collisions is a steep experimental and theo-

retical challenge, requiring the use of novel techniques and differential measurements to piece together the full dynamical picture of the medium formed in heavy-ion collisions.

The goal of this thesis is to contribute to the overall physics understanding of ultra-relativistic heavy-ion collisions and their relation to the QGP. This goal will be achieved by studying how heavy quarks (charm, in this case) interact with the medium formed in heavy-ion collisions, and see how those interactions compare to the interactions of light quarks (up, down, and strange) in the medium.

1.1 Quarks and the Development of QCD

In 1964, Murray Gell-Mann and George Zweig proposed that baryons and mesons were actually composed of smaller particles of spin-1/2 and fractional electric charge. They proposed that this subtructure was needed to explain the mass differences seen in the baryon and meson octets of particles. This approach was based on the earlier work of Gell-Mann on the Eightfold Way (see Fig. 1.1) to describe the symmetries between hadrons [3, 4, 6].

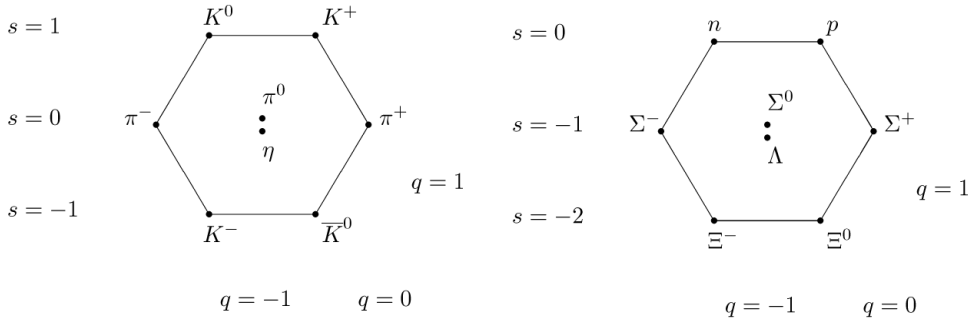

Figure 1.1: Sketch of the Eightfold Way symmetery for the meson and baryon octets. [7]

Gell-Mann and Zweig found that the underlying symmetry to describe this arrangement of the baryon and meson octets was best described by the Lie group SU(3), which led to the proposal that baryons and mesons contained these "quarks", as Gell-Mann called them (Zweig called them "aces"[4]). Baryons are particles comprised of three quarks, while mesons are comprised of a quark and an anti-quark, with quark-containing particles dubbed "hadrons". Initially, only three quark flavors were proposed (up, down, and strange), since that described the observed particle mass differences at that time. It was then the proposal of Zweig that there should be an experimental search for these particles since the formulation under the SU(3) symmetry group described the observed baryon and meson octets so well and even predicted the Ω baryon, which was later discovered at Brookhaven National Laboratory [5].

From 1968 to 1970, deep inelastic scattering experiments performed at the Stanford Linear Accelerator Center (SLAC) confirmed that the proton and neutron had internal, point-like substructure via the observation of Bjorken scaling in the electron+proton scattering cross section. This scaling phenomenon has to do with the structure functions $(W_1(Q^2,\nu), W_2(Q^2,\nu))$ that are a part of the differential cross section for inelastic electron+proton scattering, as seen in Eq. 1.1,

$$\frac{d\sigma}{d\Omega dE'} = \frac{\alpha^2}{4E_0^2 \sin^2(\theta/2)} \cos^2(\theta/2)[W_2(Q^2,\nu) + 2W_1(Q^2,\nu)\tan^2(\theta/2)], \quad (1.1)$$

where E_0 is the energy of the incident electron, E' is the energy of the scattered outgoing electron, θ is the scattering angle, Q^2 is the energy transfer (squared), and $\nu = E_0 - E'$. Experimental data (Fig. 1.2) from SLAC showed that the cross section for these collisions sharply differed with the expectation for elastic scattering.

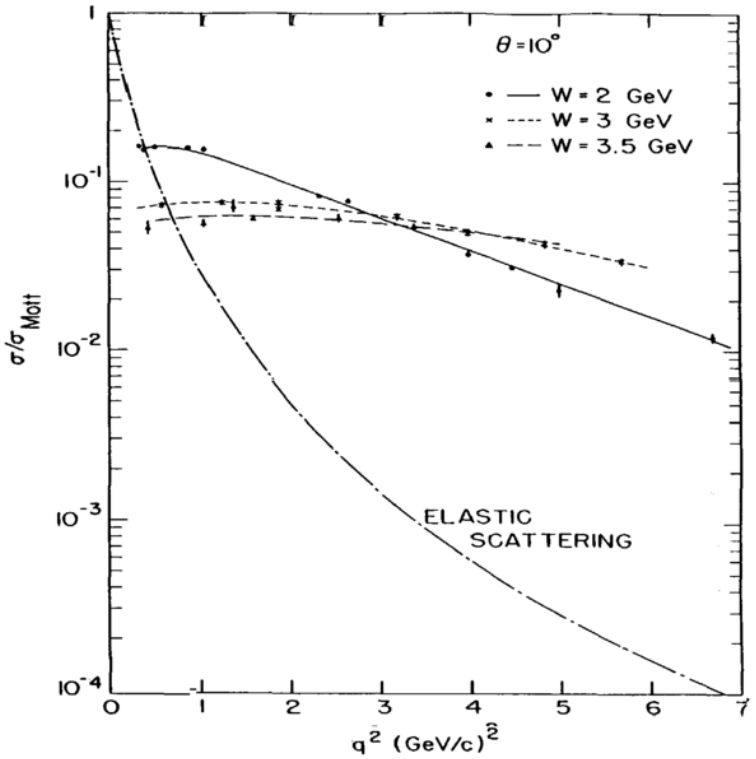

Figure 1.2: Data from SLAC experiments showing the scattering cross section for electron+proton collisions, scaled by the Mott cross section, as a function of q^2 (note: $Q^2 = -q^2$) [8]. The different behavior of the measured cross section compared to the expectation from elastic scattering is apparent and came as a surprise.

Bjorken proposed that these structure functions, W_1 and W_2, could be written as a function of a "scaling variable", $\omega = \frac{2M\nu}{Q^2}$. In the limit $Q^2 \to \infty$ and $\nu \to \infty$, the "Bjorken limit", the structure functions depend only on the scaling variable. Feynman then proposed the "parton" model with the scaling variable $x = \frac{1}{\omega}$ ("Bjorken-x") which naturally explained this scaling behavior coming from collisions of the electrons with sub-nucleonic partons in the protons [9].

Further analysis of the experimental data, and development of theory that included the spins and fractional charges of the partons, confirmed that the quark model proposed by Zweig and Gell-Mann was indeed correct. But there were still some basic problems. For one, based on the Pauli Exclusion Principle, there were some baryon states, namely the Δ^{++} baryon, which would not obey the Pauli Exclusion Principle without the introduction of a new quantum number. In 1972, Murray Gell-Mann and Harald Fritzsch gave a talk in which they presented a new quantum number [10]. They dubbed this quantum number "color", and also introduced the gluon gauge field needed to describe the interactions between the quarks in the strong nuclear force. They described color as a conserved charge, coming in red, green and blue (and the anti-colors). When the color-charges are combined in combinations of all three colors (or anti-colors) for baryons, or a color and its anti-color for mesons, a color-neutral object is formed, which we know as a hadron. Only color-neutral objects are observed in nature. This was the first presentation of an almost modern theory of the strong force - dubbed Quantum Chromodynamics (QCD). But there was still an unanswered question - why were the quarks forever confined in their hadrons?

The answer to this condundrum of confinement came in 1973 with the discovery of "asymptotic freedom" by Politzer, Gross and Wilczek [11, 12] in QCD. Asymptotic freedom describes the strong force as asymptotically "weak" at very short (sub-nucleon) distances, but increasingly strong at nuclear distance or greater. At nuclear distances, the strong-force binding energy between the quarks becomes so large, that it is more favorable for the quarks to form a new quark/anti-quark pair from the QCD vacuum rather than to separate. This makes the observation of a free quark in nature not possible, as far as

we know. The discovery of asymptotic freedom is what solidified QCD as the theory of the strong force and gave it predictive power.

In QCD, because the strong force coupling displays this property of asymptotic freedom, the coupling gets larger (logarithmically) as you go to lower energy (Q^2) exchange. This makes a whole portion of QCD calculations "non-perturbative", which is very problematic and requires special treatment of the theory in order to carry out analytic calculations. In 1974, Ken Wilson proposed a solution to this problem by calculating QCD on a discretized "lattice," and eventually taking the lattice space to a continuum [13]. However, even elementary lattice calculations are very computationally challenging. Despite those challenges, lattice gauge theory has been able to successfully predict properties of hadrons, such as mass, using nothing but lattice QCD.

Over the years the theories of the subatomic world - electro-weak (QED) theory and QCD - as well as the enormous body of collected and analyzed experimental data (including the discovery of the heavy quarks [14, 15, 16, 17, 18], the weak gauge bosons, and the Higgs [19]) have been nicely buttoned-up in the "Standard Model". Fig. 1.3 depicts the full set of Standard Model particles and the force-mediating gauge bosons.

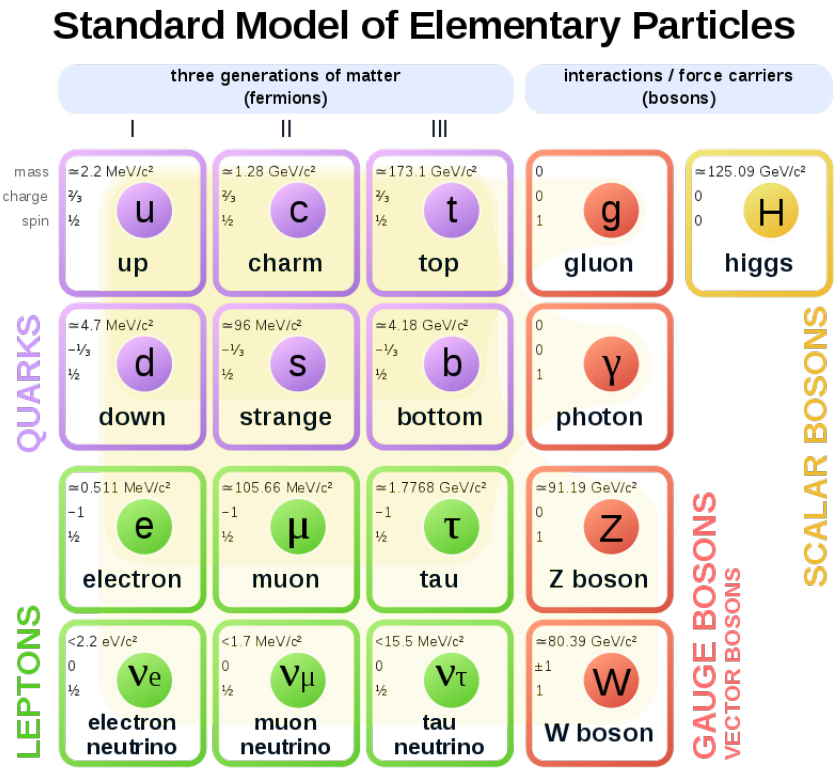

Figure 1.3: Schematic drawing of the Standard Model particles and gauge bosons. [20]

The Standard Model contains six quark flavors, and their anti-quarks: up, down, strange, charm, bottom, and top (in order of increasing mass). It also contains six leptons: the electron, muon, and tau lepton, and their corresponding neutrinos. The gauge bosons are spin-1 particles that mediate the various forces, with the photon being responsible for the electromagnetic force, the gluon responsible for the strong force, and the W/Z bosons responsible for mediating the weak nuclear force. The newly-discovered Higgs Boson [19], partially responsible for giving particles their mass, is also a part of the Standard

Model.

1.2 Deconfinement and The Quark-Gluon Plasma

As stated previously, the running QCD coupling becomes logarithmically weaker at higher energy transfers between partons. From finite temperature perturbation theory [1], the QCD coupling was also shown to become weaker as the temperature increases. Furthermore, chiral symmetry, which is spontaneously broken by QCD, is restored at very high temperature. These observations led to the proposal of a new state of QCD matter at very high temperature where the coupling becomes weak enough for the quarks and gluons to be deconfined over nuclear, rather than nucleon distances [1, 2]. This state of matter is known as the Quark-Gluon Plasma (QGP). Lattice QCD predicts that for matter with zero baryochemical potential (or net baryon density), a crossover phase transition to the QGP phase could happen at $T \sim 150 - 180$ MeV (see Fig. 1.4).

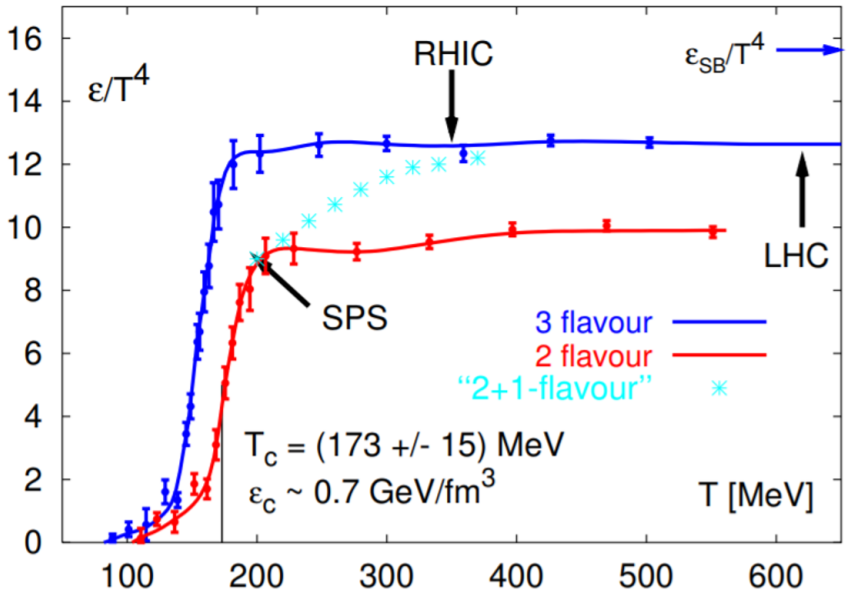

Figure 1.4: Lattice calculations with zero net-baryon density of energy density vs. temperature. A cross-over phase transition can be seen around ∼173 MeV [23].

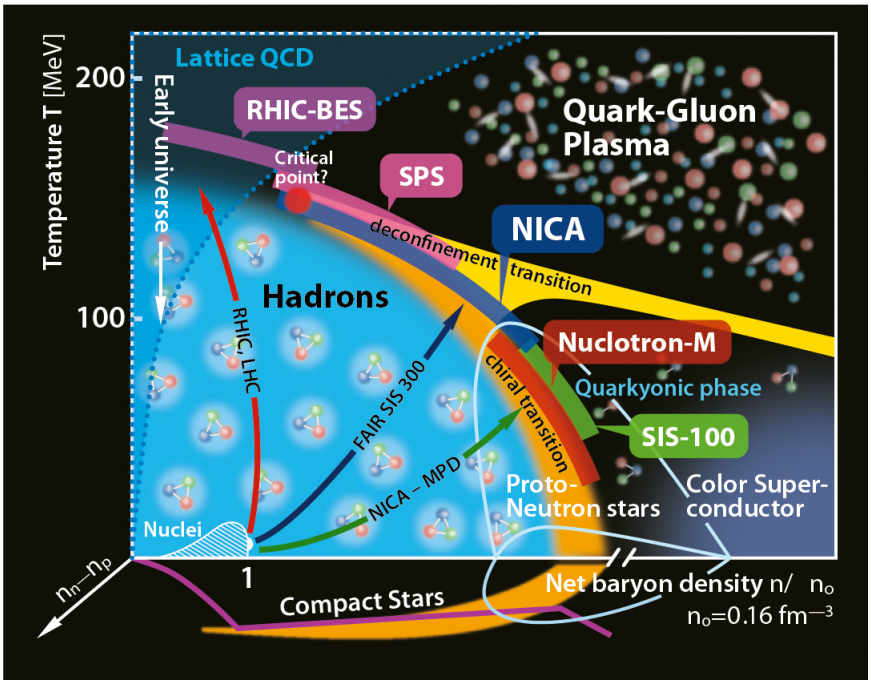

Figure 1.5: Cartoon of the QGP phase diagram, with the limits of lattice predictions loosely outlined [24].

This QGP state of matter is believed to have existed in the very early universe several microseconds after the Big Bang, when the energy density and temperature would have been sufficiently high. Based on the lattice predictions, the phase diagram shows that this state of matter could also exist in the very dense cores of neutron stars (meaning, high baryon density and low temperature - not easily accessible in the lab). The QGP is not just an exotic state of matter to be studied because of where it could have or could now exist. It is also important because its existence is a prediction of QCD, so searching for evidence of and understanding the QGP could help us to better understand the fundamental theory of the strong nuclear force in areas off-limits to perturbative calculations. To study the QGP, our best option is to

use collide heavy-ions in high-energy particle colliders to produce the needed energy density and low net baryon density to produce it.

1.3 Heavy-Ion Collisions

Bjorken first suggested that collisions between two heavy-ions at relativistic energies provide access to the energy densities needed to possibly create a phase transition to a QGP state in a laboratory environment [21]. However, there are significant experimental challenges that must be overcome in using heavy-ion collisions to study high energy density QCD and the QGP.

Several initial observables of the production of a QGP were originally predicted. Perhaps the most-notable early prediction was the existence of critical fluctuations consistent with a first- or second-order phase transition. In fact, the measurement of critical fluctuations of thermodynamic quantities was the original idea of a "smoking gun" observable for the QGP phase transition, since one would expect a rapid change in thermodynamic quantities near a phase transition boundary [22]. Current lattice predictions indicate a rapid crossover transition to a QGP, without necessarily producing critical fluctuations of thermodynamic quantities. Other observables, such as enhancement of strangeness production [25], suppression of the J/ψ via Debye color-screening [27], and opacity of jets traversing the medium [29] were all proposed as signatures of QGP formation. Some of these things have indeed been observed in heavy-ion collisions [26, 28, 30]. Furthermore, ideal hydrodynamics proved to be very successful at explaining the measured azimuthal anisotropy parameter, v_2, and thermal models were able to predict particle yields and ratios, leading to the claim of the existence of an equilibrated, zero-viscosity fluid in heavy-ion collisions [31], or "perfect" fluid.

However, despite all of these signatures for QGP, it turns out that many different phenomenological models can reproduce many of the observables measured, despite having different underlying physical mechanisms [31]. Recently, as newer experimental upgrades are completed and beam luminosities have increased, the use of rare, "hard probes" to study the QGP has grown in popularity. A hard probe is one that is formed by a high-momentum transfer between partons in the colliding nuclei, before any possible phase transition can occur. These hard-scattered partons produce heavy-flavor quarks and jets (collimated sprays of particles) which probe the entire QGP medium from formation to freeze out (when final-state particles are free-streaming to detectors) and can in-principle yield information about the entire evolution of the medium. In general, hard probe measurements are not well-described by the current phenomenological models and could therefore provide constraints to the available bouquet of models on the market. Hard probes are also generally rare processes, requiring combinatorial background reduction and/or very large statistics datasets. The next section will expand on the study of hard probes in heavy-ion collisions.

1.4 Hard Probes and Heavy Flavor

In QCD, interactions involving high momentum transfers $\sim$ 1 GeV/c or more are able to be calculated perturbatively, and are generally referred to as hard processes. As mentioned in the previous sections, observables related to these hard processes are referred to as hard probes and include things like particle jets, heavy-flavor hadrons, and electromagnetic probes, such as photons.

In order for a heavy-flavor quark (i.e. charm, bottom) to be produced

in a heavy-ion collision, an inelastic scattering with high energy transfer must take place (e.g. high energy gluon fusion $g + g \rightarrow c + \overline{c}$). The energy transfer for the formation of the charm is 3 GeV, enabling perturbative calculation of its production using pQCD [33, 34]. These hard-scattering processes happen very early in the evolution of the collision medium [35, 36]. Because of this a heavy-flavor quark is produced before any possible QGP is formed and then, its subsequently formed hadron, decays outside of the medium after freeze out has occurred. This makes heavy-flavor quarks ideal to study the properties of the medium.

Several important heavy flavor measurements have been made thus far at both RHIC and the LHC. Studies of the nuclear modification factor, R_{AA}, which compares production of particles in heavy-ion collisions to the production in proton+proton collisions, scaled by the average number of binary nucleon+nucleon interactions, have demonstrated that charm production is suppressed [32, 37] in very central heavy-ion collisions (see Fig. 1.6).

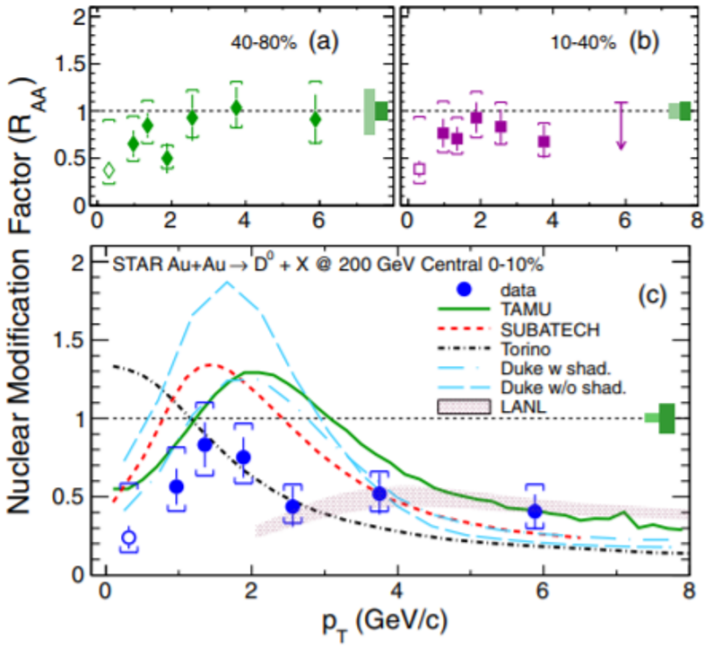

Figure 1.6: Measurement of the nuclear modification factor, R_{AA}, for the D^0-meson in Au+Au collisions at $\sqrt{s_{\mathrm{NN}}}$ =200 GeV, as a function of p_T. Panel a) is the peripheral centrality bin 40-80%, panel b) is 10-40%, and panel c) is 0-10% [32].

Furthermore, it has also been demonstrated that the charm quark has an appreciable azimuthal anisotropy (v_2), which in the conventional understanding implies that the charm quarks experience collective motion in the medium, similar to that of light quarks, although a bit smaller in magnitude [38, 39], as shown in Fig. 1.7.

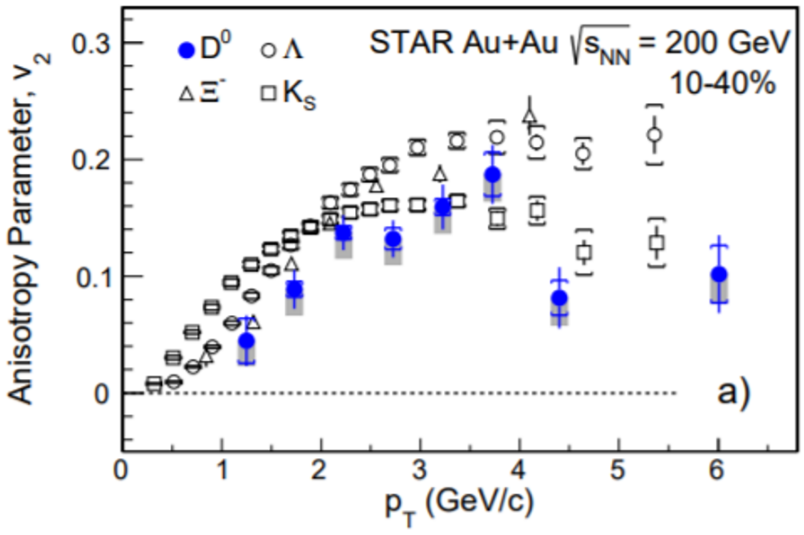

Figure 1.7: Measurement of the azimuthal anisotropy parameter, v_2, for the D^0-meson in Au+Au collisions at $\sqrt{s_{\rm NN}}$ =200 GeV, as a function of p_T [38].

These results were a bit surprising since initial theory predictions indicated that the mass of the charm would be high enough to see significantly less interaction with the medium because of decreased gluon-radiation due to the dead-cone effect [40], and decreased collisional energy loss due to the higher mass [41].

When two-particle correlations are carried out using heavy-flavor hadrons (i.e. D-mesons), access is gained to the underlying dynamics of the interaction between the charm quark and the medium. However, when these correlations are analyzed in heavy-ion collisions, they contain dynamics from vacuum fragmentation as well as from medium interactions. To approximately separate these contributions, correlations must be studied from proton+proton (pp) collisions (vacuum processes), proton+nucleus (pA) collisions (vacuum + nuclear effects), and nucleus+nucleus (AA) collisions. However, much can be

learned by studying the dependence of the correlations in AA collisions as a function of the overlap of the nuclei (centrality), which determines the size of the collision system, and as a function of the momentum or energy of the heavy-flavor quark containing meson.

1.5 Measurement Variables

1.5.1 Kinematic Variables

Before we delve into the details of the detectors, let's digress momentarily to introduce the kinematic variables relevant to the present analysis. Many current high-energy particle and nuclear collider experiments use spectrometers that have cylindrical symmetry. This makes the natural choice of coordinate system cylindrical coordinates based on the geometry of the detectors. However, a coordinate system with a well-defined center makes more sense for measurements involving relativistic transformations from the lab frame to the center-of-mass frame used in collider experiments. As a result, a combination of spherical and cylindrical coordinates are instead used as illustrated in Fig. 1.8.

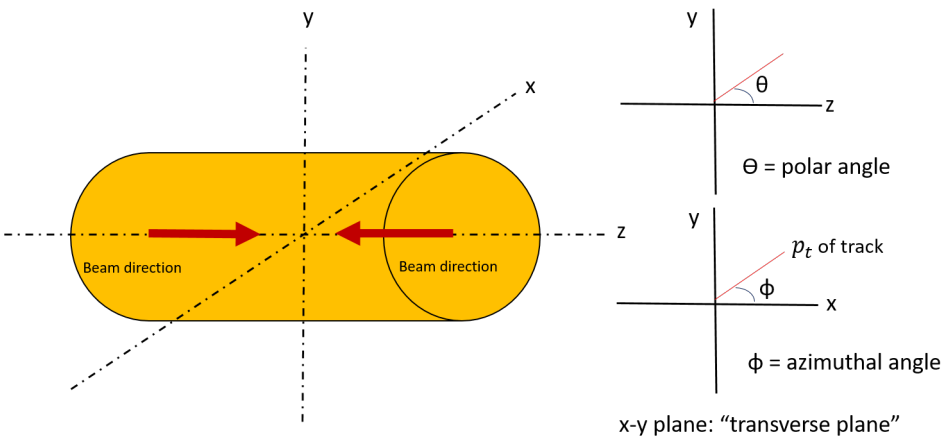

Figure 1.8: Cartoon illustrating a generic cylindrical detector with the axes labeled and relevant quantities noted.

This combination of coordinates uses the particle trajectory (track) momentum vector information on the transverse plane (perpendicular to the beam), containing the x- and y- components of the vector, along with the polar angle (the angle between the z-component and the beam axis) from the spherical coordinate system. Using this set of coordinates, the Cartesian momentum components (p_x, p_y, p_z) are substituted with (p_T, ϕ, η), where $p_T = \sqrt{p_x^2 + p_y^2}$ is the momentum in the transverse plane, ϕ is the angle of the p_T vector in the transverse plane, and η is the *pseudorapidity*, $\eta \equiv -ln(\tan(\frac{\theta}{2}))$. η is dependent on the polar (longitudinal) angle with respect to the beam direction, but the polar angle itself is not a helpful variable since it is not Lorentz invariant or boost-additive. Pseudorapidity is the longitudinal rapidity, $y = \frac{1}{2} ln \frac{E+p_z}{E-p_z}$, in the high-energy limit (i.e. $E >> m$). Rapidity is an additive quantity when boosted to a different reference frame, and therefore a more appropriate quantity for use in relativistic collider experiments.

1.5.2 Impact Parameter and Centrality

In heavy-ion collisions, incoming nuclei do not always collide head-on. In fact, interactions can occur between nuclei that simply pass each other and exchange a virtual photon (so-called "ultra-peripheral collisions"). Measuring observables as a function of the impact parameter, or the amount of overlap, of the colliding nuclei allows one to study the effect of system size on an observable, where more head-on collisions produce the larger system size. The basic idea is illustrated in Fig. 1.9.

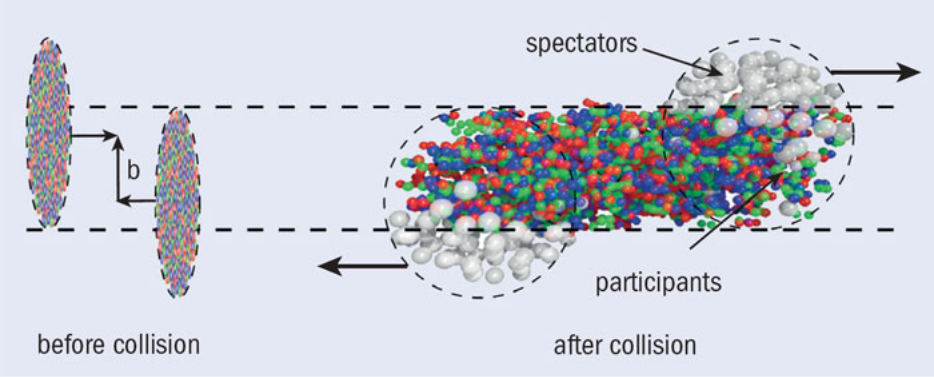

Figure 1.9: Cartoon illustrating a generic collision between two nuclei partially overlapping [42].

The particles (protons and neutrons) that participate in the interaction are known as "participants" while particles in the remaining nuclear fragments that travel down the beam pipe after the collision are called "spectators". Centrality is measured as the fraction of the total inelastic collision cross section, usually written as a percentage range, with the most-central (most head-on, smallest impact parameter) collisions being the ones with the lowest percentages. In practice, centrality is measured by tabulating the charged-particle

multiplicity (the number of tracks counted in the detector) per event and producing a histogram, as illustrated in Fig. 1.10.

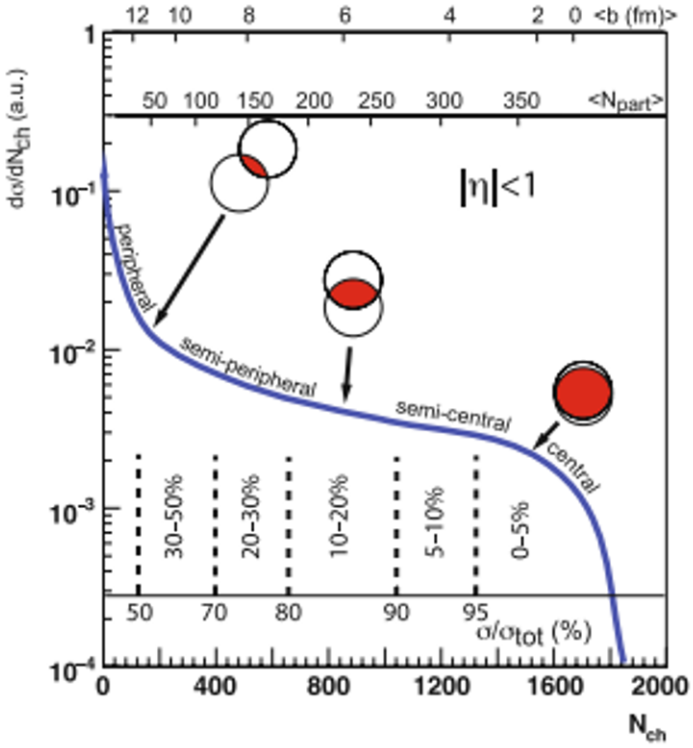

Figure 1.10: Plot depicting centrality fractions extracted from a plot of the charged particle multiplicity [43].

Once this histogram is produced for a sufficient number of events and normalized by the number of events, the distribution is divided into equal-area sections that represent the various multiplicity bins, with the highest charged-particle multiplicities being the central collisions, and the lowest multiplicities being the peripheral collisions. This is related to the inelastic cross section by using a "Glauber Linear Superposition" [44, 45] model that uses geometric arguments to relate the impact parameter to a number of participant particles,

shown in the top axis of Fig. 1.10. By using a Monte Carlo simulation of a Glauber Model (MCG), a similar track multiplicity distribution can be generated that can then be matched to the experimental data from the detector. Only then can centrality fractions be assigned to the multiplicity bins in the data, as shown in Fig. 1.10.

Chapter 2

Experimental Setup

2.1 The Relativistic heavy-ion Collider (RHIC)

RHIC [46] came online in the year 2000 with the physics goals of studying matter at extreme temperature and energy densities via heavy-ion collisions, and of studying the origin of the spin of the proton by colliding beams of polarized protons.

The RHIC accelerator complex consists of several components required to accelerate the ions (maximum energy of 100 GeV per nucleon) or protons (maximum energy of 250 GeV) to the design energies for our physics goals. The heavy-ions are initially produced using the Electron Beam Ion Source (EBIS) [47], capable of providing ions ranging from helium to uranium, while protons are initially sourced by a 200 MeV linear accelerator (LINAC). EBIS produces Au ions with a charge of +32 at an energy of 2 MeV/nucleon. EBIS can also feed ions to the NASA Space Radiation Laboratory, where they are used to test long-term radiation exposure experienced in space.

After the ions are initially produced at this low energy, they are transferred to the Booster Synchrotron, where they are accelerated to 100 MeV/nucleon, or about 37% the speed of light, and further stripped of their electrons to produce ions with a charge of +77. The ions are then injected into the Alternating Gradient Synchrotron (AGS), where they are accelerated to 8.86 GeV/nucleon,

or about 99.7% the speed of light, and are injected into RHIC with their remaining electrons stripped. This process is done twice, once for each of the two RHIC rings. Once the two rings are filled with the ion beams, the beams are further accelerated to the maximum operating energy of 100 GeV/nucleon per beam, yielding a maximum center-of-mass energy of 200 GeV/nucleon-pair. Fig. 2.1 depicts the overview of the RHIC complex.

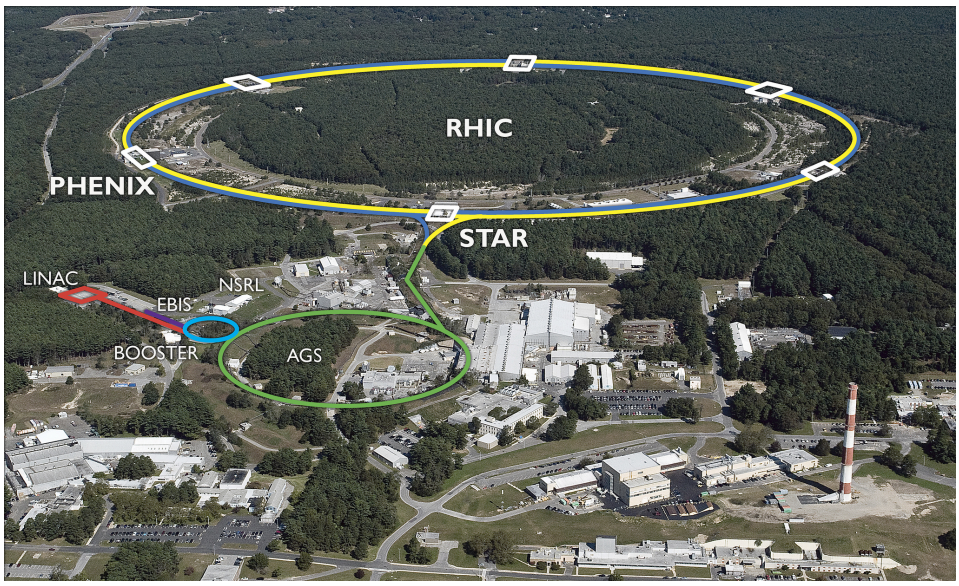

Figure 2.1: Cartoon drawing of the RHIC complex. Courtesy of rhic.bnl.gov.

The RHIC accelerator is 2.4 miles in circumference, and has six regions where the counter-circulating beams intersect - dubbed "interaction regions", or IRs. At the start of RHIC operations, experiments were constructed and placed at four of the six IRs - PHOBOS [48], BRAHMS [49], PHENIX [50] and STAR [51]. PHOBOS and BRAHMS have been decommissioned, and PHENIX is in the process of a complete rebuild as sPHENIX [52]. STAR is currently the only operating experiment at RHIC at the time of this thesis.

2.2 The Solenoidal Tracker at RHIC (STAR) Detector

The STAR detector was designed to be a multi-purpose, mid-rapidity detector capable of collecting both heavy-ion collision data for studying the QGP, as well as polarized proton collision data useful for cold-QCD studies. STAR is comprised of over ten different detector subsystems useful for analysis of a multitude of different physical observables, as shown in Fig. 2.2.

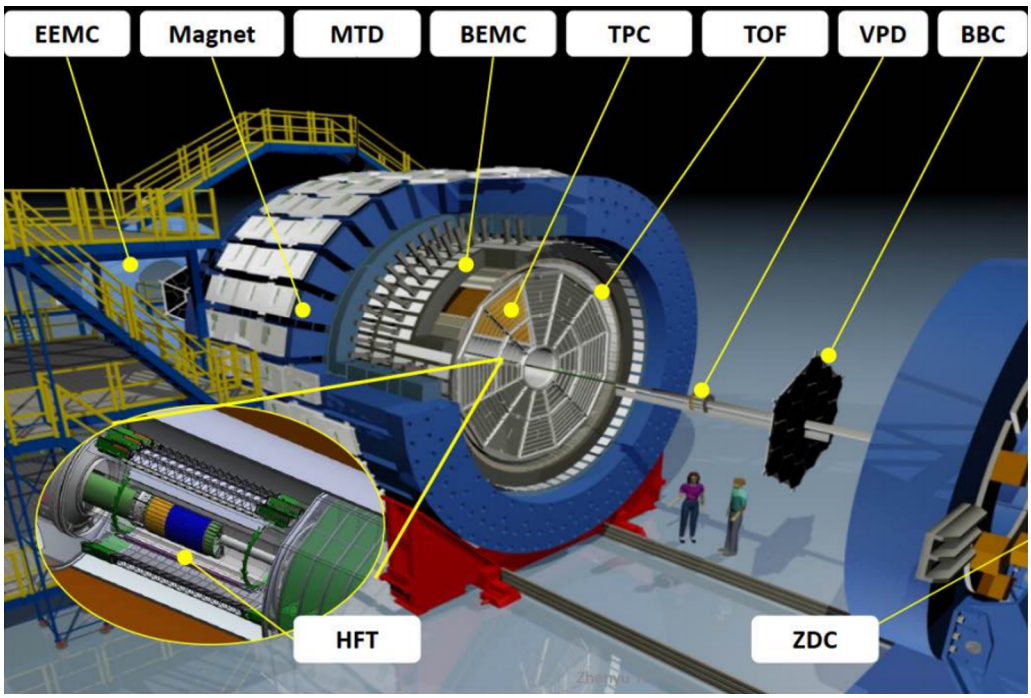

Figure 2.2: Schematic of the STAR detector, depicting the various detector subsystems at STAR. Of special interest to this thesis are the TPC, HFT, VPD, and MTD which are detailed in this chapter.

These detector systems include a Time Projection Chamber (TPC) for tracking, a Barrel Electromagnetic Calorimeter (BEMC) for measuring particle energy, a Time of Flight detector (TOF) useful for particle identification,

the Heavy-Flavor Tracker (HFT) for reconstruction of short-lifetime decay vertices, and the Muon Telescope Detector (MTD) used for identification of di-muon decays from J/ψ and Υs.

In the following sections, I will discuss the sub-systems most relevant to the present analysis, the TPC and HFT, in detail.

2.2.1 Time Projection Chamber (TPC)

Perhaps the most important detector for the majority of analyses carried out by STAR is the Time Projection Chamber (TPC) [53]. This detector allows for the reconstruction of the momentum of particle trajectories (with a .5 T magnetic field directed parallel to the beam) as well as particle identification (PID) by observing the energy loss per unit length (dE/dx) in the detection medium, which is P10 gas (90% argon, 10% methane). The P10 mixture is used because of fast drift velocity of electrons and ions in the gas ($\sim$5.5 cm/μs). The TPC is 4.2 meters long and 4 meters in diameter (see Fig. 2.3).

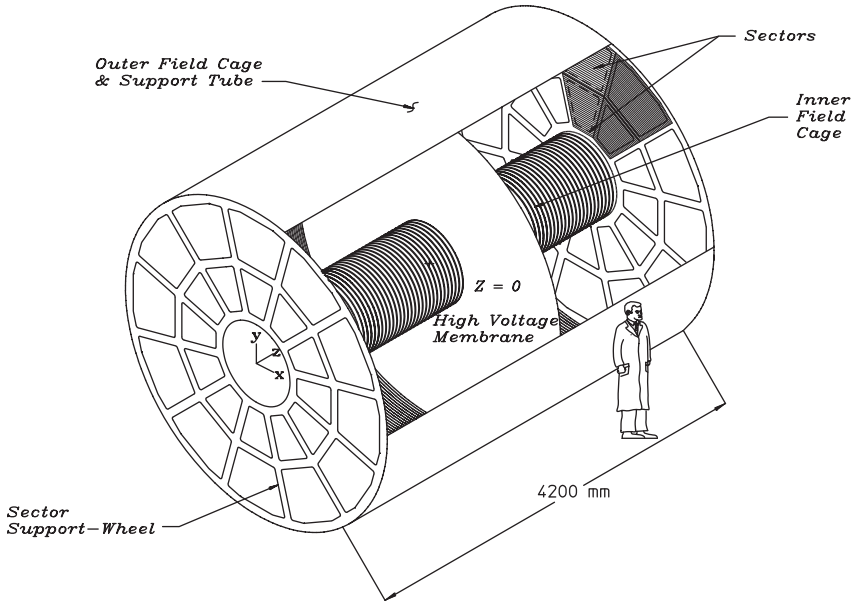

Figure 2.3: Schematic drawing of the STAR TPC [53].

When a charged particle enters the TPC it ionizes the gas molecules. A high-voltage cathode at 28 kV in the central membrane of the TPC causes the liberated electrons in the gas to drift in the electric field toward the endcaps, where they are collected by multi-wire proportional counters (MWPC). The TPC is arranged into 24 sectors, with each sector containing an inner and outer sub-sector. The two endcaps of the TPC each have 12 of these sectors arranged in a circle. An example of a full TPC sector is shown in Fig. 2.4.

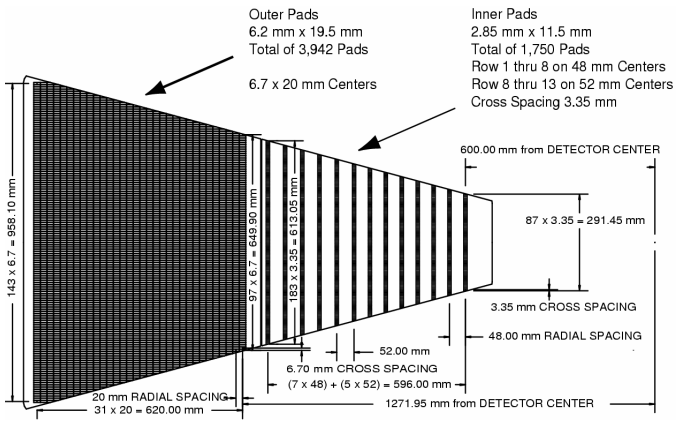

Figure 2.4: Schematic drawing of a STAR TPC sector, with the inner and outer sub-sectors differentiated. [53].

When the electrons arrive at a TPC sector, they are first greeted by a gating grid, which is a set of wires kept at ± 75 V when it is "closed", and 110 V when it is "open". The gating stops the liberated electrons (and left-over positive ions) from making it to the readout pads on the MWPCs. The grid only opens when an event is triggered so the event can be read out. When the gating grid opens, the electrons are drawn toward the anode wires, kept at 1390 V for the outer sectors, and 1170 V for the inner sectors, which cause an avalanche of electrons to create the gain necessary to register hits on the readout pads. These parameters have been chosen to maintain a 20:1 signal to noise ratio for readout of the pads.

Once the hits are collected on the pads, a clustering algorithm is invoked to cluster the hits together so they can be used to reconstruct the particle trajectories (tracks). The x and y coordinates are found by looking at the hits in a pad and the two adjacent pads on the same row (for each direction), and assuming all of signal-peaks are Gaussian (the pad response function). This

approach, detailed in [53], yields an x- and y-coordinate with a precision of a few hundred μm each. The full track information is provided by a maximum of 45 possible hits for single track in the TPC. The z-coordinate is calculated by measuring the drift time between the first ionization of the gas in the TPC (based on the collision trigger) and the readout on the MWPC pads, then dividing this time by the TPC drift velocity. This velocity changes as the TPC gas pressure varies along with the temperature in the TPC. This is somewhat mitigated by the voltage of the cathode, which is chosen to correspond to a maximum drift velocity in the gas. Furthermore, every few hours the TPC drift velocity is re-calculated by using a calibration laser. The various parameters calculated based on TPC information (momentum, energy loss (dE/dx), primary collision vertex, etc.) are all limited by the spatial resolution from reconstruction, as well as other issues that go beyond the scope of the detail necessary for this thesis.

The track information provided by the TPC includes the particle momentum, calculated by looking at the radius of curvature of the track in the STAR magnetic field. The direction of the curvature in the transverse plane also determines the charge of the track, provided you know the direction of the magnetic field. The other information that can be extracted is the energy loss per unit length (dE/dx), which can be plotted as a function of particle momentum. This can be parameterized using the Bischel formula and used for particle identification (PID) [54]. An illustration of the PID capabilities from this information is shown in Fig. 2.5.

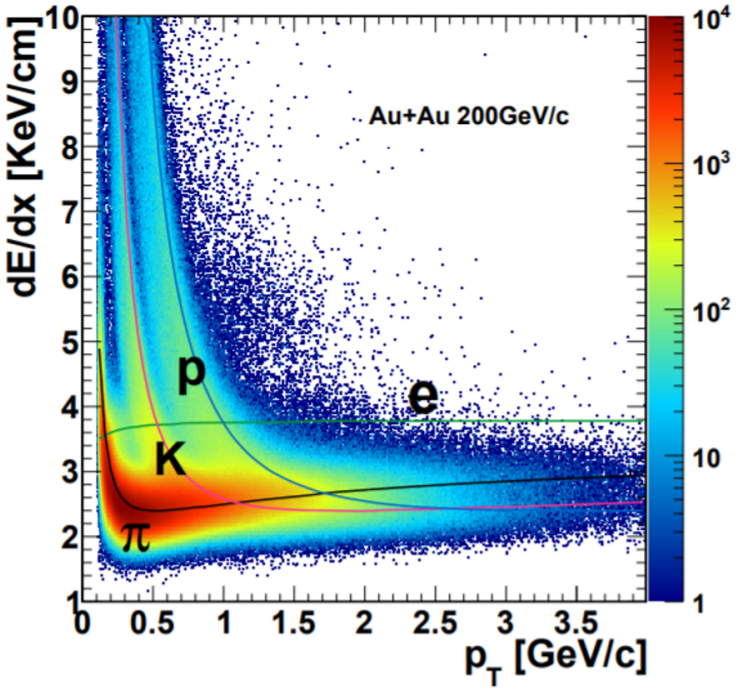

Figure 2.5: Histogram showing track dE/dx vs. momentum. The individual bands from the hits alone are apparent. Each band is fit using a prediction from the Bischel formula, which gives the "expected" values used in Eq. nSigmaFormula to calculate TPC nσ.

In order for this PID capability to be applied a quantity must be calculated that can be imposed as a cut on a track to decide its species. The convenient approach is to calculate the statistical likelihood that a track is identifiable as a particular species using nσ, where the number of σs defines how good of a fit a track's dE/dx vs. momentum is to what is expected by the Bischel formula (normally an n$\sigma < 3$ is considered a good cut). This nσ quantity is defined in Eq. 2.1,

$$n\sigma_{PID,TPC} = \frac{\ln(\mathrm{dE/dx_{measured}}) - \ln(\mathrm{dE/dx_{expected}})}{\sigma_{\ln(\mathrm{dE/dx_{measured}})}}. \tag{2.1}$$

The PID capabilities of the TPC are only good for lower momentum tracks, as shown in Fig. 2.5. The TPC has pseudorapidity acceptance of $|\eta| < 1$, 2π coverage in azimuth, and can reconstruct particle tracks with $p_T > 150$ MeV/c. The distance of closest approach (DCA) resolution for the tracks to the primary collision vertex are limited to about 1 cm making the differentiation of primary and secondary decay particles difficult with the TPC alone.

2.2.2 The Heavy Flavor Tracker (HFT)

Because of the limitations of the TPC in regards to DCA resolution ($\sim$ 1 cm, at best), a detector that can be used to reconstruct secondary decay vertices with a DCA pointing resolution on the order of $\sim 100\mu$m (i.e. for heavy flavor meson decays) is necessary. A silicon detector placed closer to the interaction point is the best option for providing the needed DCA pointing resolution. During the three data-taking runs in 2014, 2015, and 2016 at STAR, the Heavy Flavor Tracker (HFT) was used for analysis of these heavy-flavor decays [55].

The HFT consists of four layers of silicon detectors comprising three individual sub-detectors, as seen in Fig. 2.6.

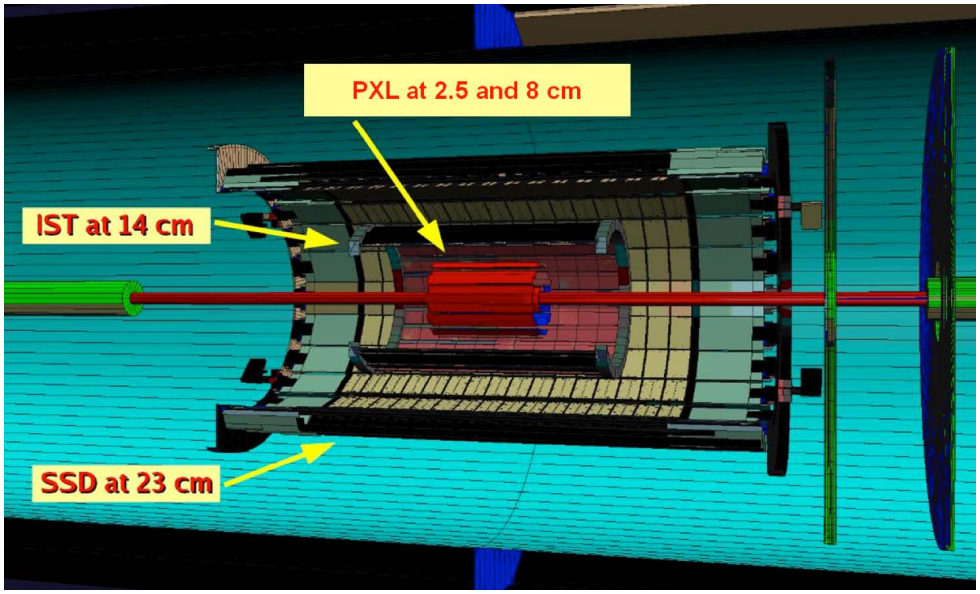

Figure 2.6: Schematic drawing of the Heavy Flavor Tracker.

The inner-most two layers are comprised of individual silicon pixel chips based on MAPS technology [56], collectively called the PXL detector. A schematic is shown in Fig. 2.7.

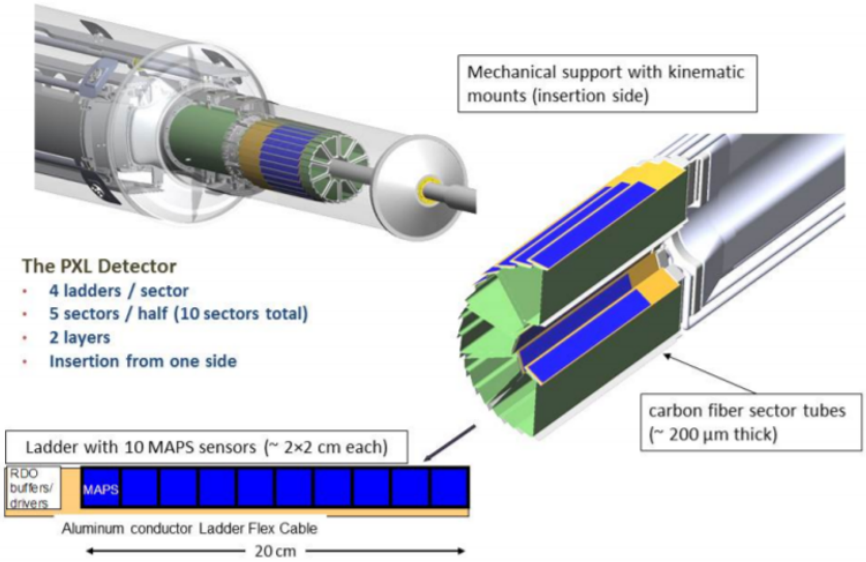

Figure 2.7: Schematic drawing of the PXL sub-detector of the HFT [57]. The PXL detector is arranged in sectors, with each sector containing ladders of ten PXL chips each. One ladder resides on the inner radius of the sector, and three are staggered to overlap on the outer radius of the sector. When the sectors are combined, an inner and outer layer of the PXL detector are formed, allowing for reconstruction of two hits for a single track much closer to the collision vertex than the TPC.

The next detector layer is the Inner Silicon Tracker (IST) [55, 58], which is comprised of silicon-strip detectors. The IST provides an extra detector hit to help guide the TPC track between the TPC and PXL detector, thereby increasing the overall precision of the HFT as a whole. Furthermore, the IST is a very fast detector, making it ideal for filtering out pileup events, or events that occur before or after the triggered collision event being read-out. The final layer is the Silicon Strip Detector (SSD), which is made of silicon drift detectors, and was originally part of the STAR Silicon Vertex Tracker (SVT) [59]. The SSD was meant to provide a redundancy for the

IST and further improve the performance of the HFT as a whole, but did not improve the resolution enough to justify the drop in overall tracking efficiency. Therefore, most HFT analyses do not include it in their tracking. Overall, the HFT achieved a DCA pointing resolution of $\sim$46 μm for kaons with p_T = 750 MeV/c, and better than $\sim$30 μm DCA pointing resolution for tracks with p_T > 1.0 GeV/c, exceeding the original design specifications.

The HFT is able to accomplish two important tasks relevant to analysis involving heavy-flavor hadrons. First, the reconstruction resolution of the full HFT system being at best $\sim$30 μm is more than enough to reconstruct the secondary decay vertex for a D^0-meson (123 μm). The second important task the HFT accomplishes actually comes from the rapid timing of the IST layer of the detector system. The IST can read-out hits at a rate faster than that of the bunch crossing rate for AuAu collisions at RHIC (107 ns). This means that the IST acts a pileup-event filter when you restrict your track sample to only accepting tracks that have the full HFT reconstruction (or tracks that have hits in the IST). Filtering pileup is especially important in correlations analyses as documented in [67].

2.2.3 The Vertex Position Detector (VPD)

The VPD, originally called the pVPD, or "pseudo" VPD (now the "upgraded" VPD, or upVPD), is actually a pair of detectors located on the beam pipe on either side of STAR (see "VPD" in Fig. 2.2) [60]. These detectors consist of 19 photo-multiplier tubes (PMTs) surrounding the beam-pipe like a revolver (see Fig. 2.8).

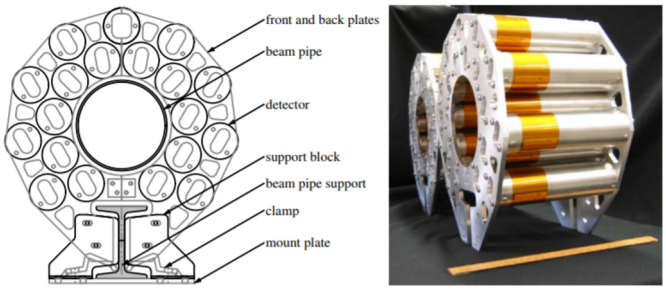

Figure 2.8: The left panel is schematic drawing of one of the upVPD asemblies, and the right panel is a photograph of both upVPD assemblies [60].

The PMTs capture neutral fragments of collided nuclei (spectators) or photons coming from the collisions inside of STAR, providing a start-time for the collision, as well as a time difference based on the different recorded times in both detectors (on either side of STAR). This time difference can be used to calculate the position of the z-coordinate of the primary collision vertex for the two colliding nuclei, assuming the fragments or photons are moving at the speed of light. This provides an independent measurement of the z-position of the primary vertex that can be used to filter out pileup events by requiring that this vertex and the vertex calculated using the TPC tracking differ by only a small amount.

2.3 The Muon Telescope Detector (MTD)

The MTD was fully installed and commissioned at STAR before the start of the 2014 RHIC physics run to complement the heavy-flavor physics program at STAR. The MTD physics goals are to measure charmonium and bottomonium states via their di-muon decay channels produced in Au+Au and p+p collisions in STAR. Even though the physics goals of the MTD are not

directly related to the measurements presented in this thesis, the author spent a considerable amount of time aiding in the construction and commissioning of the MTD, so a digression to discuss these details will be taken.

The MTD sub-system is located on the outer-most layer of STAR as shown in Fig. 2.2. The MTD consists of 120 detector trays arranged in 30 "backlegs" of either three or five MTD trays (see Fig. 2.9). Each tray contains a large Multi-Gap Resistive Plate (MRPC) detector module, discussed in detail in section 2.3.1. The MTD covers 45% of STAR in azimuth and has pseudorapidity coverage of $|\eta| < .5$.

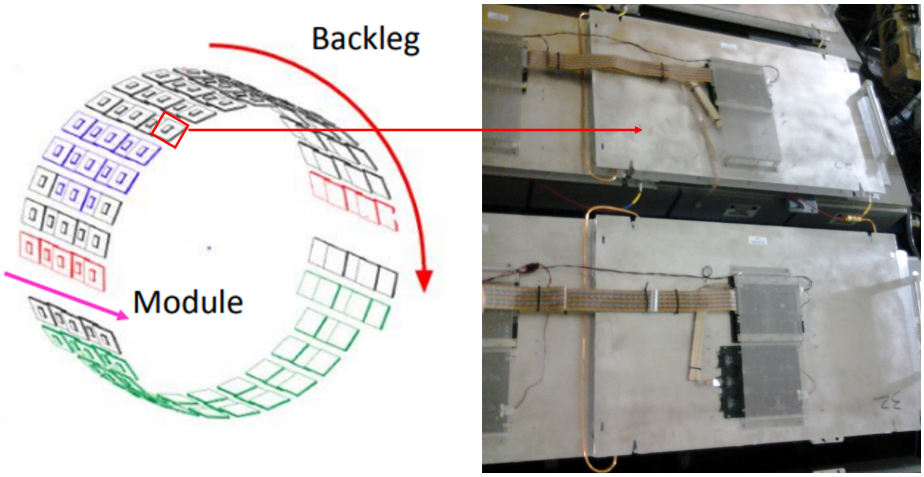

Figure 2.9: The left panel shows a cartoon of the modules arranged in backlegs around the STAR geomtery, with the rest of the STAR detector removed (photo credit: [61]). The right panel shows a photo of some installed MTD trays on STAR taken by the author during the installation in Fall of 2013.

2.3.1 MTD Construction

Each MTD tray is constructed from aluminum and contains an MRPC detector module and the related electronics. The trays were sealed using

a corrosion-resistant silicone sealant (Dow Corning DC-730) to contain the gaseous medium to be ionized by incoming muons. Fig. 2.10 depicts a schematic diagram of an MRPC module. Each module consists of an outer-most layer of honeycomb support structure glued to PCB with twelve long readout strips. Each strip is read-out on both ends to measure a time-difference for a hit, allowing for determination of the position of a hit on the strip. On the other side of the PCB, carbon paint is applied to the surface of the PCB to act as the high-voltage electrode to produce the electric field need to cause the ions liberated by charged particles (muons, in this case) to drift toward the readout pads. The modules are kept at ±6300 V during physics operation. The outer-most layers of glass in the MRPC are adhered directly to the carbon electrode.

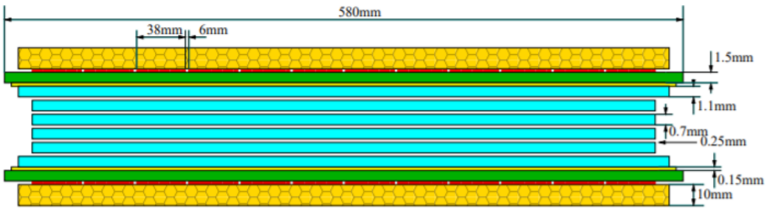

Figure 2.10: A cross-section of an MRPC module with the honeycomb support structure shown in yellow, the glass sparating the individual gas-gaps in sky-blue, and the PCB (green layer) and strip layers [62].

Four more layers of glass are placed between the two outer-most layers of glass, separated by .25 mm using nylon fibers. These layers of glass produce five gas-gaps which contain highly electro-negative R-134a gas (85%), isobutane (10%) to suppress streamers, and SF_6 (5%) to reduce overall noise in the detector. The "multi-gap" in MRPC is a refinement of the original RPC detector, where the gaps allow for a more controlled electron-ion avalanche

from the ionizing particles. This better controlled avalanche allows the timing resolution of the MRPCs used in the MTD to reach ∼90ps! The sum of the liberated charges produce an image charge on the readout strips which generates the pulse read-out by the electronics.

2.3.2 MTD Noise Testing

Before installation at STAR each MTD tray had to be tested for noise to ensure the proper operation and electronic response. The noise testing was preceded by approximately one week of purging with R-134a just above atmospheric pressure after the DC-730 sealant had cured with ambient air for approximately one week. DC-730 off-gases acetic acid (vinegar) and causes the noise rates to increase for the detector. Measurements of detector noise were done for 24 hours at a time, and for a total of approximately five days to see that the noise rates were decreasing as a function of time as the sealant cured and any remaining pollutants in the detector were purged. In the case of very noisy detectors the detectors were purged with N_2 at slightly higher pressure to try and remove any dust particles from the gas gaps. In a few cases, the nylon fibers separating the gas gaps were suspected as possible culprits of high noise rates and the offending modules were completely disassembled (see Fig. 2.11).

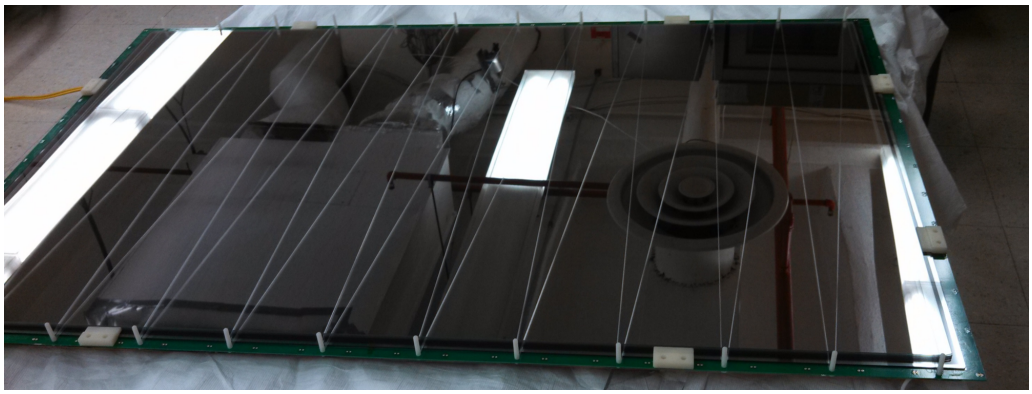

Figure 2.11: An MTD module with the top layer of honeycomb+PCB removed. The zig-zag pattern of nylon fibers separating the glass layers can be seen, as well as the carbon paint beneath the bottom-most glass layer.

Based on the "bad" noise-rate plots, the nylon fiber pattern was seen as the cause of the noise in the case of the fibers being improperly cleaned during assembly and and prior to shipment to UT (see Fig. 2.12). To remedy this issue, the offending modules were disassembled. The individual glass layers were then cleaned with isopropanol and the nylon fibers carefully cleaned and replaced. Fig. 2.12 depicts examples of a good and bad noise rate plots for the MTD detectors.

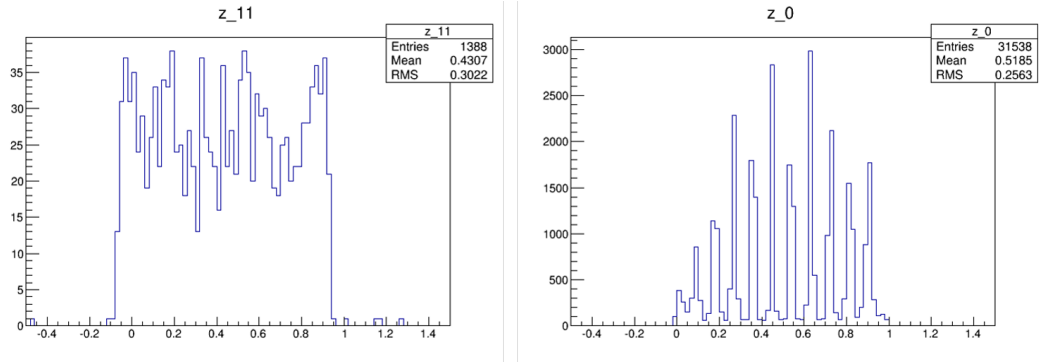

Figure 2.12: Plots of MTD noise rates (in Hz) as a function of percent of total length along strip. The left plot is from a "good" strip, with rates around 30-40Hz and no obvious noise pattern. The right plot is from a strip in a module with dirty nylon fibers, with extremely high noise rates (∼3000 Hz) and obvious periodicity of the noise consistent with the pattern of the nylon fibers.

Chapter 3

Theoretical Background

3.1 Two-Particle Correlations

Two-particle correlations have been used extensively in heavy-ion and nuclear physics for the past several decades. Correlations are useful because they enable the extraction of small signals from the enormous statistical backgrounds in heavy-ion collisions, enabling access to the underlying dynamics.

3.1.1 Pearson's Correlation Coefficient

A statistical correlation was first defined by Karl Pearson and Francis Galton in [63], and has the form of a normalized co-variance,

$$correlation \;=\; \frac{Cov(X,Y)}{\sigma_X \sigma_Y}, \tag{3.1}$$

where $Cov(X,Y)$ refers to a co-variance between two random variables, X and Y, and σ_X and σ_Y are the standard deviations of the random variables. This correlation quantity is dimensionless, and takes values between -1 and +1, with +1 defining a 100%, linear correlation between X and Y, and -1 defining an anti-correlation. A correlation measurement gives a probability that two random variables linearly depend on each other, and coupled with a plausible physical mechanism to relate them, provides good supporting evidence for their relationship. This is especially useful when the underlying

physical relationship is not clearly understood, since models containing various correlations can be directly compared to the correlation from data to either falsify or give weight to a particular model with some physical mechanisms employed. A good example of this would be correlations between CO_2 in our atmosphere and average global surface temperature. The correlation between these data-sets is high, and is explained by the findings of Arrhenius on the heat-trapping power of CO_2 [64] and further confirmed by the observation of the infrared absorption and emission from CO_2 molecules.

In the context of heavy-ion collisions, correlations between final-state particles in an event can provide insight into the dynamical mechanisms that produce them. Correlations between pairs of particles, or *two-particle correlations*, are the simplest to calculate, but are still not well-described by models [67].

Using the definition of the correlation in Eq. 3.1, we can relate the general correlation to a two-particle correlation with

$$correlation \;=\; \frac{1}{N_{events}} \sum_{j=1}^{N_{events}} \sum_{i=1}^{N_{part}} \frac{(n_{a,i} - \overline{n_a})(n_{b,i} - \overline{n_b})}{\sigma_a \sigma_b}, \tag{3.2}$$

where i is the particle index out of an ensemble of particles, N_{part}, all contained in an ensemble of events, N_{events}, indexed by j. $n_{a,i}$ and $n_{b,i}$ represent the number of particles in arbitrary bins, a and b, and the quantities with overbars denote the mean values in those bins, $\frac{1}{N_{part}} \sum_{i=1}^{N_{part}} n_i$. Since we are measuring particle counts, Poisson statistics can be used, which implies that $\sigma_a^2 = \overline{n_a}$ and similarly for bin b. Eq. 3.2 can then be written as

$$
\begin{aligned}
correlation &= \frac{1}{N_{events}} \sum_{j=1}^{N_{events}} \sum_{i=1}^{N_{part}} \frac{(n_{a,i} - \overline{n_a})(n_{b,i} - \overline{n_b})}{\sqrt{\sigma_a^2 \sigma_b^2}} \\
&= \frac{\overline{n_a n_b} \; - \; \overline{n_a} \cdot \overline{n_b}}{\sqrt{\overline{n_a} \cdot \overline{n_b}}}.
\end{aligned}
\tag{3.3}
$$

Since the particle-pair counts in each bin reflect the dimensions of the bin, it is a good idea to remove this dependence by dividing the particle-pair counts by the area of the bin, ϵ. Applying this to all terms in Eq. 3.3 yields,

$$
correlation = \frac{(\overline{n_a n_b}/\epsilon) \; - \; (\overline{n_a} \cdot \overline{n_b}/\epsilon)}{\sqrt{(\overline{n_a} \cdot \overline{n_b})/\epsilon}}. \tag{3.4}
$$

where the products $\overline{n_a n_b}/\epsilon$ and $\sqrt{\overline{n_a} \cdot \overline{n_b}}/\epsilon$ are *two-particle densities*, denoted by ρ. The $\overline{n_a n_b}/\epsilon$ term corresponds to a two-particle density using particles from the same-event, denoted by ρ_{SE}, while the term $\sqrt{\overline{n_a} \cdot \overline{n_b}}/\epsilon$ corresponds to a two-particle density where the particles are coming from independent events, which is defined as the *uncorrelated reference*. We will call this density ρ_{ref}. Substituting these into Eq. 3.4 gives

$$
correlation = \frac{\rho_{\mathrm{SE}} - \rho_{ref}}{\sqrt{\rho_{ref}}}. \tag{3.5}
$$

The last step in constructing a useful correlation measure for use in experiment has to do with the denominator in Eq. 3.5. The root of a two-particle density is problematic because experimentally we are talking about histograms of counts in bins. It is therefore useful to do a trivial algebra step to write Eq. 3.5 as a ratio of the experimentally accessible two-particle densities, multiplied by a "pre-factor" calculated from products of single-particle spectra,

$$
correlation = \frac{\rho_{\mathrm{SE}} - \rho_{ref}}{\sqrt{\rho_{ref}}} = \sqrt{\rho_{ref}} \frac{\rho_{\mathrm{SE}} - \rho_{ref}}{\rho_{ref}}. \tag{3.6}
$$

3.1.2 Correlation Subspaces

Two-particle correlations are computed via construction of two-particle densities from particle collision events. Originally, correlations were calculated in the momentum space of the particles, but the combined momentum space for a two-particle correlation represents a six-dimensional quantity, i.e. $\rho(p_{1x}, p_{1y}, p_{1z}, p_{2x}, p_{2y}, p_{2z})$. In practice, two-particle correlations must be projected onto a smaller-dimensional subspace for us to use them.

For example, correlations between identical pions at the AGS, or Hanbury-Brown Twiss (HBT) correlations, have been carried out by the E877 collaborations in the momentum *difference* space of the particles, reducing the dimensionality of the correlation function from six dimensions to one dimension, $\rho(q = |\vec{p_1} - \vec{p_2}|)$ [65, 66], by taking the difference in the three-momentum of the particle pairs and projecting onto the different (x, y, z) axes. These analyses were carried-out on momentum differences with one in the longitudinal direction (parallel to the beam, q_{long}), one in the transverse direction (perpendicular to the beam, q_{side}), and one in the plane perpendicular to the beam and transverse plane (q_{out}). An additional observable, $Q_{inv} = \sqrt{(p_2 - p_1)^2 - (E_2 - E_1)^2}$, was also used. An example of these results for Q_{inv} is shown in Fig. 3.1.

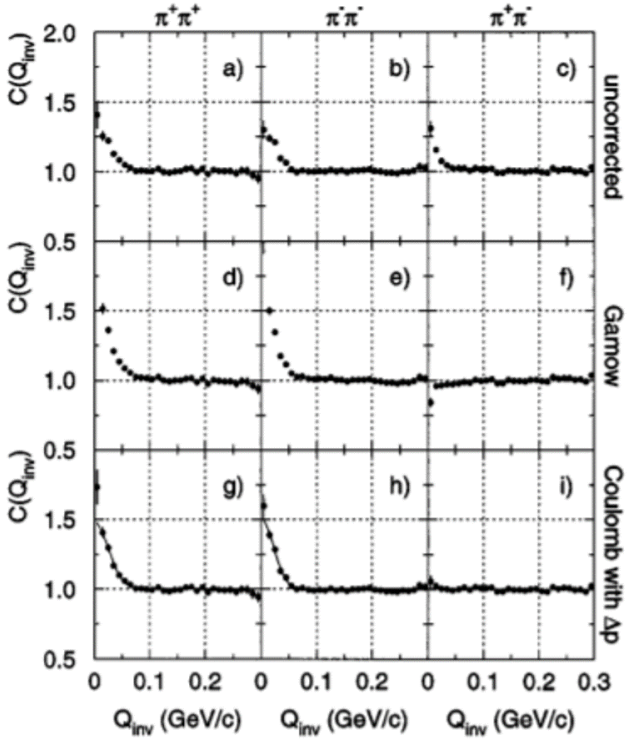

Figure 3.1: Correlations projected on Q_{inv} for $\pi^+\pi^+$, $\pi^-\pi-$ and $\pi^+\pi^-$. The top row are uncorrected, the middle row are Gamow-corrected (Coulomb correction assuming point-like charge source), and the bottom row has the correction for the Coulomb interaction applied. The solid line is the Gaussian fit to the data.

The analysis in Fig. 3.1 had physics extracted via a Gaussian fit to the correlation function $C(Q_{inv}) = 1+\lambda exp[-R^2Q_{inv}^2]$, where λ gives the amplitude of the correlation above unity, and the "R" value is related to the radius of the source (the gold nucleus, in this case). Even with the loss of some dynamical information from projecting onto the sub-space, there is much to be learned from two-particle correlations, such as the radius of the three-dimensional emitting source of particles as shown above.

For this thesis, we are using spherical coordinates (see Section 1.5.1) so our six-dimensional correlation space is $\rho(p_{T,1}, \phi_1, \eta_1, p_{T,2}, \phi_2, \eta_2)$. Correlations in this coordinate space have been projected onto the difference of the azimuthal angles, $\Delta\phi \equiv \phi_2 - \phi_1$, for many analyses as a one-dimensional correlation space. For two-dimensional correlation space, the correlations can be projected onto $p_{T,1}$ and $p_{T,2}$ or the 2D angular difference space ($\Delta\phi = \phi_1 - \phi_2, \Delta\eta = \eta_1 - \eta_2$). The latter two-dimensional sub-spaces in principle contain all of the relevant underlying dynamical information.

For this thesis, the two-dimensional angular subspace ($\Delta\phi = \phi_1 - \phi_2, \Delta\eta = \eta_1 - \eta_2$) is used. All correlation quantities will now be shown as a function of these two variables for the remainder of the thesis.

3.1.3 Correlations Projected on Relative Angular Coordinates (Angular Correlations)

Experimentally, two-particle densities for angular correlations come from counting pairs of particles in bins on the angular supspace in the same-event, and using particles from different events, or *mixed-events*, to approximate the uncorrelated reference. A cartoon example of this is shown in Fig. 3.2.

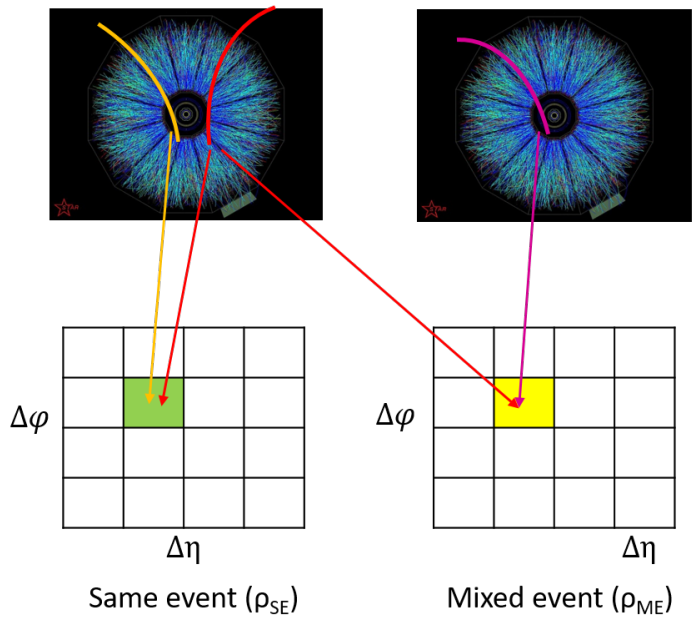

Figure 3.2: An example of building the histograms of two-particle pair densities on $(\Delta\eta, \Delta\phi)$.

Specifying the correlation sub-space, we now write Eq. 3.4 in the second algebraic form, following the method used in [67]. The way the correlation quantity is defined, we are actually calculating the *ratio* of particle-pairs from the same-event to those from the uncorrelated reference, or mixed-events. This ratio has the added bonus of also canceling out our pair acceptance effects and detector inefficiencies. The remaining "pre-factor", $\sqrt{\rho_{ref}}$, which properly scales the final correlations, must be efficiency and acceptance corrected separately. The underlying dynamics related to the widths and amplitudes of correlation structures are encompassed in the ratio $\frac{\rho_{\rm SE}}{\rho_{ref}}$, where the mixed-events are used to construct the reference. The pre-factor is responsible for the final normalization of the correlations needed to yield the number of correlated pairs of particles *per-particle*, or *per-trigger*. The final per-pair correlation is

then

$$correlation(\Delta\eta, \Delta\phi) \propto \frac{\rho(\Delta\eta, \Delta\phi)_{\mathrm{SE}} - \alpha\rho(\Delta\eta, \Delta\phi)_{ME}}{\alpha\rho(\Delta\eta, \Delta\phi)_{ME}}, \tag{3.7}$$

where the α is introduced to normalize the mixed-event distribution, and is defined as $\alpha = \frac{N_{SE}}{N_{ME}}$ where N_{SE} and N_{ME} are the total number of pairs in the same-event and mixed-events distributions, respectively.

3.2 Obtaining Underlying Dynamics from Correlations

There have been a number of methods introduced to try to glean "physics", or the underlying dynamics, from correlation measures. The goal is to extract some quantities from the correlation function found in data, and compare those quantities to correlations from a Monte-Carlo (MC) event generator containing some specific physics mechanisms. The method quantifying the correlation structures involves fitting the structures with a function, and extracting the fit parameters and errors, as was shown in the brief overview of the results from [65, 66] in Section 3.1.2. This procedure can then be carried out for the MC model, and the fit parameters can be compared between MC and data. A few examples of this approach for angular correlations in both proton+proton and Au+Au collision data from STAR are presented in the following sections.

3.2.1 Two-Particle Correlations in Proton-Proton Collisions

Studying two-particle correlations in proton-proton collisions provides a baseline for the study of these correlations in heavy-ion collisions. In 2005,

results presented by R. Jeff Porter on behalf of STAR [68] showed unidentified charged two-particle correlations from STAR proton+proton data at $\sqrt{s} = 200$ GeV, projected on the two-particle subspace $(y_{T,1}, y_{T,2})$, where y_T is the *transverse rapidity* and is approximately the natural log of p_T. Fig. 3.3 shows some of these preliminary $(y_{T,1}, y_{T,2})$ STAR results. These results show correlations using unidentified particles from both the "away-side" (AS) where the difference in azimuthal angle ($\Delta\phi$) between the particles is greater than $\pi/2$, and on the "near-side" (NS), where $\Delta\phi < \pi/2$. Also shown are the charge combinations for particles that have the same charge (same-sign, or SS) and particles that have different charge (unlike-sign, or US).

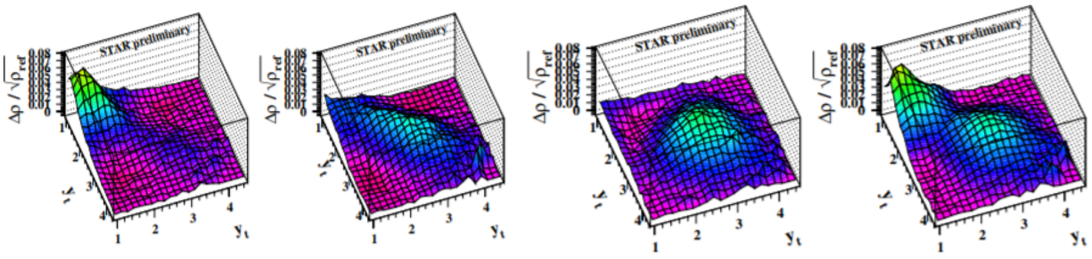

Figure 3.3: Correlations projected on transverse rapidity $(y_{T,1}, y_{T,2})$ for near-side like-sign pairs (first panel), near-side unlike-sign pairs (second panel), away-side like-sign pairs (third panel), and away-side unlike-sign pairs(fourth panel).

These proton+proton correlations can also be projected on two-dimensional angular coordinates $(\Delta\eta, \Delta\phi)$, as shown in Fig. 3.4. The "soft-component" refers to angular pairs with $y_{T,1}$ and $y_{T,2} < 2$ ($p_{T,1}$ and $p_{T,2} < 0.5$ GeV/c), while the "hard-component" refers to angular pairs with $y_{T,1}$ and $y_{T,2} > 2$.

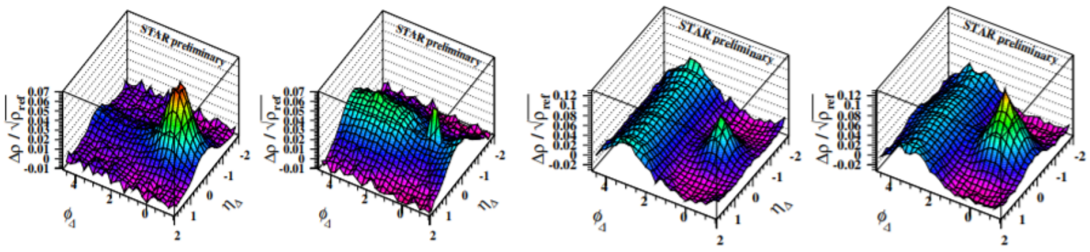

Figure 3.4: Correlations projected on $(\Delta\eta, \Delta\phi)$ for soft-component like-sign pairs (first panel), soft-component unlike-sign pairs (second panel), hard-component like-sign pairs (third panel), and hard-component unlike-sign pairs(fourth panel).

The angular correlations are a bit easier to interpret visually because we are essentially counting particles in phase-space coordinates in the three-dimensional detector cylinder. For example, when we see a peak at $(\Delta\eta, \Delta\phi) = (0, 0)$ what we are observing is an excess above statistical fluctuations of particles very close together in angular space. There are many sources of these particular, peaked correlations on $(\Delta\eta, \Delta\phi) = (0, 0)$ including Hanbury-Brown Twiss (HBT) correlations [69] from the LS pairs (quantum correlations coming from identical bosons), photon conversion in the detector material for unlike-sign pairs (the production of unlike-sign electrons from the material), and the fragmentation of jets from a hard-scattered parton in the collision. Many of these physical correlations are found in the most modern version of PYTHIA [70]. Focusing on the hard-component correlations, one can apply a very simple mathematical model to fit the data, with terms only used to describe the observed structure. In this study, a model including a constant-offset term, a two-dimensional Gaussian term for the NS peak, and a one-dimensional Gaussian on $\Delta\phi$ was used to fit the hard-component data, shown in Eq. 3.8,

$$Fit(\Delta\eta, \Delta\phi) \; = \; A_0 \; + \; A_{NS}\mathrm{Exp}\left(-\frac{\Delta\eta^2}{2\sigma_{\Delta\eta}} - \frac{\Delta\phi^2}{2\sigma_{\Delta\phi}} \right) \; + \; \mathrm{A_{AS}Exp}\left(-\frac{(\Delta\phi - \pi)^2}{2\sigma_{\Delta\phi}} \right). \tag{3.8}$$

This fitting procedure was also carried out for a proton+proton sample using PYTHIA 6.2. The results of those fits are shown in Fig. 3.5.

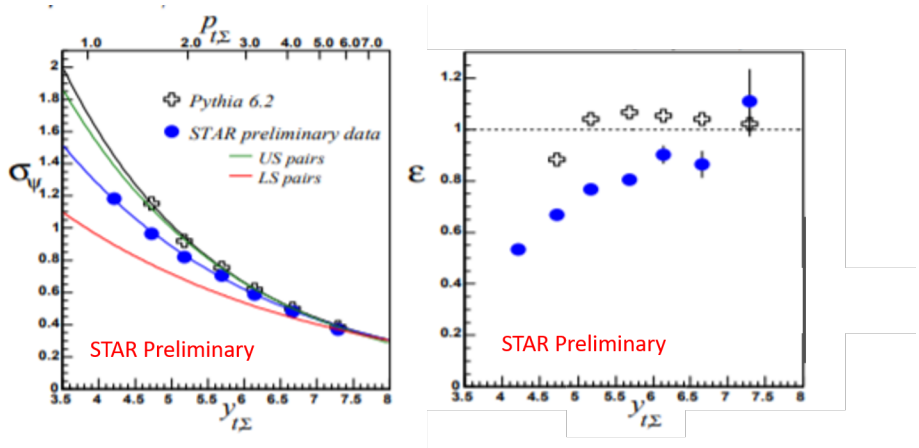

Figure 3.5: Comparison of the fits from the STAR data and PYTHIA 6.2 predictions. The left panel shows a plot of the radius of the NS peak ($\sigma_\Psi = \sqrt{\sigma^2_{\Delta\eta} \; + \; \sigma^2_{\Delta\phi}}$) as a function of the sum $y_{T,1}$ and $y_{T,2}$. The right panel shows a plot of the ratio of the widths of the NS peak ($\epsilon \; = \frac{\sigma_{\Delta\eta}}{\sigma_{\Delta\phi}}$).

From this study, the ability of the two-particle correlation measurement to provide quantitative comparisons to MC physics models is apparent. Studies of the correlation structures on $(y_{T,1}, y_{T,2})$ and a phenomenological description of those structures is discussed in [71].

3.2.2 Two-Particle Angular Correlations in Heavy-Ion Collisions

Since this thesis is on the subject of two-particle correlations in heavy-ion physics, a discussion of this methodology in the more complicated nu-

clear system is necessary. In 2012, STAR published a comprehensive study of unidentified charge-hadron correlations in Au+Au collisions at $\sqrt{s_{\rm NN}}$ = 64 GeV and $\sqrt{s_{\rm NN}}$ = 200 GeV (the "NN" here refers to the center-of-mass energy of two individually colliding nucleons) [67]. In this paper, correlations were studied as a function of centrality, which is related to the impact parameter (or nuclear overlap) of the colliding nuclei (see Sec. 1.5.2). The more central a collision is, the more head-on the nuclei collide, and the more particles are produced. Fig. 3.6 shows the results in a few of the centrality bins for both beam energies.

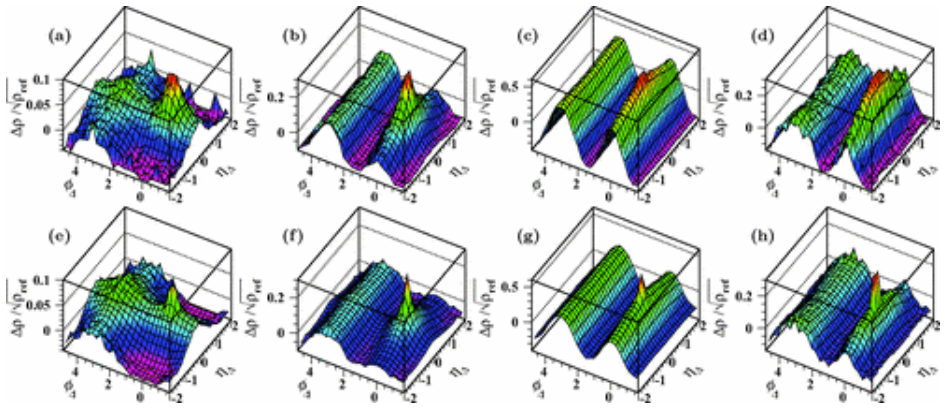

Figure 3.6: Two-dimensional charge-independent angular correlations on $(\Delta\eta, \Delta\phi)$ for Au-Au collisions at $\sqrt{s_{\rm NN}}$ = 64GeV (top row) and $\sqrt{s_{\rm NN}}$ = 200GeV (bottom row). Centrality increases left to right, from most peripheral to most central.

Similar correlation structures are seen as were observed in the correlations from proton+proton collisions, but now there is an addtional modulation in $\Delta\phi$ that appears to be proportional to $cos(2\Delta\phi)$, or a quadrupole. Since these correlations also have no cuts on the transverse momentum, the soft and hard components are all mixed together, meaning more structures are likely

present physically, but hard to observe visually. The fit model for these heavy-ion data therefore contains one more term, the quadrupole, to accommodate the more complicated dynamics observed in heavy-ion collisions and can be found in Eq. (4) of [67]. The results of this fitting procedure are found in Fig. 3.7.

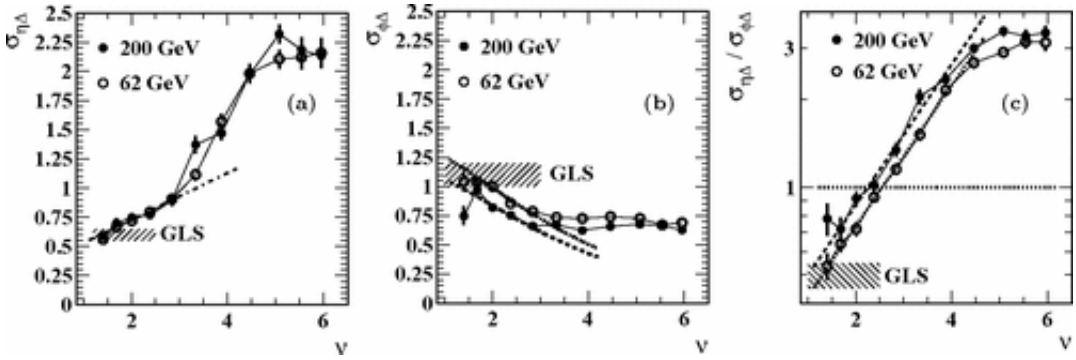

Figure 3.7: Two-dimensional charge-independent angular correlations on $(\Delta\eta, \Delta\phi)$ for Au-Au collisions at $\sqrt{s_{\rm NN}}$ = 64GeV (top row) and $\sqrt{s_{\rm NN}}$ = 200GeV (bottom row). Centrality measure (ν) increases left to right in the x-axis of each plot, from most-peripheral to most-central. The left panel is width of the NS peak on $\Delta\eta$, the middle panel is the width of the NS peak on $\Delta\phi$, and the right panel shows the ratio $\sigma_{\Delta\eta}/\sigma_{\Delta\phi}$

.

The results of the correlation study in Au+Au collisions in [67] showed some interesting results, including significant broadening of the near-side ($\Delta\phi < \pi/2$) correlation peak on $\Delta\eta$ as a function of centrality. These results were in sharp contrast to null-hypothesis Glauber model expectations and indicate significant modification of the the correlation structures in heavy-ion collisions as a function of centrality.

Chapter 4

Analysis Details

Before discussing the details of the correlation analysis the dataset and preliminary cuts must be discussed. This section will discuss the various event and track cuts imposed on the data, and then detail the determination of centrality bins for this analysis.

4.1 Event and Track Selection

4.1.1 Event Selection

The events used in the present analysis all come from the 2014 dataset collected by the STAR experiment (Run14). The dataset consists of 832M *minimum-bias* events - events with no special trigger considerations - with trigger IDs 450050, 450060, 450005, 450015, and 450025. The following cuts were imposed on the events used:

$$| V_{z,TPC} | < 6\ cm$$

$$| V_{z,TPC} - V_{z,upVPD} | < 3\ cm$$

$V_{z,TPC}$ and $V_{z,upVPD}$ refer to the z-coordinate of the primary vertex reconstructed using the TPC and the upVPD, respectively. The TPC vertex is the best-ranked vertex from the vertex finding algorithm using the raw reconstructed track information for an event. The algorthim uses a DCA

minimization to find the z-position of the primary vertex based on the DCA of the z-position of each track to the beamline at $(x, y) = (0, 0)$. The z-vertex from the upVPD is calculated by taking the time difference between the two spectator fragments of the colliding nuclei on the east and west side of STAR, $V_{z,upVPD} = c(T_{east} - T_{west})/2$ (see Sec. 2.2.3)[60].

The 6 cm z-vertex cut is imposed to ensure the events fall within the volume of the Heavy Flavor Tracker detector subsystem used for secondary vertex reconstruction, while the upVPD z-vertex cut is imposed to help remove pileup events by ensuring that the timing window for the vertex falls within a single bunch crossing via the two independently-calculated z-vertices from the TPC and upVPD.

4.1.2 Track Selection

Since this analysis is the measurement of correlated D^0+hadron pairs, separate track cuts are imposed for both the triggers (D^0) and associated charged-hadrons. All tracks in this analysis are required to be "HFT" tracks, meaning that each track has to satisfy the requirement of having hits in both layers of the PXL detector and the IST used in its reconstruction. While it is obvious why this is necessary for the D^0 daughters (given that the HFT is necessary for the secondary vertex reconstruction), the requirement for associated hadrons may not be obvious. The main reason for the additional HFT hit requirement on the associated tracks is that the IST timing is fast enough to differentiate individual bunch-crossings, which happen every 107 ns, making it ideal for removing pileup tracks from our event sample [81]. Pileup has been shown to produce considerable artifacts in two-dimensional, two-particle correlations [67]. Because of the information available (or rather, unavailable)

in the data files for this analysis, post-pileup filtration would have been impossible. Therefore, imposing cuts to remove pileup tracks before calculating correlations, even at the cost of pair-statistics, was the only option to ensure removal of the pileup.

4.1.2.1 Trigger D^0 Selection

The D^0(and $\overline{D^0}$) mesons were reconstructed directly via the hadronic decay channel ($D^0 \rightarrow K+\pi$). Since the average decay length ($c\tau$) for the decay is 123 μm, backgrounds can be significantly reduced in the reconstruction by removing tracks which come from the primary collision vertex (PV) instead of the displaced, secondary vertex (SV). The K and π tracks were identified using the TPC $n\sigma$ from the dE/dx information for the track, as discussed in section 2.2.1. The charge of the tracks is calculated based on the direction of the curvature of the track in the transverse plane due to the 0.5 T magnetic field in the STAR detector, parallel the beam direction (z-axis).

$\mid \eta \mid$	< 1.0
Track DCA to primary vertex	< 3 cm
χ^2 of track helix fit	< 3
nHitsFit in TPC	> 20
nHitsFit/nHitsFitMax	> 0.52
$p_{T,daughters}$	> 0.15 GeV/c
TPC $n\sigma\pi$	< 2.0
TPC $n\sigma K$	< 2.0
reconstructed D^0 candidate p_T	2-10 GeV/c

Table 4.1: General daughter and D^0 cuts.

After ensuring that the candidate daughter tracks meet their respective

requirements for being a TPC K or π, the HFT topological cuts were imposed to reduce combinatorial background originating from tracks coming from the primary vertex.

1) D^0 decay length from PV to SV	$> 212\mu m$
2) DCA daughter K and π	$< 57\mu m$
3) DCA of D^0 candidate mom. vector to PV	$< 38\mu m$
4) DCA daughter K to primary vertex	$> 95\mu m$
5) DCA daughter π to primary vertex	$> 86\mu m$

Table 4.2: D^0 HFT topological cuts.

These cuts came from a Toolkit for Multivariate Analysis (TMVA) study applied in the D^0 v_2 event-plane analysis [38] used to optimize the topological cuts based on the D^0 signal significance, $S/\sqrt{S+B}$. The cuts for the D^0 p_T 2-3 GeV/c bin from [38] were applied to the broader 2-10 GeV/c p_T bin. The systematic uncertainty from varying the topological cuts is discussed in Chapter 6.

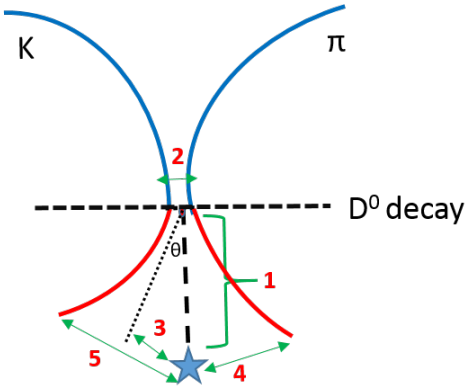

Figure 4.1: Sketch of the D^0 decay. The numbers in the sketch correspond to the enumeration in table 4.2.

In addition to obtaining the Kπ pairs from the invariant mass signal region, we also need triggers from the side-bands of the unlike-sign invariant mass distribution to estimate the correlation contributions from background Kπ pairs (what is done with these pairs is described in section 5.1). The same topological cuts are used for all Kπ pairs, and the invariant mass ranges are in table 4.3.

Signal region	$1.82 < M_{K\pi} < 1.9\ GeV/c$
Left sideband	$1.7 < M_{K\pi} < 1.8\ GeV/c$
Right sideband	$1.92 < M_{K\pi} < 2.1\ GeV/c$

Table 4.3: Invariant mass cuts for the signal and side-band regions.

The illustration of these sidebands is shown in Fig. 4.2.

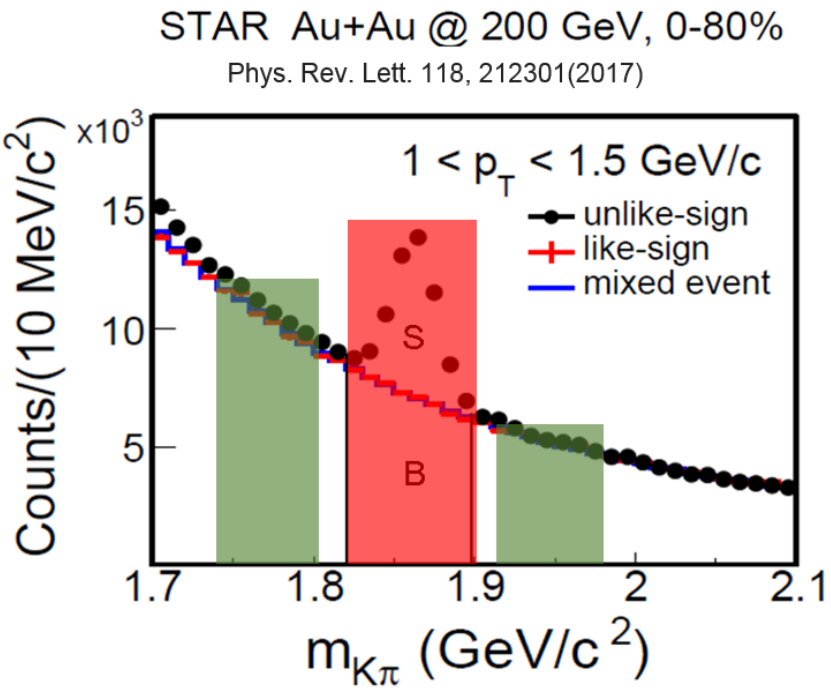

Figure 4.2: Invariant Mass Distribution for D^0 showing the "signal band" (red) and the "side bands" (green) used in the analysis. Several different side band ranges were used to assess systematics on the choice of side bands (see Sec. 6).

4.1.2.2 Associated Hadron Selection

The associated hadrons used for this analysis are any charged particles meeting the cuts mentioned in Table 4.1, except the ones specific to the D^0 itself. We are taking essentially all charged-hadrons in the acceptance of STAR. In principle, one could also place P_T cuts on the associated hadrons to study different physical mechanisms, but the low overall pair-statistics of this analysis established by the scarcity of D^0 events prohibits any of these additional cuts.

4.2 D^0 Reconstruction Results and Yields

As mentioned in Section 4.1.2.1, the reconstruction of the D^0 from its hadronic decay daughters makes use of the HFT and the various topological cuts detailed above. From this reconstruction, we get invariant mass distributions which can be used to extract the signal (S) and background (B) yields. To extract the yields, we construct the invariant mass distributions for both the unlike-sign (US) Kπ pairs and the like-sign (LS) pairs. The LS distributions are then normalized to a region in the US invariant mass distribution where the shapes match well with that of the US distribution (2.0 to 2.2 GeV/c^2), and the normalized LS distribution is subtracted from the US. The residual background is then fit with a straight-line and then removed. The systematic uncertainty for this procedure is discussed in Section 6. The integral over the range $\pm 2\sigma$ (see table 4.3) of the remaining peak, yields the signal (S). Then B is calculated by subtracting S from the total yield in the raw US distribution in the same $\pm 2\sigma$ region. The results of this procedure are shown in Fig. 4.3.

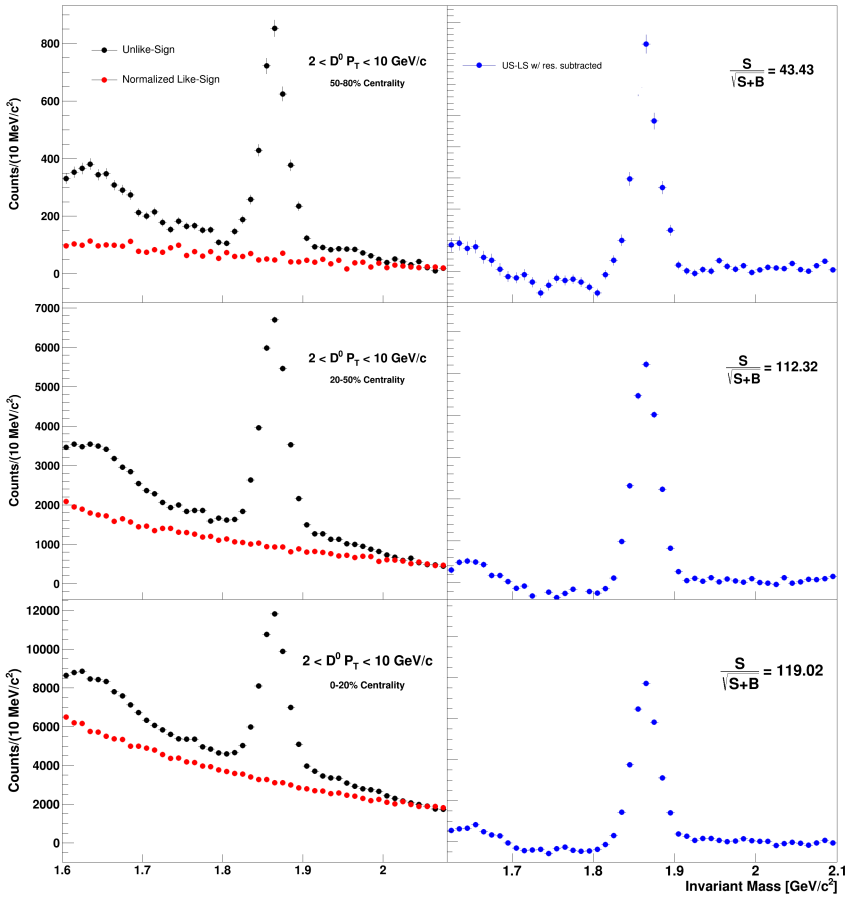

Figure 4.3: D^0 invariant mass distributions for all three centrality bins. The left column is the raw US invariant mass distributions in black, plotted with the normalized LS distribution in red. The right column shows the final, fully-subtracted distribution.

Centrality (%)	50-80%	20-50%	0-20%
Signal Yield	2637±51	20,170±142	30037±173
Background Yield	1049±32	12077±110	33650±183

Table 4.4: Signal and background yields from the invariant mass distributions in Fig. 4.3.

4.3 Centrality Determination

Since this analysis contains correlation information on $|\Delta\eta| < 2$, the standard RefMult software package for determining centrality in STAR, which is restricted to the charged particle multiplicty in $|\Delta\eta| < 1$, could not be used. In the standard RefMult definition, track multiplicity in an event is calculated within $|\eta| < 0.5$. It has been shown in previous analyses involving angular correlations on $\Delta\eta$ that using this definition of centrality with the restriction on $|\eta| < .5$ introduces an unphysical correlation structure at $|\Delta\eta| \geq 1.0$ [67].

To calculate the centrality bins for this analysis, the track multiplicity distribution, dN_{event}/dN_{ch} , is generated from the event-by-event charged-particle multiplicity, where the "good tracks" must meet the requirements for an associated track, with the exception of the HFT requirement. dN_{event}/dN_{ch} is then converted from N_{ch} *vs.* dN_{event}/dN_{ch} to $(N_{ch})^{1/4}$ *vs.* $dN_{event}/dN_{ch}^{1/4}$ using the Jacobian for the transform.

$$\frac{dN_{event}}{dN_{ch}^{1/4}} = 4N_{ch}^{3/4}\frac{dN_{event}}{dN_{ch}} \tag{4.1}$$

This is done in response to the empirical fact that the track-multiplicity distribution follows a power law, $\frac{dN_{event}}{dN_{ch}} \propto N_{ch}^{-3/4}$, if trigger and primary

vertex finding inefficencies are minimal as shown in Ref. [75]. The original track multiplicity distribution and the transformed distribution are shown in Fig. 4.4. In the transformed distribution, trigger and primary vertex finding inefficiencies at lower multiplicity become apparent (seen as a loss from most-peripheral to mid-central events), and the enhancement of high-multiplicity events due to the VPD efficiency can be seen, when compared to Monte-Carlo Glauber (MCG) predictions. Because of this trigger inefficiency for low-multiplicity events, the 80-100% centrality fraction could not be used.

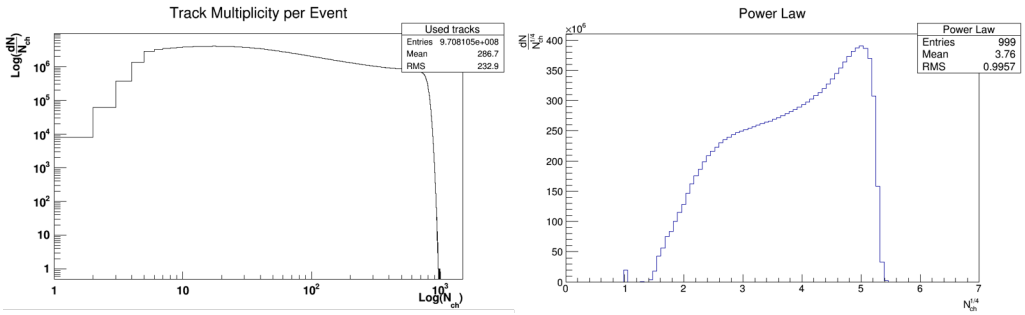

Figure 4.4: Track Multiplicity per event on log-log scale (left) and the Jacobian transform of the track multiplicity distribution (right) in run14.

The procedure to correct the raw distribution is explained in the thesis of Prabhat Bhattarai [76], but we will repeat the basic steps here. Using the power-law distribution from data, and comparing to a MCG, it can readily be seen that there is a loss of events (inefficiencies) at low-multiplicity, compared to MCG, and that the tails do not match at high-multiplicity as in Fig. 4.5.

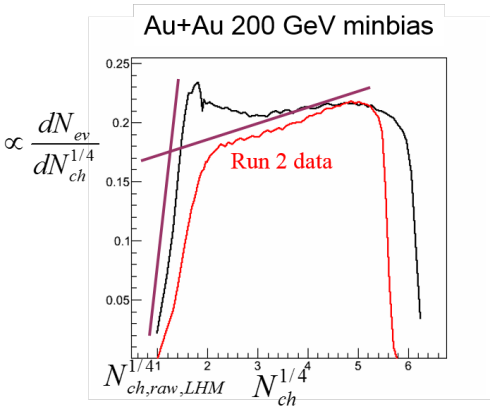

Figure 4.5: Comparison of run2 data (red) to MCG (black).

To correct for this, a non-linear function is introduced to approximately correct the tracking inefficiency,

$$N_{ch,corrected} = N_{ch,raw}\frac{(1+\alpha N_{ch,raw})}{\beta} \tag{4.2}$$

where α and β are chosen to best match the mid-centrality and high-multiplicity tail of the raw data to the MCG. This process was carried out for run2 and run4 Au+Au 200 GeV minimum-bias data in the dihadron correlation paper published by STAR [67].

To correct for these inefficiencies in run14, a slightly simpler approach was taken by matching the raw run14 data to the raw run4 data and then using the previous run4 correction. This was done to simplify the process of centrality determination, and because the trigger bias and vertex finding inefficiencies were much smaller in run4. First, using Eq. (4.2) with $\alpha_{run4} = .000203$ and $\beta_{run4} = .819$ (from matching the raw run4 to MCG), the raw run4 data were corrected in the previous dihadron analysis [67]. Then, the

raw run14 distribution was best-matched to the raw run4 distribution, with $\alpha_{run14} = .00014$ and $\beta_{run14} = .9$, as in figure 4.6.

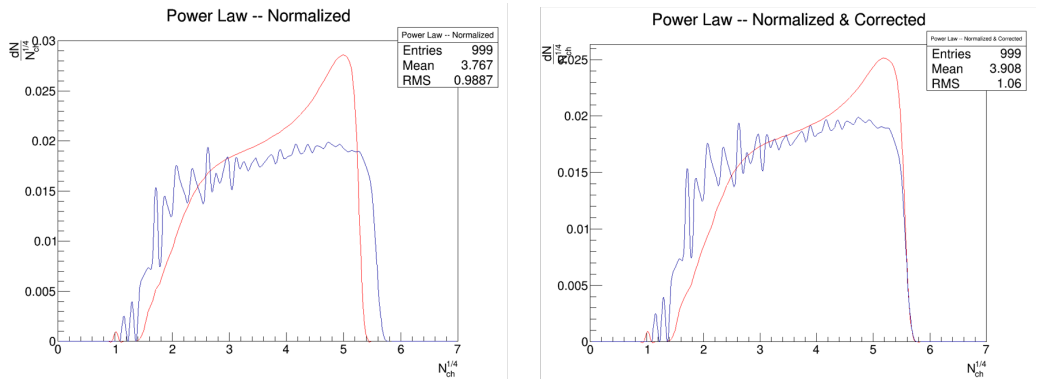

Figure 4.6: Raw run14 power law data (red) and raw run4 data (blue). The left histogram shows the raw data overlaid on the same plot, and the right histogram shows the corrected run14 curve.

Solving Eq.(4.2) for $N_{ch,raw}$, and writing a separate equation for the run4 correction to MCG, and the run14 correction to raw run4 gives:

$$N_{ch,raw,run4} = \frac{\sqrt{1 \ + \ 4\alpha_{run4}\beta_{run4}N_{ch,corr,run4}} - 1}{2\alpha_{run4}} \tag{4.3}$$

$$N_{ch,raw,run14} = \frac{\sqrt{1 \ + \ 4\alpha_{run14}\beta_{run14}N_{ch,raw,run4}} - 1}{2\alpha_{run14}} \tag{4.4}$$

Inserting the corrected N_{ch} values, corresponding to the selected centrality bins in Table 4.5, into Eq.(4.3) and the resulting $N_{ch,raw,run4}$ into Eq.(4.4) gives the uncorrected, raw multiplicity cuts for run14 to use for centrality event selection.

centrality(%)	multiplicity
90-100	2-6
80-90	7-17
70-80	18-39
60-70	40-76
50-60	77-131
40-50	132-209
30-40	210-311
20-30	312-439
10-20	440-596
5-10	597-689
0-5	> 690

Table 4.5: Raw multiplicity cuts for the run14 centrality bins.

This procedure corrects for trigger and track reconstruction inefficiencies, but not for the possible luminosity and z-vertex effects on the centrality determination. The z-vertex effects refer to the different track multiplicities possibly measured for different primary vertex positions. For example, if a collision occurs at a large distance from the center of STAR in z, the detector would only be able to detect a portion of the tracks available in the collisions. The z-vertex effect was addressed at the STAR collaboration meeting at BNL in May of 2017 (see [77]). On slides 15-21 of [77], it was shown that the effects of the luminosity and z-vertex corrections were very small in run4, and they were included as a systematic. Because of the narrow z-vertex requirement imposed by the HFT acceptance in run14, this effect was shown to be very small [78]. The luminosity dependence of the centrality determination is mostly due to increased track reconstruction inefficiencies because of the increased occupancy of tracks in the TPC. For run14, these effects were also studied in [78]), and were subsequently estimated to be negligibly small. The combined effects

from vertex finding and luminosity are estimated to be $< 1\%$ for this analysis.

4.4 Statistical Uncertainty

Statistical uncertainties in two-particle correlations for various event-mixing techniques have been worked out in [79, 80]. In [79], the uncertainties are worked out under the assumption that event-mixing is done using particles from one event with another event, and vice-versa (i.e. the tracks from event A with the tracks from event B, and then the tracks from event B with the tracks from event A). Doing the event mixing using both permutations of tracks from the different events in this manner allows for cancellation of correlated statistical fluctuations between the same-event and mixed-event pairs.

However, in this thesis, the event mixing cannot be done in this way due to statistical and computational constraints caused by the rare production of and reconstruction of of the D^0 ($\sim$ .0001 D^0 per event in our p_T range). Instead, our mixed-event pool consists of the overwhelming majority of events not containing a D^0 candidate, where one D^0 candidate track is mixed with several (five, in this thesis) events from this non-D^0 candidate pool. Because of this, the statistical noise cancellation that happens using the algorithm in [79] does not occur here. This means that the statistical uncertainties in the present analysis contain both uncorrelated and correlated noise. However, these correlated errors are negative contributions to the overall statistical uncertainty, and are small contributions. In order to simplify computation of the correlations, the statistical uncertainties were assumed to only contain uncorrelated noise, making the error scale with $\sqrt{N_{pairs}}$ as shown in [79]. This essentially assumes an upper-bound for the statistical uncertainties presented in this thesis.

Chapter 5

D^0+hadron Correlations

5.1 Derivation of the Correlation Quantity

Experimentally, direct access to a "clean" sample of D^0-mesons is not possible - meaning, there is combinatorial background present that cannot be removed in the process of constructing correlations using the reconstructed trigger-D^0 candidates. In addition, the actual number of correlated pairs is not directly accessible. A relationship with respect to some reference that is uncorrelated (e.g. mixed event reference) must be constructed - as described in 3.1.1. As a reminder here for convenience, $\Delta\rho = \rho_{SE} - \alpha\rho_{ME}$, where $\Delta\rho$ is the same-event correlation distribution minus the mixed-event distribution, which removes the contribution from uncorrelated background pairs.

The starting point for the derivation of the correlation quantity is a number of correlated pairs ($\Delta\rho$). Working backwards from this starting point will enable the relationship between the general correlation quantity of interest in terms of quantities accessible experimentally. Starting with the number of correlated pairs in the "signal region" of the invariant mass spectrum (the red band in Fig. 4.3)):

$$\Delta\rho_{signal} = \Delta\rho_{D^0+hadron} + \Delta\rho_{D^*} + \Delta\rho_{BG+h} \tag{5.1}$$

The first quantity on the right-hand side is the correlated D^0+hadron pair quantity desired; the second quantity includes only those D^0+hadron pairs

where the hadron is a π_{soft} (low-momentum pion) coming from the decay of the $D^{*\pm}$ ($D^* \rightarrow D^0 + \pi_{soft}$); and the third term is the background pairs, where the trigger comes from combinatorial background in the trigger D^0 reconstruction. As a note, the D^* correction is necessary because of the details of the decay kinematics for a D^* meson, and the time it decays (after freeze-out of the medium evolution). This is discussed in detail in Section 5.2.4.

Rearranging the above equation to isolate the $\Delta\rho_{D^0+hadron}$ quantity of interest yields

$$\Delta\rho_{D^0+hadron} = \Delta\rho_{signal} - \Delta\rho_{D^*} - \Delta\rho_{BG+h}. \tag{5.2}$$

The $\Delta\rho$ quantities would in principle be calculated by constructing histograms binned on $(\Delta\eta = \eta_{D^0} - \eta_h, \Delta\phi = \phi_{D^0} - \phi_h)$ from all D^0(candidate)+hadron pairs in the "same-event (SE)" - meaning the candidate Kπ pairs and associated hadrons originating from the same collision event. However, the SE quantity still contains an uncorrelated background (i.e. pairs that have no physical correlations) as well as detector artifacts that can manifest as correlation structure, but contain no physics. This background is removed by constructing a similar set of histograms binned on $(\Delta\eta, \Delta\phi)$, where the associated hadrons come from "different" events, or "mixed-events" (ME), other than the events that contain the D^0(candidate). These mixed-events must have a similar charged-particle multiplicity and similar primary z-vertex location as the events used for the SE pairs.

As described in 3.1.1, $\Delta\rho = \rho_{SE} - \alpha\rho_{ME}$, where α is a normalization factor, which in this case is defined as $\alpha \equiv \frac{N_{same}}{N_{mix}}$, where N_{same}, N_{mix} are the total number of pairs in the SE and ME histograms, respectively. This normalizes the ME distribution to have the same integral as the SE. Then to

correct for detector acceptance and efficiency effects this quantity is divided by the ME histogram,

$$corr = \frac{\rho_{SE} - \alpha\rho_{ME}}{\alpha\rho_{ME}}. \tag{5.3}$$

Eq. 5.3 depicts a simple quantity that represents the physical correlations with detector effects corrected for. Using the above definition for the general correlation quantity in terms of the SE and ME distribution,

$$\begin{aligned} corr(D^0 + hadron) = \frac{\Delta\rho_{D^0+hadron}}{\rho_{ME,D^0+hadron}} = \frac{(\rho_{SE,signal} - \alpha_{signal}\rho_{ME,signal})}{\rho_{ME,D^0+hadron}} \\ - \frac{(\rho_{SE,BG+h} - \alpha_{BG+h}\rho_{ME,BG+h})}{\rho_{ME,D^0+hadron}} - \frac{(\rho_{SE,D^*} - \alpha_{D^*}\rho_{ME,D^*})}{\rho_{ME,D^0+hadron}}. \end{aligned} \tag{5.4}$$

The denominator is not something directly accessible experimentally. Approximations must be made in order to calculate the final correlation quantity from experimentally available quantities. Expanding the first two terms of equation 5.4 in terms of the ME distributions related to the SE for those bands yields,

$$\begin{aligned} \frac{(\rho_{SE,signal} - \alpha_{signal}\rho_{ME,signal})}{\rho_{ME,D^0+hadron}} = \\ \frac{\alpha_{signal}\rho_{ME,signal}}{\rho_{ME,D^0+hadron}} \frac{(\rho_{SE,signal} - \alpha_{signal}\rho_{ME,signal})}{\alpha_{signal}\rho_{ME,signal}} \end{aligned} \tag{5.5}$$

$$\begin{aligned} \frac{(\rho_{SE,BG+h} - \alpha_{BG+h}\rho_{ME,BG+h})}{\rho_{ME,D^0+hadron}} = \\ \frac{\alpha_{BG+h}\rho_{ME,BG+h}}{\rho_{ME,D^0+hadron}} \frac{(\rho_{SE,BG+h} - \alpha_{BG+h}\rho_{ME,BG+h})}{\alpha_{BG+h}\rho_{ME,BG+h}} \end{aligned} \tag{5.6}$$

$$\frac{\alpha_{signal}\rho_{ME,signal}}{\rho_{ME,D^0+hadron}} \simeq \frac{S+B}{S} \tag{5.7}$$

$$\frac{\alpha_{BG+h}\rho_{ME,BG+h}}{\rho_{ME,D^0+hadron}} \simeq \frac{B}{S}, \tag{5.8}$$

where S and B are the signal and background yields extracted from the D^0 invariant mass distributions. Inserting Eqs. 5.5 - 5.8 into Eq. 5.4, the following expression is obtained,

$$\begin{aligned}\frac{\Delta\rho_{D^0+hadron}}{\rho_{ME,D^0+hadron}} = \frac{S+B}{S}\frac{(\rho_{SE,signal} - \alpha_{signal}\rho_{ME,signal})}{\alpha_{signal}\rho_{ME,signal}} \\ - \frac{B}{S}\frac{(\rho_{SE,BG+h} - \alpha_{BG+h}\rho_{ME,BG+h})}{\rho_{ME,BG+h}} - \frac{(\rho_{SE,D^*} - \alpha_{D^*}\rho_{ME,D^*})}{\rho_{ME,D^0+hadron}}.\end{aligned} \tag{5.9}$$

In this analysis, the background is estimated using Kπ-hadron pairs, where the Kπ candidates come from side bands in the invariant mass distribution:

$$\frac{(\rho_{SE,BG+h} - \alpha_{BG+h}\rho_{ME,BG+h})}{\alpha_{BG+h}\rho_{ME,BG+h}} \simeq \frac{(\rho_{SE,SB} - \alpha_{SB}\rho_{ME,SB})}{\alpha_{SB}\rho_{ME,SB}}. \tag{5.10}$$

Like-sign Kπ pairs were also considered for use in describing the background in the correlations, but since the correlation structures are charge dependent, as demonstrated in [67], correlations from two side-bands in the D^0 invariant mass distribution were instead used to approximate the correlation function coming from the background Kπ+hadron pairs.

For the D^* correction the same expansion can be carried out, but the ratio of the ME distributions seen in the previous expansion does not have the same approximate reduction.

$$\frac{(\rho_{SE,D^*} - \alpha_{D^*}\rho_{ME,D^*})}{\rho_{ME,D^0+hadron}} = \frac{\alpha_{D^*}\rho_{ME,D^*}}{\rho_{ME,D^0+hadron}}\frac{(\rho_{SE,D^*} - \alpha_{D^*}\rho_{ME,D^*})}{\alpha_{D^*}\rho_{ME,D^*}} \tag{5.11}$$

$$\rho_{ME,D^0+hadron} \simeq \frac{S}{S+B}\alpha_{signal}\rho_{ME,signal} \tag{5.12}$$

Plugging these expressions into the Eq. 5.4 yields,

$$\frac{\Delta\rho_{D^0+hadron}}{\rho_{ME,D^0+hadron}} = \frac{S+B}{S}\frac{(\rho_{SE,signal}-\alpha_{signal}\rho_{ME,signal})}{\alpha_{signal}\rho_{ME,signal}} - \frac{B}{S}\frac{(\rho_{SE,SB}-\alpha_{SB}\rho_{ME,SB})}{\rho_{ME,SB}} - \frac{S+B}{S}\frac{\alpha_{D^*}\rho_{ME,D^*}}{\alpha_{signal}\rho_{ME,signal}}\frac{(\rho_{SE,D^*}-\alpha_{D^*}\rho_{ME,D^*})}{\alpha_{D^*}\rho_{ME,D^*}}. \quad (5.13)$$

The final expression in Eq. 5.13 represents a correlation quantity that only contains terms accessible experimentally, allowing for approximate calculation of the true D^0+hadron correlations. The next section will detail how to experimentally obtain each of these terms.

5.2 Calculation of Correlations from STAR Data

In order to calculate the final correlations, the $\rho_{SE}(\Delta\eta, \Delta\phi)$ (for events with D^0-candidates) and $\rho_{ME}(\Delta\eta, \Delta\phi)$ (using associated hadrons from different events) histograms need to be obtained for each term in Eq. 5.13. For any given event, if that event has a "candidate" - either a "signal" region or "sideband" Kπ pair that passes the required cuts in Tables 4.1 and 4.2 - then the event is used to generate the SE pairs for the present Kπ candidate. The details of this procedure and the event mixing are in the following sections.

5.2.1 Event Mixing with V_z and Multiplicity (N_{ch}) Sub-bins

In order to construct the uncorrelated background distribution on $(\Delta\eta, \Delta\phi)$, an event-mixing technique is used, where the $(\Delta\eta, \Delta\phi)$ distribution with D^0 candidates from one event is formed with charged-hadrons from another, "sim-

ilar" event. The event-mixing in this analysis had to be done in such a way as to ensure enough events were present in the mixed-event buffer so event-mixing could take place efficiently. Unfortunately, due to the low statistics for the D^0 events ($< \sim 1$ per 10^6 events) there were never enough events populated to do the mixing with those events alone.

"Similar" meaning that the events have a similar charged-track multiplicity (N_{ch}) and a similar primary vertex position in the TPC (specifically, the z-coordinate). The ranges of the various bins are chosen to balance the need for enough statistics to carry out the event mixing, and to ensure that events being mixed don't have some inherent bias by virtue of being very different (i.e. an event with a primary vertex far away from another primary vertex will have a different TPC acceptance). The full range of the V_z cuts were chosen to ensure the events fall within the HFT detector volume ($\pm$ 6cm relative to the geometric center of STAR). The cut ranges for both the N_{ch} and V_z bins are shown in tables 5.1 and 5.2.

Bin	V_z range (in cm)
1	[-6, -4.8)
2	[-4.8, -3.6)
3	[-3.6, -2.4)
4	[-2.4, -1.2)
5	[-1.2, 0.0)
6	[0.0, 1.2)
7	[1.2, 2.4)
8	[2.4, 3.6)
9	[3.6, 4.8)
10	[4.8, 6.0]

Table 5.1: V_z bins for event-mixing.

Bin	N_{ch} range
1	[1, 42)
2	[42, 86)
3	[86, 131)
4	[131, 183)
5	[183, 235)
6	[235, 288)
7	[288, 340)
8	[340, 392)
9	[392, 440)
10	[440, 491)
11	[491, 542)
12	[542, 593)
13	[593, 644)
14	[644, 695)
15	[695, 746)
16	≥ 746

Table 5.2: N_{ch} bins for event-mixing.

The main reason these events must have these similarities is because of the different two-particle acceptance effects. For example, if an event is very close to the edge of the acceptance in V_z (perhaps at 5 cm), the tracks streaming through the detector closer to that edge have less physical space to be able to traverse the TPC and still acquire enough hits to meet the quality cuts. This results in an skewed correlation function on $\Delta\eta$, rather than the normal symmetric triangular shape seen in the center of the detector. Because of this, events used for mixing must have the same general acceptance shape in order to actually cancel these effects.

5.2.2 Efficiency Corrections

In correlation analyses in general, taking a ratio of SE and ME distributions cancels out acceptance and detector inefficiency effects present in the SE distributions. In most cases, this is also true for the efficiency effects present in the SE pair distribution, if the efficiency variation for the single-particle distributions are roughly constant in the region of interest (or change slowly). Even though in the present analysis, these effects have been shown to cancel out with no discernible effects on the final correlations when comparing the results with and without the efficiency corrections, the efficiency correction is still applied to D^0+hadron pairs.

5.2.2.1 Associated Hadron Efficiency Correction

The efficiency function for the associated hadrons is taken from published STAR spectra [72],

$$\epsilon_{h,TPC}(p_T) = P_0 e^{-(\frac{P_1}{p_T})^{P_2}}, \tag{5.14}$$

where the parameters P_0, P_1, and P_2 are taken from table IV of [72]. This function is then multiplied by a correction factor to account for the inclusion of the HFT - the so-called "HFT ratio", which reduces the overall efficiency since not every good TPC track is matched to and reconstructed with HFT hits. The HFT ratio comes from taking the hadron p_T-distribution with the HFT required, and dividing by the non-HFT TPC p_T-distribution [38], with each distribution normalized by the total number of counts,

$$HFTRatio = \frac{TPC + HFT\ p_T\ dist}{TPConly\ p_T\ dist}. \tag{5.15}$$

This yields the results in Fig. 5.1, which were fit with a 6th-order polynomial.

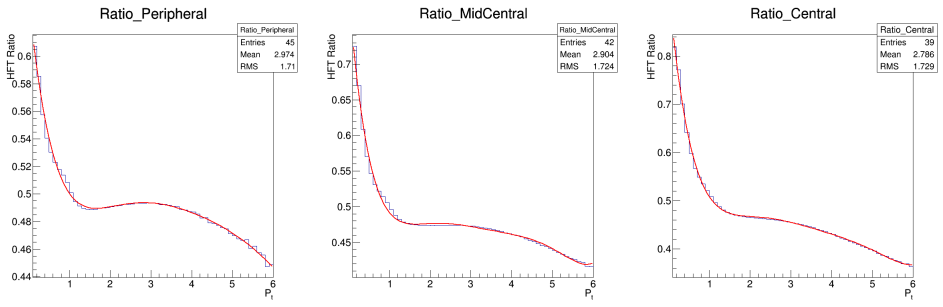

Figure 5.1: HFT Ratio plots with 6th-degree polynomial fit.

The parameters of the 6th-order polynomial fit [P(0)-P(6)] for the HFT ratios were extracted from the three centrality-bins and can be found in table 5.3.

cent. bin	P(0)	P(1)	P(2)	P(3)	P(4)	P(5)	P(6)
peripheral	.6427	-.2948	.2179	-.0793	.0153	-0.0015	6.084e-5
mid-central	.8062	-.7176	.6154	-.2665	.0617	-.0073	3.319e-4
central	.9455	-.9337	.7367	-.2981	.0649	-.0073	3.319e-4

Table 5.3: Table of 6th-order polynomial fit parameters for the HFT Ratios.

The final hadron efficiency correction becomes,

$$\epsilon_h(p_T)_{corrected} = \epsilon_{h,TPC}(p_T) \ * \ HFTRatio(p_T). \tag{5.16}$$

5.2.2.2 D^0 Efficiency Correction

The efficiency correction for the D^0 is calculated by comparing the raw yields of D^0 mesons found in the present dataset to published, corrected spectra for STAR data [85] (an erratum for [32]). Fig. 5.2 shows the published STAR D^0 meson spectra in three centrality bins. The spectra were fit with a

Levy distribution,

$$Fit(A, T, n, m_T, m_0) = \frac{A}{(1 + \frac{m_T - m_0}{nT})^n}, \tag{5.17}$$

where A, T and n are parameters of the distribution, m_0 is the rest mass of the D^0, and m_T is the transverse mass, $m_T = \sqrt{p_T^2 + m_0^2}$. The fit parameters for all three of the centrality bins can be found in Table 5.4.

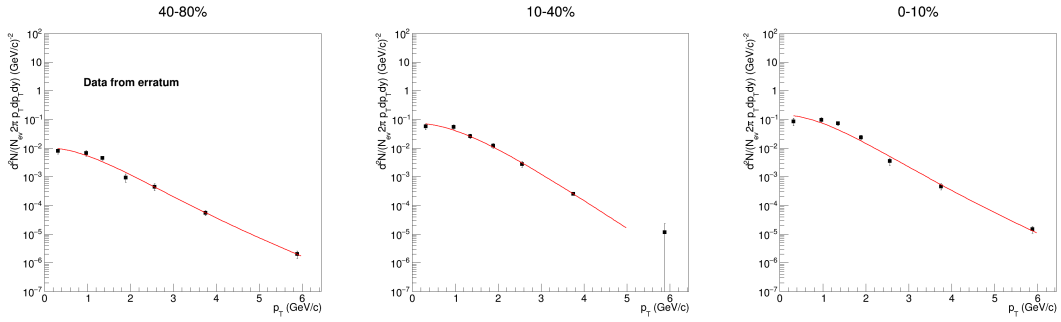

Figure 5.2: Plot of the D^0 spectra from [32]. The red curve shows the fit with the Levy distribution.

cent. bin	A	T	n
40-80 %	.0214	12.995	.3256
10-40%	.1566	249.9997	.3705
0-10%	.3638	15.91	.3070

Table 5.4: Table of Levy fit parameters for D^0 meson spectra data.

Using the corrected spectra compared with the raw, uncorrected D^0 signal yields per event in the present data enables an overall efficiency correction for the D^0 reconstruction in the present dataset. To do this, the D^0 was reconstructed in 10 p_T-bins in all three centralities, with some bins being too sparsely populated to extract a yield. The procedure for extracting the signal

yield was the same as was described in Section 4.2. Once these yields were extracted, the efficiency was calculated to be,

$$eff_{D^0}(p_T - bin) = \frac{Yield_{raw,p_T-bin}/N_{ev,p_T-bin}}{\left(\frac{p_T^2}{m_T}\frac{A}{(1+\frac{m_T-m_0}{nT})^n}\right)}, \tag{5.18}$$

where the factor p_T^2/m_T in the denominator of Eq. 5.18 is included to convert the D^0 spectra data from $\frac{d^2N}{(2\pi p_T)dp_T dy}$ to $\frac{d^2N}{(2\pi)dp_T d\eta}$, which is the form obtained from the raw run14 D^0 yield. The result of these efficiencies per p_T-bin were fit with a 4th-order polynomial. The results can be seen in Fig. 5.3, plotted with their respective fits. Table 5.5 shows the fit parameter values for 4th-order polynomial.

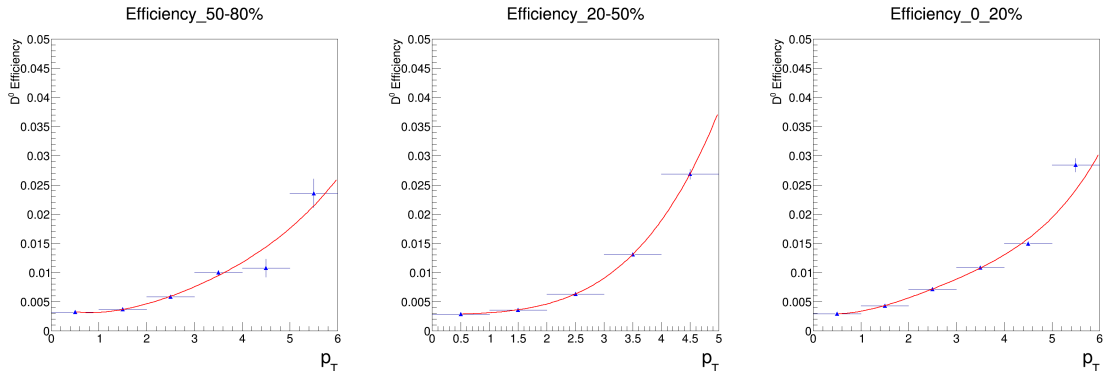

Figure 5.3: Plot of all the D^0 efficiencies for this analysis. The red curves are the individual 4th-order polynomial fits. The parameters for the fits are summed up in table 5.5

The final D^0 efficiencies are fit with a 4th-order polynomial. The parameters are listed below:

centrality bin	P(0)	P(1)	P(2)	P(3)	P(4)
peripheral	0.002258	-0.000672	0.000689	0.000035	-0.000007
mid-central	0.004414	-0.007136	0.003958	-0.000377	0.000010
central	0.001541	-0.000731	0.000957	-0.000036	-0.000002

Table 5.5: Table of 4th-order polynomial fit parameters for the D^0 efficiencies.

Above $p_T = 6$ GeV/c, the efficiency calculation was not reliable to due the very low statistics of D^0 events at the higher p_T at STAR. For this reason, the efficiency correction for the D^0s with $p_T > 6$ GeV/c were taken to be flat. In the case of the mid-central bin, this was actually cut back to $p_T < 5$ GeV/c because of the error bars on the 10-40% central D^0 spectra data. The effect of this efficiency correction on the final correlations is discussed in Section 6. The D^0 efficiency correction applied to the data presented in Sec. 5.2.5 used spectra data from [32], the publication previous to the recently published erratum. The updated efficiency correction from the erratum was studied in comparison to the old correction applied to the data presented here. The erratum spectra resulted in an efficiency correction with the same functional shape and a few percent difference in overall amplitude. Due to technical constraints at the time of this analysis and the small effect of the efficiency correction on the final results (see Sec. 6), the D^0 correction applied to the data in this thesis uses the spectra from [32].

5.2.2.3 Full Efficiency Correction and Pair Weight

These individual efficiency corrections are applied for every D^0-candidate + hadron pair by applying a weight-factor to the pair. The weight factor is

calculated from the efficiency functions derived in the previous sections for the hadrons and D^0s. However, a heuristic method was employed to calculate a pair weight that accounts for the different reconstruction efficiency of a true D^0 and a combinatorial background Kπ pair. Since the background is suppressed compared to the D^0 signal due to the HFT topological cuts, the overall efficiency correction is modified in reference to the D^0 signal. This was accounted for by assigning a probability based on the ratio of raw signal (S) and background (B) yields to the total yield (S+B) in the invariant mass distribution. This approach results in a weight applied to each D^0 candidate + hadron pair that has a term for the probability that the pair contains a real D^0-meson, and a term for the probability that the pair contains a background Kπ pair mistaken for a real D^0. The full pair-weight is defined in Eq. 5.19,

$$pair\ weight = \frac{B}{S+B}\frac{\overline{\epsilon_K\epsilon_\pi\epsilon_h}}{\epsilon_K\epsilon_\pi\epsilon_h} + \frac{S}{S+B}\frac{\overline{\epsilon_{D^0}\epsilon_h}}{\epsilon_{D^0}\epsilon_h}, \tag{5.19}$$

where the $\overline{\epsilon_K\epsilon_\pi\epsilon_h}$ and $\overline{\epsilon_{D^0}\epsilon_h}$ are included to ensure that the pair weights are approximately maintained when summed over all pairs.

5.2.3 Calculation of SE and ME Pair Distributions

When a Kπ-hadron pair is formed for $\rho_{SE}(\Delta\eta, \Delta\phi)$ or $\rho_{ME}(\Delta\eta, \Delta\phi)$, the pair angular differences are calculated on $(|\Delta\eta|, |\Delta\phi|)$, and the pair is recorded in all four quadrants on $(\Delta\eta, \Delta\phi)$. This procedure is called *symmetrization*. The symmetrization procedure is justified because of the symmetry in the collision system (i.e. two colliding nuclei of same species and energy), and the fact that STAR is a mid-rapidity detector (i.e. our η dependence is symmetric and our system is rotationally invariant about ϕ). The symmetrization is only useful to make the correlations visually more intuitive.

The symmetrization must be taken into account when calculating errors and doing fitting. The efficiency correction is also applied to each individual pair, and the copies. Any one "pair" increments a bin on $(\Delta\eta, \Delta\phi)$ by one, with a weight being applied as calculated in Eq. 5.19. Eq. 5.20 shows the basic approach of calculating the SE distribution in a generic multiplicity, V_z, and D^0 p_T sub-bin,

$$\rho_{SE}(\Delta\eta, \Delta\phi) = \sum_{1}^{N_{events}} \sum_{j=1}^{N_{trks}} (pair\ weight)\ pair_j(\Delta\eta, \Delta\phi), \tag{5.20}$$

where j is the track index for the associated hadron list (containing N_{trks} number of hadrons), and N_{events} is the number of events containing a D^0 in the generic set of sub-bins and is equal to the number of D^0 candidates in that bin (since any candidate event only ever has one D^0 candidate).

When the ME buffer is filled for a given multiplicity and V_z sub-bin, event mixing can take place for that bin. The procedure is the same as for the SE calculation, except that a single candidate Kπ pair is paired with associated hadrons from multiple mixed events ($N_{mix-events} = 5$). Eq. 5.21 shows the same calculation as in Eq. 5.20,

$$\rho_{ME}(\Delta\eta, \Delta\phi) = \sum_{1}^{N_{K\pi events}} \sum_{1}^{N_{mix-events}} \sum_{j=1}^{N_{trks}} (pair\ weight)\ pair_j(\Delta\eta, \Delta\phi) \tag{5.21}$$

where N_{trks} is the number of tracks in the mixed-event, $N_{mix-events}$ is the number of mixed-events used, and $N_{K\pi events}$ is the number of D^0 tracks in the buffer at that time.

5.2.4 D^* Correction

In Section 5.1 the calculation of the correlations from the signal region and from the sideband regions were discussed. The sideband correlations are meant to estimate the correlation contribution from the D^0 combinatorial background from the invariant mass spectrum and also mentioned the contribution from the decay of the D^*.

The predominate decay of the charged, excited D-meson state is $D^* \rightarrow D^0 + \pi_{soft}$ (BR = 67%) [84]. From charm quark fragmentation calculations, about 25% of the charm formed in the initial hard-scattering interactions forms a $D^{*\pm}$-meson, which can then subsequently decay into the trigger D^0. The lifetime of the $D^{*\pm}$-meson yields a $c\tau \sim 12$ nm, while the medium only exists for ~ 10 fm/c, so the $D^{*\pm}$ decay happens well outside the medium. Given the charm fragmentation, about 17% of the D^0 sample could be coming from the decay of a $D^{*\pm}$ and therefore must be accounted for.

The reason to specifically correct for the D^* contribution is because of the kinematics of the decay, which makes the angular distribution on $(\Delta\eta, \Delta\phi)$ peaked around (0,0), as can be seen in the PYTHIA results below.

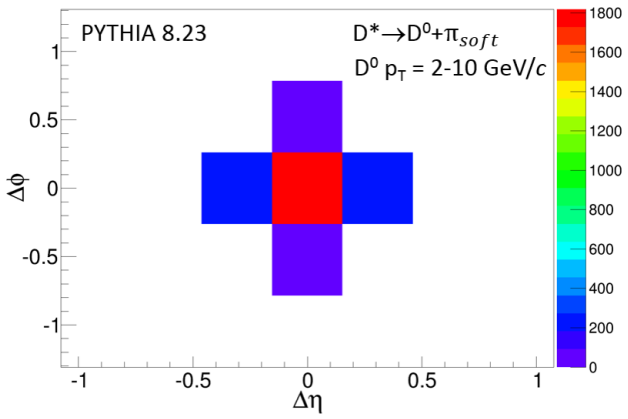

Figure 5.4: D^* decay distribution on $(\Delta\eta, \Delta\phi)$ between the daughter D^0 and π_{soft}.

The reason this contribution is problematic is that the π_{soft} coming from the decay of the D^* is produced outside the medium, and therefore does not interact with it. This produces a D^0+hadron correlated pair that does not contain information about the interactions with the medium, but clearly affects the final correlation structure, making the jet-like peak have an artificially larger amplitude. The issue is sketched in the cartoon in figure 5.5.

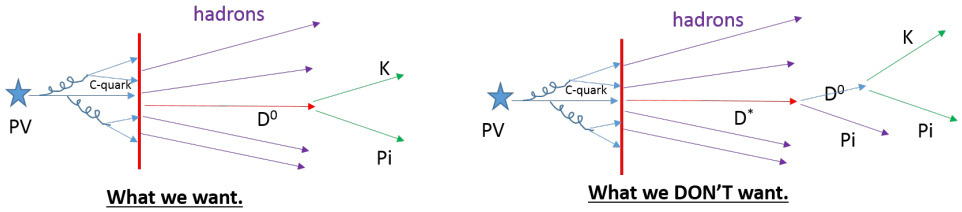

Figure 5.5: Cartoon of a D^0 created promptly, then decaying (left) vs. a D^0 produced alongside a π_{soft} from the decay of a D^* outside the medium (right).

As noted in the derivation of the correlation quantity, the D^* correction is carried out in the same way as is done for the invariant mass background

present in the correlations, meaning the ρ_{SE} and ρ_{ME} distributions are calculated for the D^0+pion pairs falling in the invariant mass window of the $D^{*\pm}$ and the correlation functions are computed.

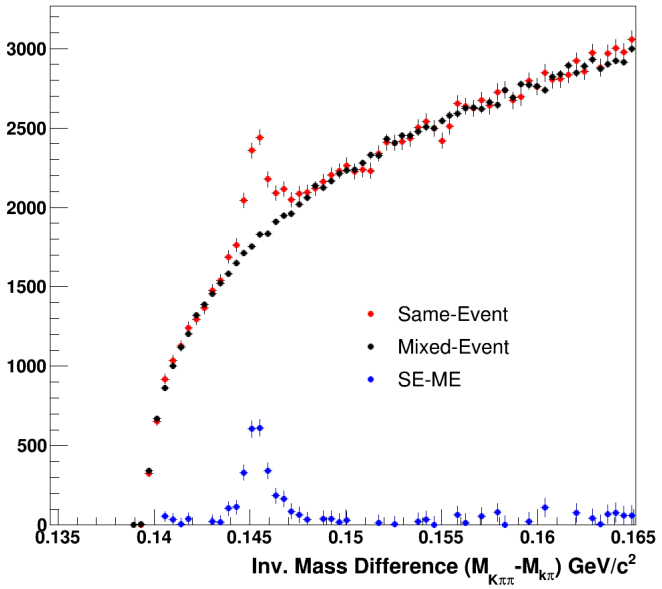

Figure 5.6: Invariant mass distribution for the D^*, plotted as the difference in mass between the $M_{K\pi\pi}$ and the $M_{K\pi}$. This histogram is for the 0-20% most central bin. The normalization is done by normalizing the ME distribution to the SE distribution in the range 0.15 to 0.16 GeV/c^2 using the ratio of the integral of the SE and ME distributions in that range.

The invariant mass combination shown in figure 5.6 is calculated, and a $D^{*\pm}$ candidate is identified when the invariant mass of a D^0-candidate + π (identified with the TPC) falls within the range $M_{K\pi\pi_s} - M_{K\pi} = 0.143 - 0.147$GeV/c^2. When that condition is met, the $(\Delta\eta, \Delta\phi)$ ordered-pair is calculated for the D^0-candidate + π and is binned in a separate histogram. The set of π that satisfy this invariant mass condition are then referred to as π_{soft}.

5.2.5 Correlation Results

In practice, the correlations for the three terms in Eq. 5.13 are all calculated in a very similar way, with the "trigger" and "associated" tracks coming from different sources, depending on the "band" in question. The three possible sources, as mentioned before, are the "signal", "sideband" and "D^*" bands. In every case, separate SE and ME histograms are calculated for each of the four total bands. In figure 5.7 below are examples of SE distributions from each of the four bands and the D^* correlation.

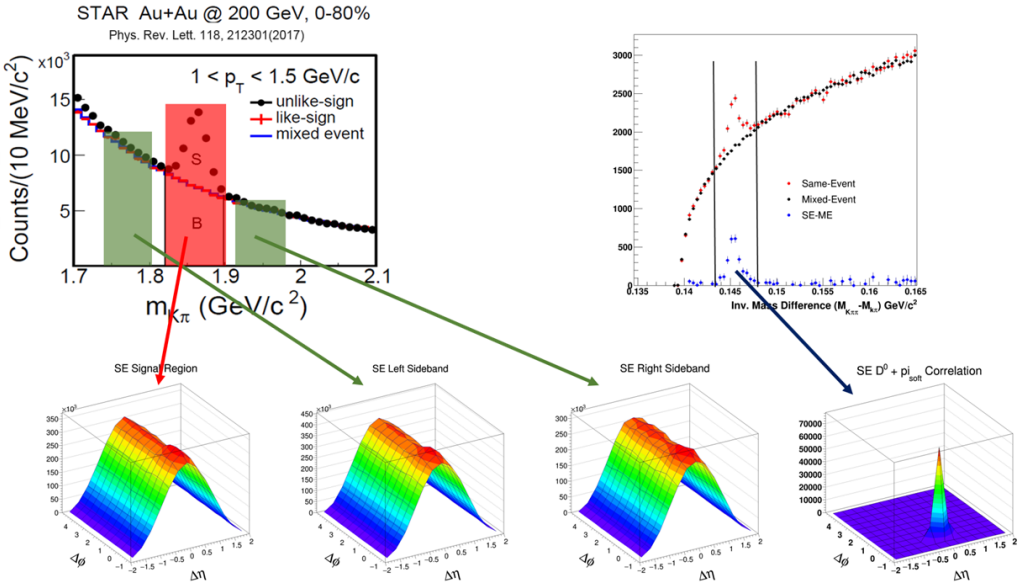

Figure 5.7: Same-event distributions for all unlike-sign bands and the $D^* \rightarrow D^0 + \pi_{soft}$ (as pictured: Left-most is the left side-band contribution, the second is the signal region, third is from the right side-band, and the right-most plot is from the D^*).

These correlations are calculated in the sixteen multiplicity and ten V_z sub-bins for each of the four contributions (signal region, left side-band, and

right side-band), with the exception of the $D^{*\pm}$, which was only calculated for the three centrality bins. This is done for both the same-event and mixed-event distributions, yielding a total of 966 histograms! The whole procedure is illustrated below with a sub-set of histograms for one multiplicity bin.

5.2.5.1 Detailed View of Computation of Correlation Function

For this section the focus will be on the computation of the correlation function for the signal region in the D^0 invariant mass distribution. The individual ρ_{SE} and ρ_{ME} histograms for all of the V_z-bins, and one of the multiplicity sub-bins are shown in Figs. 5.8 and 5.9.

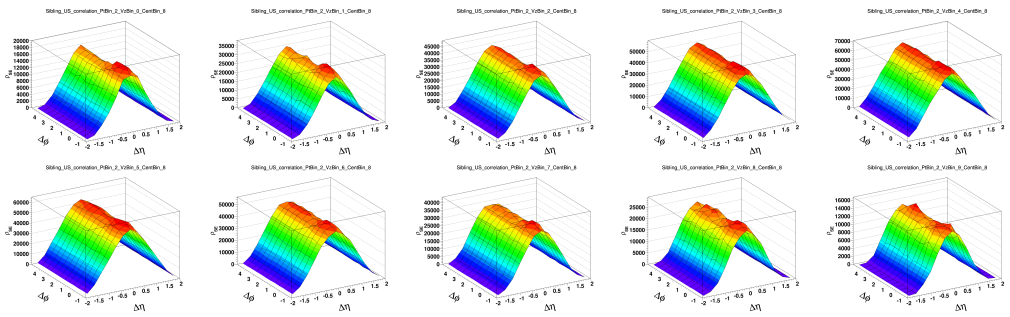

Figure 5.8: Same-event distributions for the signal region of D^0 invariant mass distribution for multiplicity bin 9 (see Table 5.2). The V_z-bins in the plots above increase from left-to-right, top-to-bottom, with the ranges shown in Table 5.1.

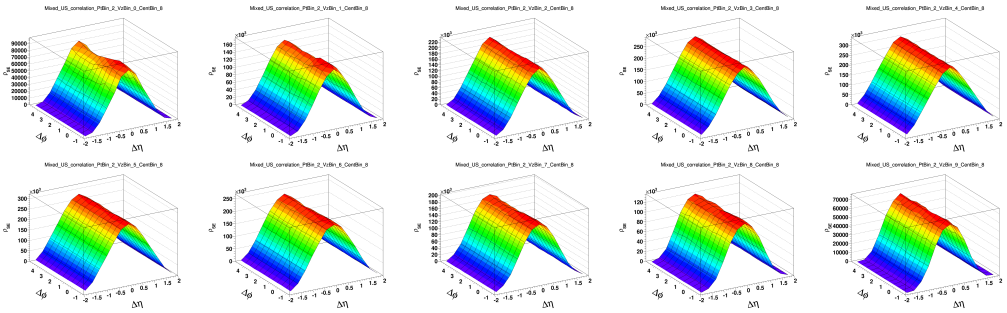

Figure 5.9: Mixed-event distributions for the signal region of D^0 invariant mass distribution for multiplicity bin 9 (see Table 5.2). The V_z-bins in the plots above increase from left-to-right, top-to-bottom, with the ranges shown in Table 5.1.

These histograms are then used to calculate the quantity $\Delta\rho$ for each of the sub-bins on V_z, as shown in Fig. 5.10.

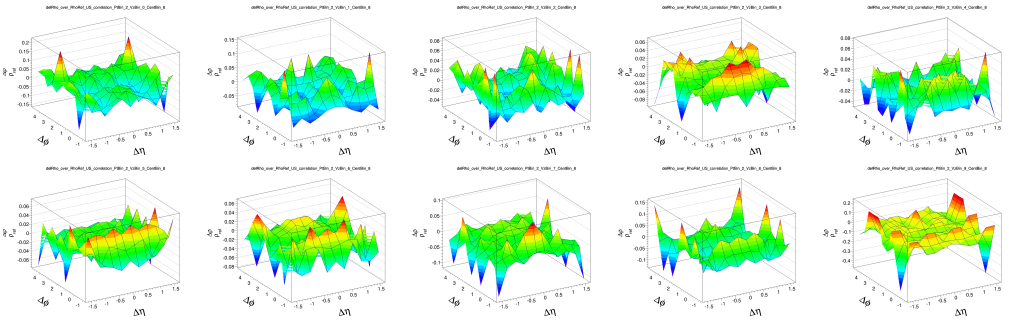

Figure 5.10: $\frac{\Delta\rho}{\rho}$ distributions for the signal region of D^0 invariant mass distribution for multiplicity bin 9 (see Table 5.2). The V_z-bins in the plots above increase from left-to-right, top-to-bottom, with the ranges shown in Table 5.1.

Once the $\Delta\rho/\rho_{ref}$ histograms are calculated for a particular multiplicity bin in the various V_z bins the histograms can be summed along V_z, since this dependence is only important for the acceptance correction. The sum over V_z is carried out using a weight factor based on the number of pairs for each

histogram, and is defined in Eq. 5.22,

$$\frac{\Delta\rho}{\rho_{ref}}(V_z - integrated) = \sum_{i=1}^{10}\left(w_i \frac{\Delta\rho}{\rho_{ref\ i}}\right), \tag{5.22}$$

where the weight factor, w_i is defined as $w_i = \sum_{i=1}^{10}\left(\frac{N_{SE,i}}{N_{SE,V_z-total}}\right)$, where $N_{SE,i}$ and $N_{SE,V_z-total}$ are the total pair counts in histogram "i" and the total pair counts in all ten histograms combined, respectively. The results of this summation can be found for all of the multiplicity bins (2-16, bin 1 is dropped due to trigger bias) in Fig. 5.11.

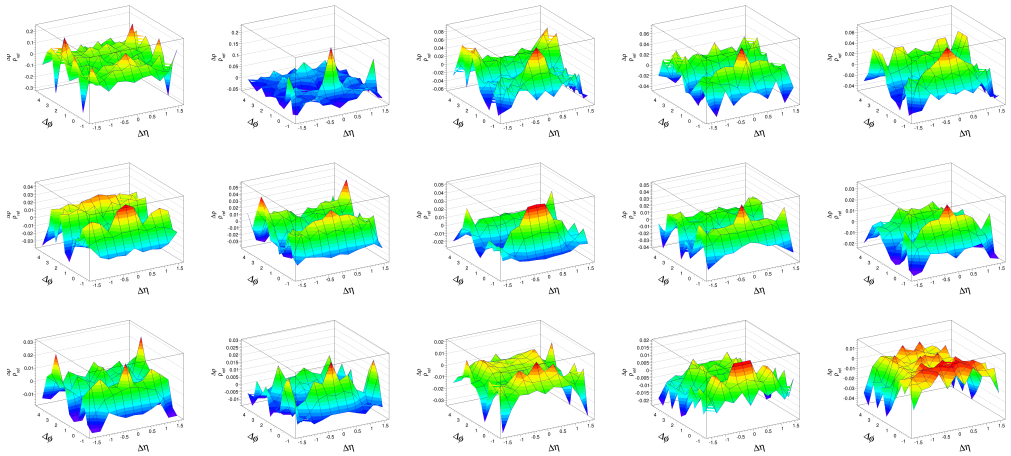

Figure 5.11: $\frac{\Delta\rho}{\rho}$ distributions for the signal region of D^0 invariant mass distribution for all multiplicity bins, increasing left-to-right, top-to-bottom (see Table 5.2).

These histograms represent the full procedure for obtaining the correlations for a given source (in this case, the signal region). This procedure is repeated for the side band correlations in the same manner as described above. The

results for this procedure for the left and right side bands are shown in Figs. 5.12 and 5.13, respectively.

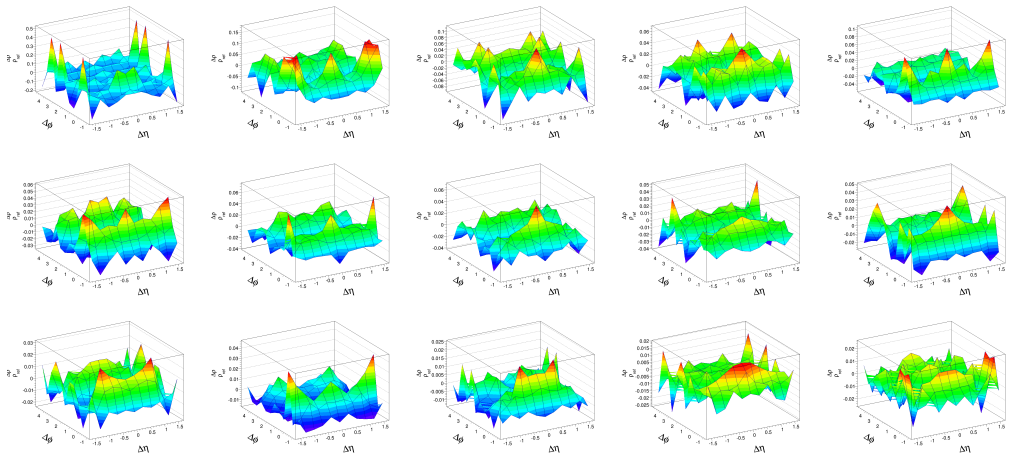

Figure 5.12: $\frac{\Delta\rho}{\rho}$ distributions for the left side band region of D^0 invariant mass distribution for all multiplicity bins, increasing left-to-right, top-to-bottom (see Table 5.2).

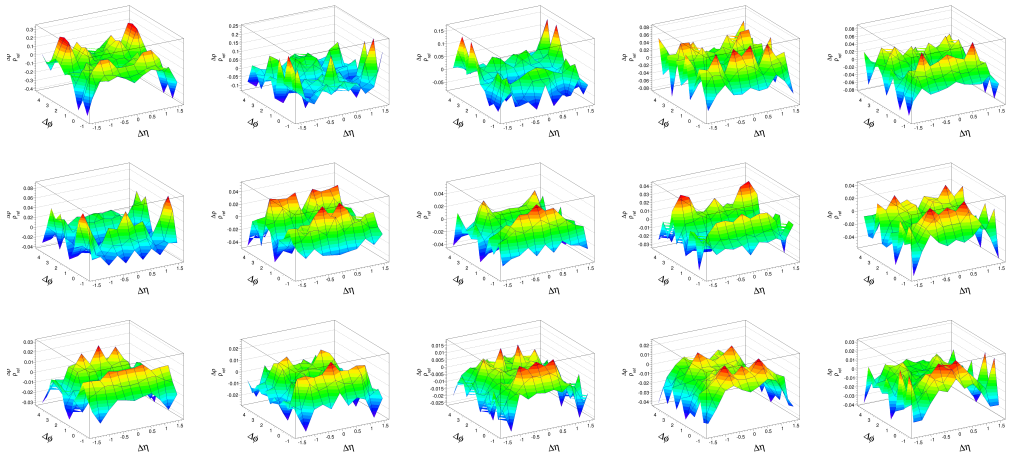

Figure 5.13: $\frac{\Delta\rho}{\rho}$ distributions for the right side band region region of D^0 invariant mass distribution for all multiplicity bins, increasing left-to-right, top-to-bottom (see Table 5.2).

Once this is done, the side band contributions are averaged, scaled by B/S (as in Eq. 5.4), and then subtracted from the signal region contribution, as shown in Fig. 5.14.

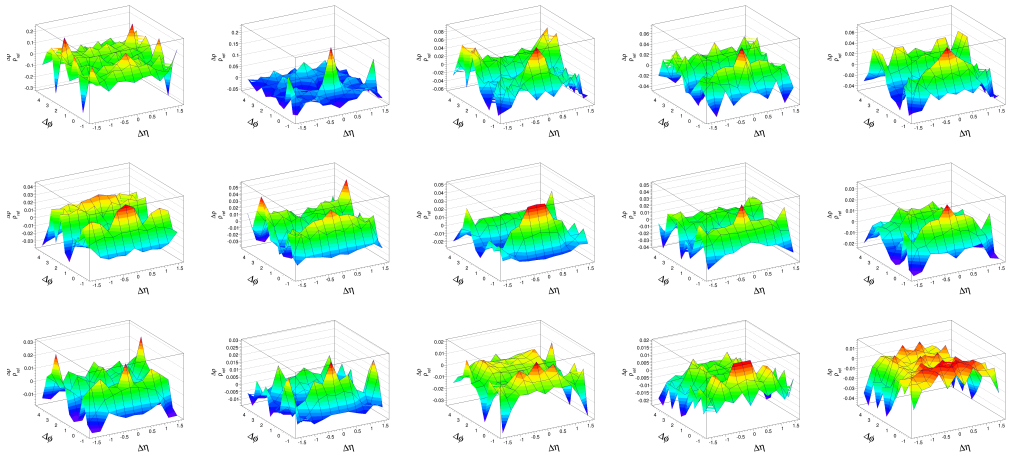

Figure 5.14: $\frac{\Delta\rho}{\rho}$ distributions with the background correlation from the invariant mass distribution subtracted.

Now that the correlations are calculated with the invariant mass background subtracted, integration over the multiplicity sub-bins to the final three centrality bins is done. The weight factor applied in Eq. 5.22 is also applied to this summation, but in each of the three centrality bins individually. The result of this is shown in Fig. 5.15.

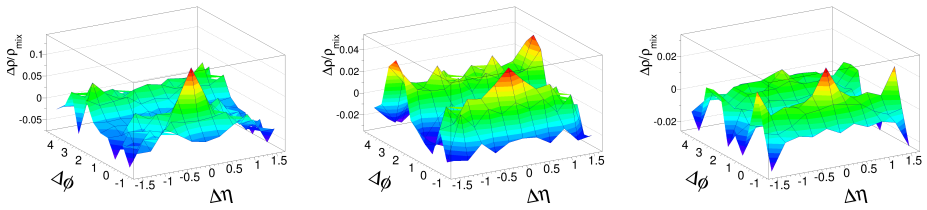

Figure 5.15: Invariant mass background subtracted correlations in three centrality bins: 50-80% (left), 20-50% (middle), and 0-20% (right).

With the final invariant mass background subtracted correlations, the correction for the D^* contribution can be carried out. Fig. 5.16 shows the D^* correlations calculated using the third term of Eq. 5.4.

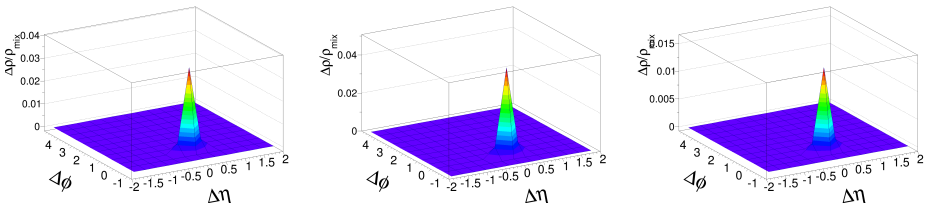

Figure 5.16: $D^0 + \pi_{soft}$ correlations from D^* decay in three centrality bins: 50-80% (left), 20-50% (middle), and 0-20% (right).

Once the D^* contribution is subtracted, the final correlations are obtained in Fig. 5.17.

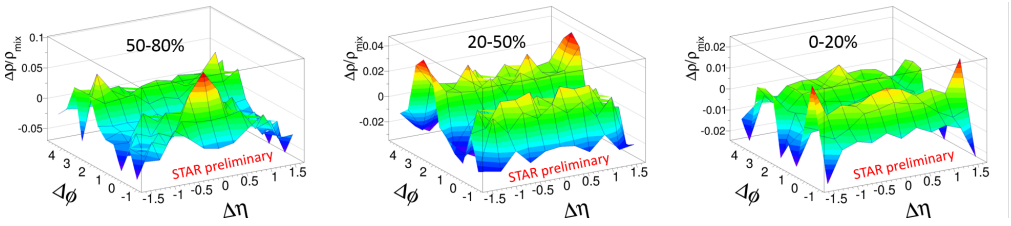

Figure 5.17: Final, fully corrected correlations.

5.3 Fitting of Correlation Results

In order to extract the underlying dynamics from these correlations, the correlation structures and their evolution with centrality must be quantified. To do this, a simple fit-function containing the fewest number of terms to get the best chi-square per degree of freedom and the minimum overall residuals from fitting was used,

$$fit(\Delta\eta,\Delta\phi) = A_{offset} + 2A_{Quadrupole} * \cos(2\Delta\phi) + A_{NS} e^{-.5\frac{\Delta\eta^2}{(\sigma_{\Delta\eta})^2}} e^{-.5\frac{\Delta\phi^2}{(\sigma_{\Delta\phi})^2}} + A_{AS} e^{-.5\frac{\Delta\eta^2}{(\sigma_{\Delta\eta})^2}} e^{-.5\frac{(\Delta\phi-\pi)^2}{(\sigma_{\Delta\phi})^2}} + periodicity\ on\ \Delta\phi. \tag{5.23}$$

The terms in the fit model include a near-side 2D Gaussian, describing the jet-like peak seen at small angles in $(\Delta\eta, \Delta\phi)$, a quadrupole term, which is related to v_2 (see appendix), and an away-side 2D Gaussian. In most two-particle correlations, $\Delta\eta$-dependence is not observed on the away-side, but there is no reason to assume *a priori* that there is none. The constant offset exists in all angular correlation measures, since these measures are controlled by an arbitrary normalization (in the present case, the pair-normalization defined as α). Some analyses refer to the constant offset term as the "baseline". The periodicity on $\Delta\phi$ refers to the need to make the NS and AS $\Delta\phi$-dependent Gaussian terms periodic, which is done by repeating the Gaussian every 2π radians (e.g. for the NS, there would be a Gaussian at -2π, 0, 2π, etc.). A pictorial representation of the various terms in the fit function is shown in Fig. 5.18.

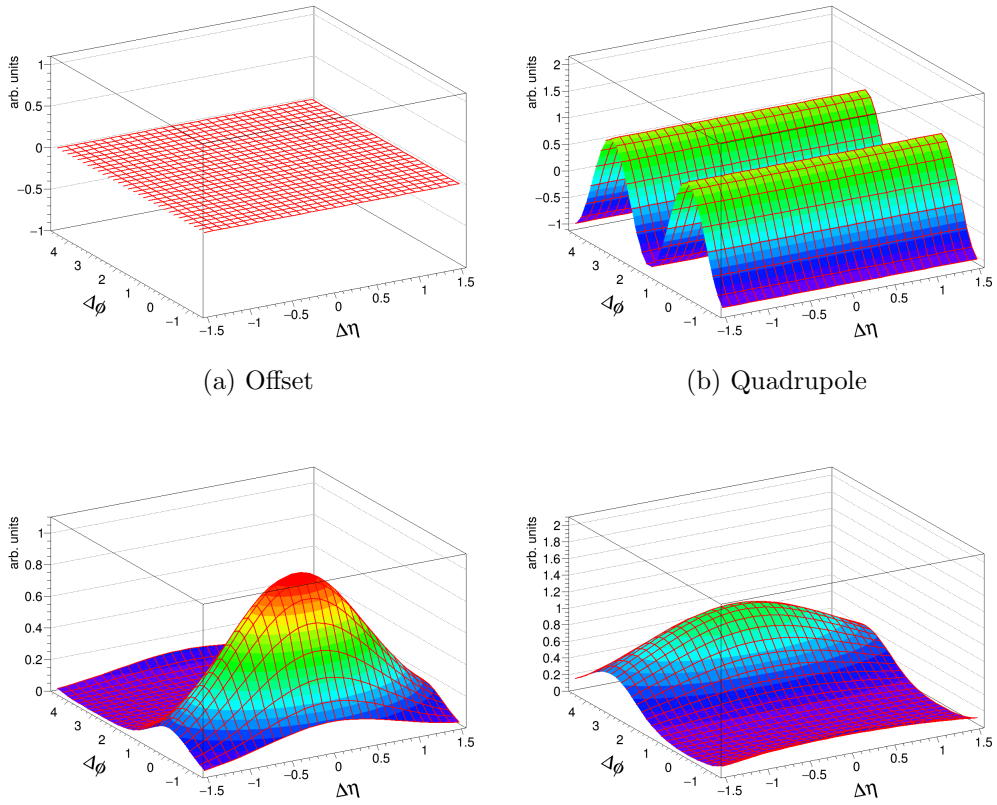

(a) Offset

(b) Quadrupole

(c) Near-side Gaussian

(d) Away-side Gaussian

Figure 5.18: 3D depiction of fit-function terms used in the fit for the D^0+hadron correlation function.

In order to fit all of the data, parameter bounds need to be chosen for the ROOT [89] fitter to find a χ^2-minimum. For simple fits with high-statistics data, this is generally straight-forward. However, with statistically limited data and a two-dimensional fit, we employed a more quantitative approach to ensure good starting values for the fitter, and to check for multiple minima in the χ^2-space that may indicate alternate solutions. This was done by mapping the χ^2-space for each parameter and locating the minimum or minima. An

example of this is shown in Fig. 5.19.

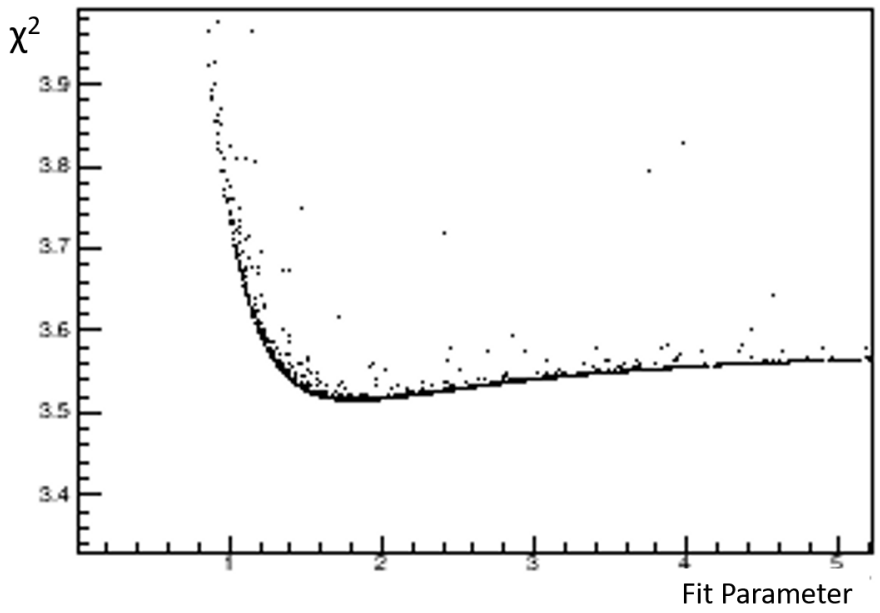

Figure 5.19: Generic χ^2/DOF vs. parameter value plot used for setting fit-parameter boundaries for the Root Minuit fitter. These plots are also used to determine if there are multiple χ^2-minima.

These plots are generated for each fit in the three centrality bins, and for each of the parameters used in the fits. The Downhill-Simplex method [86], or "amoeba" method was used to sample 10,000 starting values for the parameters. For each starting value, the fit-function is computed using those values and compared to the data to calculate the χ^2 per degree of freedom. For each step, the χ^2/DOF and parameter-value ordered-pair is plotted, and the result is what is seen in Fig. 5.19. These plots can then be used to pick the starting values for the ROOT fitter by inspection. This method also serves as an independent check on the fit-parameters found using the ROOT fitter.

An important thing to note in doing the fitting is how the width on $\Delta\phi$ on the away-side evolves with centrality. Since the $\Delta\phi$ coordinate system is periodic, if the Gaussian becomes broad it approaches a limit ($\sigma_{\Delta\phi} \sim 1$) where it mathematically becomes a dipole term $\propto \cos(\Delta\phi)$, as shown in Eq. 5.24,

$$\begin{aligned} &\sum_{k-odd} exp[-(\Delta\phi - k\pi)/2\sigma^2] = \\ &\frac{\sigma}{\sqrt{2\pi}}\left(1 + 2\sum_{m=1}^{\infty}(-1)^m e^{(-m^2\sigma^2/2)}\cos(m\Delta\phi)\right) = \\ &\frac{\sigma}{\sqrt{2\pi}}\left(1 - 2e^{(-\sigma^2/2)}\cos(\Delta\phi) + ...\right), \end{aligned} \tag{5.24}$$

plus a constant, which gets absorbed by the constant used in the fit.

The 50-80% data were fit using the fit model in Eq. 5.23 as is. The 20-50% data used the dipole term in place of the 2D away-side Gaussian, since the away-side was too broad on $\Delta\phi$ to be described by a Gaussian, and approached the dipole limit. Furthermore, to better constrain the near-side fit, the fit was performed only using the offset, dipole and quadrupole terms on the away-side, and then those values were fixed in the full-fit. The 0-20% data were fit using a dipole in place of the Gaussian on $\Delta\phi$, but required the $\Delta\eta$-dependent portion of the Gaussian to best describe the data, which is qualitatively not flat on $\Delta\eta$ within statistical uncertainty.

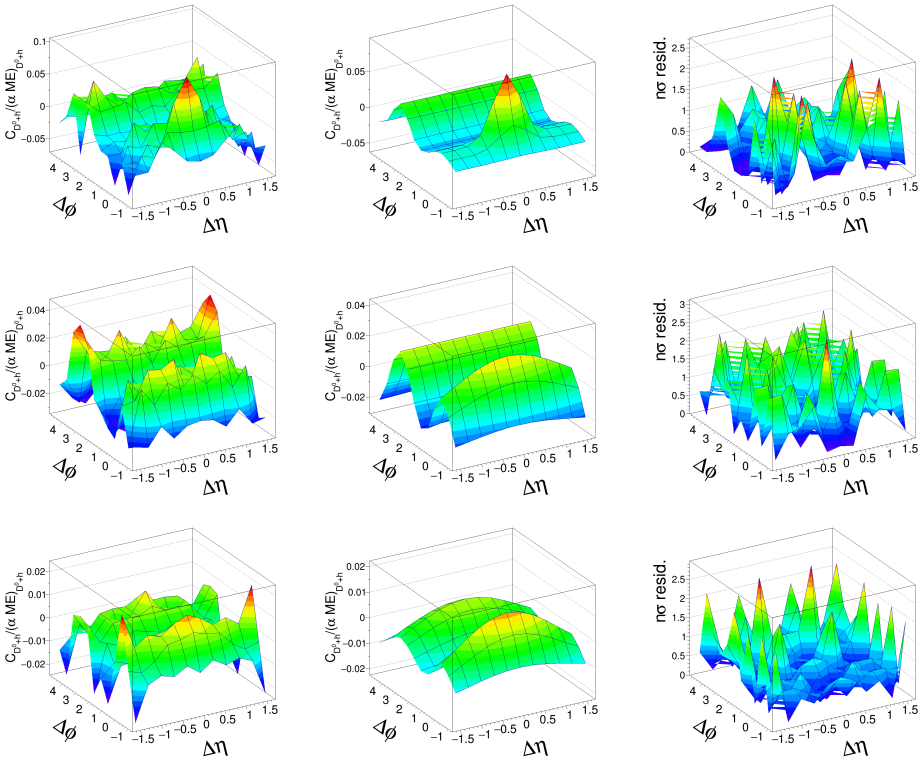

Figure 5.20: Final fits in all centrality bins: Top: 50-80%, Middle: 20-50%, Bottom: 0-20%. The left column is the data, the second column is the fit, and the third column is a map of the $n\sigma_{fluctuation}$ in each $(\Delta\eta, \Delta\phi)$ bin (i.e. (data-fit)/error). The $n\sigma_{fluctuation}$ is a quantitative version of a standard residual, and is more informative.

The residuals in all three cases have fluctuations on the order of 3σ or less, with the exception of the $(\Delta\eta, \Delta\phi) = (0, 0)$ bin in the 20-50% centrality bin, which is addressed in the systematic uncertainty section. Table 5.6 shows all of the fit-parameters and associated errors.

$\sigma_{AA}(\%)$	50-80	20-50	0-20
A_0	-0.0118($\pm$0.0044)	-0.0093($\pm$0.0014)	-0.0117($\pm$0.0025)
$A_{\rm Q}$	0.0040($\pm$0.0028)	0.0066($\pm$0.0030)	0.0($\pm$0.0022)
$A_{\rm NS}$	0.091($\pm$0.019)	0.0374($\pm$0.0035)	0.0439($\pm$0.0061)
$\sigma_{\Delta\eta,NS}$	0.312($\pm$0.078)	1.37($\pm$0.35)	1.24($\pm$0.30)
$\sigma_{\Delta\phi,NS}$	0.350($\pm$0.068)	0.663($\pm$0.064)	0.754($\pm$0.073)
$A_{\rm AS}$	0.0295($\pm$0.0196)	-	-
$\sigma_{\Delta\eta,AS}$	-	-	1.33($\pm$0.25)
$\sigma_{\Delta\phi,AS}$	0.55($\pm$0.14)	-	-
$A_{\rm D}$	-	0.0158($\pm$0.0117)	0.0191($\pm$0.0037)
χ^2/DoF	.93	1.90	1.17

Table 5.6: Model parameters and statistical errors (in parentheses) for 200 GeV Au+Au D^0 + hadron correlations as discussed in the text.

5.4 Extraction of the Near-Side Associated Yield (per-trigger yield)

Since the correlations in the present analysis are normalized *per-particle pair*, we need to apply a proper normalization in order to extract an associated yield on the near-side. The associated yield refers to the average number of particles associated with the the charm-quark in the jet-like correlation structure on the near-siide - or more simply, "how many particles appear nearby the charm quark (or D^0-meson) as it traverses the medium." This procedure is done using a different approach than other per-trigger correlation analyses, where the correlation is normalized differently, and the final correlation divided by the number of trigger particles (c.f. [87, 88]). This is because of the needed efficiency correction for the number of triggers (the D^0 efficiency correction) and to make a direct comparison with the published LF results more straight-forward, since the same normalization was used in that analysis [83].

The associated hadron yield per D^0 trigger in the NS jet-like correlation structure, $Y_{\mathrm{NS-peak}}/N_{D^0}$, is estimated by summing that portion of the correlation fitting model in Eq. 5.23 over the $(\Delta\eta, \Delta\phi)$ acceptance, including efficiency and acceptance corrections, and dividing by the efficiency corrected number of D^0 mesons, N_{D^0}, used in the analysis. Starting with this more conventional per-trigger yield,

$$Y_{\mathrm{NS-peak}}/N_{D^0} = \frac{1}{N_{D^0}} \times \sum_{\Delta\eta,\Delta\phi} \left[\frac{\Delta n_{D^0+h}}{\frac{\alpha_{D^0+h}\rho_{\mathrm{ME},D^0+h}}{\alpha_{D^0+h}\rho^{\mathrm{max}}_{\mathrm{ME},D^0+h}}} \right]_{\mathrm{NS-peak}} , \tag{5.25}$$

where Δn_{D^0+h} is the number of correlated $D^0 + h^{\pm}$ pairs in bins $(\Delta\eta, \Delta\phi)$, which is equal to $\delta_{\Delta\eta}\delta_{\Delta\phi}\Delta\rho_{D^0+h}$, where $\delta_{\Delta\eta}, \delta_{\Delta\phi}$ are the bin widths on $\Delta\eta$ and $\Delta\phi$. $\alpha_{D^0+h}\rho^{\mathrm{max}}_{\mathrm{ME},D^0+h}$ is the maximum value of the normalized, mixed-event pair distribution, evaluated by averaging over the $\Delta\phi$ bins for $\Delta\eta = 0$. The ratio in the denominator represents the mixed-event distribution normalized to 1.0 at the maximum. Rearranging Eq. 5.25 gives

$$\begin{aligned} Y_{\mathrm{NS-peak}}/N_{D^0} &= \frac{\alpha_{D^0+h}\rho^{\mathrm{max}}_{\mathrm{ME},D^0+h}}{N_{D^0}} \times \sum_{\Delta\eta,\Delta\phi} \delta_{\Delta\eta}\delta_{\Delta\phi} \left[\frac{\Delta\rho_{D^0+h}}{\alpha_{D^0+h}\rho_{\mathrm{ME},D^0+h}} \right]_{\mathrm{NS-peak}} \\ &= \frac{\alpha_{D^0+h}\rho^{\mathrm{max}}_{\mathrm{ME},D^0+h}}{N_{D^0}} V_{\mathrm{NS-peak}} \end{aligned} \tag{5.26}$$

where the summation in the first line of Eq. 5.26 is defined as $V_{\mathrm{NS-peak}}$, the volume of the NS peak correlation structure, represented by the integral of the NS 2D Gaussian in the fit-model in Eq. 5.23,

$$V_{\mathrm{NS-peak}} = \int_{\Delta\eta \text{ accep}} d\Delta\eta \int_{-\pi}^{+\pi} d\Delta\phi A_{NS} e^{-.5\frac{\Delta\eta^2}{(\sigma_{\Delta\eta})^2}} e^{-.5\frac{\Delta\phi^2}{(\sigma_{\Delta\phi})^2}} \tag{5.27}$$

The ratio on the RHS of the second line of Eq. (5.26) can be estimated from the measured numbers of D^0 and $D^0 + h^{\pm}$ ME pairs, provided both numerator

and denominator are corrected for inefficiencies. A simpler form is given in the following in which the required efficiency corrected quantities are more readily obtained.

The maximum value of the efficiency corrected, normalized mixed-event density equals the fraction of the total number of $D^0 + h^\pm$ pairs in a $\Delta\eta = 0$, $\Delta\phi$ bin per bin area. This is given by

$$\alpha_{D^0+h}\rho^{\max}_{\mathrm{ME},D^0+h} = \frac{\varepsilon\bar{n}_{D^0}\bar{n}_h}{\delta_{\Delta\eta}\delta_{\Delta\phi}}\frac{2[1-1/(2N_{\Delta\eta})]}{N_{\Delta\eta}N_{\Delta\phi}} \tag{5.28}$$

where ε is the number of events in the centrality bin, $\bar{n}_{D^0}$ and $\bar{n}_h$ are the efficiency corrected, event-averaged number of D^0 mesons and associated $h^\pm$ particles in the acceptance, $N_{\Delta\eta}$ and $N_{\Delta\phi}$ are the numbers of $\Delta\eta$ and $\Delta\phi$ bins, where $N_{\Delta\eta}$ is odd and $N_{\Delta\phi}$ is a multiple of four. The second ratio on the RHS of Eq. (5.28) is the fraction of $D^0 + h^\pm$ pairs in an average $\Delta\eta = 0$, $\Delta\phi$ bin. The efficiency corrected number of D^0 mesons is $N_{D^0} = \varepsilon\bar{n}_{D^0}$. The ratio in Eq. (5.26) simplifies to

$$\begin{aligned}\frac{\alpha_{D^0+h}\rho^{\max}_{\mathrm{ME},D^0+h}}{N_{D^0}} = \frac{2\bar{n}_h[1-1/(2N_{\Delta\eta})]}{N_{\Delta\eta}N_{\Delta\phi}\delta_{\Delta\eta}\delta_{\Delta\phi}} &= \frac{\bar{n}_h}{2\pi\Omega_\eta}\left(1-\frac{1}{2N_{\Delta\eta}}\right) \\ &\approx \frac{dN_{\mathrm{ch}}}{2\pi d\eta}\left(1-\frac{1}{2N_{\Delta\eta}}\right)\end{aligned} \tag{5.29}$$

where $N_{\Delta\eta}N_{\Delta\phi}\delta_{\Delta\eta}\delta_{\Delta\phi} = 4\pi\Omega_\eta$, and Ω_η is the single particle pseudorapidity acceptance which equals 2 units for the STAR TPC. In the last step we assumed that the number of K, π daughters is much less than the event multiplicity, such that $\bar{n}_h$ is well approximated by event multiplicity N_{ch}. The final NS-peak correlated yield per D^0 trigger is given by

$$Y_{\mathrm{NS-peak}}/N_{D^0} = \frac{dN_{\mathrm{ch}}}{2\pi d\eta}\left(1-\frac{1}{2N_{\Delta\eta}}\right)V_{\mathrm{NS-peak}} \tag{5.30}$$

where $dN_{\mathrm{ch}}/2\pi d\eta$ is efficiency corrected [67].

5.5 PYTHIA Analysis

Since there were no data available for pp 200 GeV with the HFT at STAR, PYTHIA 8.23 was used to generate a pp baseline analysis. The tune used for PYTHIA was obtained from two studies in [73] and [74]. It involved setting the value beamRemnant:primordialkt = 1.0 to soften the D^0 p_T distribution to match data from AuAu 200 GeV collisions measured at STAR. The the tune settings used are the defaults in PYTHIA for the Monash 2013 tune.

After the tune was adjusted, D^0+hadron correlations were calculated in the same way as was done in the Au+Au run14 data presented in this thesis, with the contributions from $D^* \to D^0 + \pi_{soft}$ removed. One major difference is that the secondary decays from the K^0_S and the Λ-baryon were removed. All other trigger and associated cuts were imposed as detailed in Sec. 4.1.2, except those cuts related to specific detectors (e.g. HFT requirement, number of TPC fit points, etc.). The results for the data and the fitting are seen in Fig. 5.21. The fit model used is similar to Eq. 5.23, but without the quadrupole term and with a generalized Gaussian for the NS peak, as the NS peak in PYTHIA is significantly sharper,

$$\begin{aligned} fit(\Delta\eta, \Delta\phi) = A_{offset} + A_{NS} e^{-.5\left(\frac{\Delta\eta^2}{(\sigma_{\Delta\eta})^2}\right)^{\beta}} e^{-.5\left(\frac{\Delta\phi^2}{(\sigma_{\Delta\phi})^2}\right)^{\beta}} \\ + A_{AS} e^{-.5\frac{\Delta\eta^2}{(\sigma_{\Delta\eta})^2}} e^{-.5\frac{(\Delta\phi-\pi)^2}{(\sigma_{\Delta\phi})^2}} + periodicity\ on\ \Delta\phi. \end{aligned} \tag{5.31}$$

Parameter of fit	Value
A_0	-0.210($\pm$0.00398)
$A_{\rm NS}$	1.398($\pm$0.0135)
$\sigma_{\Delta\eta,NS}$	0.397($\pm$0.003918)
$\sigma_{\Delta\phi,NS}$	0.451($\pm$0.003676)
$A_{\rm AS}$	0.345($\pm$0.00437)
$\sigma_{\Delta\phi,AS}$	0.808($\pm$0.0138)
β (Gen. Gaussian Parameter)	.829($\pm$.0123)
$Y_{\rm NS,peak}/N_{D^0}$	0.987($\pm$0.023)
χ^2/DoF	1.77

Table 5.7: Model parameters and statistical errors (in parentheses) for D^0 + hadron correlations from 10M PYTHIA p+p $\sqrt{s} = 200$ GeV events.

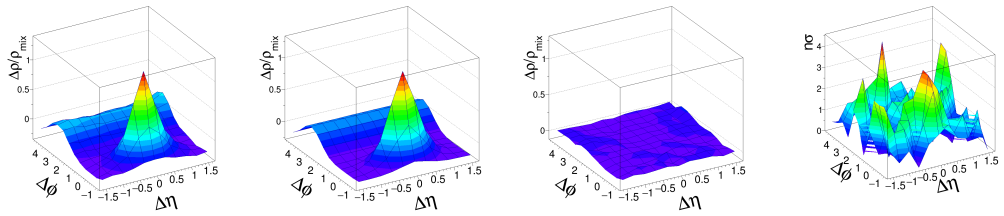

Figure 5.21: Simulated data and fits for D^0+hadron correlations from PYTHIA. The left column is the data, the second column is the fit, the third is the residual and the fourth column is a map of the $n\sigma_{fluctuation}$ in each $(\Delta\eta, \Delta\phi)$ bin.

Chapter 6

Systematic Uncertainties

There are several sources of possible systematic uncertainty in this analysis, which are summarized below:

- Secondary hadron contamination
- B-meson feed down
- D^0 yield determination (calculation of S and B)
- D^0 Decay Topological Cuts
- Sideband Variations (widths and range)
- Pileup
- Fits using various $(\Delta\eta, \Delta\phi)$ bins
- D^* correction
- Efficiency Correction

Systematic uncertainties in the 2D $D^0 + h^{\pm}$ correlation data are discussed first. The impact of these uncertainties in the data, plus uncertainties in the mathematical representation of the fitting model on the properties of the correlations are discussed next.

The largest source of systematic uncertainty is that caused by non-primary (secondary) particle contamination in the associated charged-particle sample originating from weak decay daughter particles and secondary particle

production (mainly pions and protons) in the detector material. Tracks which pass the associated hadron requirements in Sec. 4.1.2.2, contain an estimated 12% contamination from these secondary particle sources [67]. The effect of this secondary contamination on the di-hadron correlations was estimated to be no more than 3% in minimum-bias Au+Au collisions at 200 GeV [67]. In the present analysis secondary particle contamination is mostly removed from the $(K\pi)$ D^0-decay candidates which include stringent secondary vertex reconstruction requirements. Furthermore, any secondary particle contamination in the $(K\pi)$ candidate sample will be included in the random $[K\pi]$ background. The remaining contamination in the associated particle sample is assumed to produce one-half the systematic uncertainty of that in the di-hadron correlation analysis, or $\pm 1.5\%$ in overall amplitude.

centrality bin	Dipole	Quadrupole	NS Volume	NS Phi	NS Eta
peripheral	N/A	± 1.5%	± 1.5%	± 0%	± 0%
mid-central	± 1.5%	± 1.5%	± 1.5%	± 0%	± 0%
central	± 1.5%	± 0	± 1.5%	± 0%	± 0%

Table 6.1: Table of systematics from secondary hadron contamination. Note: the central bin quadrupole systematic is not quoted as % error.

Contributions from B-meson feed-down to D^0-mesons was estimated to be 4% of the D^0 sample in minimum-bias 200 GeV Au+Au collisions [38]. These decays occur well outside the collision volume such that the daughter D^0 has little opportunity to develop correlations with particle in the medium. Due to the large Q-value of the decay process, the D^0 daughter momentum vector will likely be shifted significantly away from the parent momentum, resulting in some dissipation of any correlations the parent B-meson may have had with the associated hadrons. We consider two limits: (1) the B-meson

+ hadron correlations are similar to the $D^0 + h^{\pm}$ correlations and are passed on unaffected to the daughter D^0 and associated hadrons; (2) any B-meson + hadron correlations are fully dissipated in the decay process. The resulting systematic uncertainty ranges from zero to a +4% overall increase in the correlation amplitude as listed in Table 6.2.

centrality bin	Dipole	Quadrupole	NS Volume	NS Phi	NS Eta
peripheral	N/A	+4.0%	+4.0%	+0%	+0%
mid-central	+4.0%	+0%	+4.0%	+0%	+0%
central	+4.0%	+0.0	+4.0%	+0%	+0%

Table 6.2: Table of systematics from B-meson feed-down contamination. Note: the central bin quadrupole systematic is not quoted as % error.

Secondary vertex reconstruction of the $D^0 \to K\pi$ decay requires five cut-parameters (see Sec. 4.1.2.1). The final correlations are insensitive to reasonable variations in each cut-parameter about the set of values which were optimized with respect to the statistical significance of the D^0 signal in the invariant mass distribution [38]. The one exception is the daughter kaon minimum DCA to the primary vertex which has marginal effects beyond statistical fluctuations. These effects on the correlations were similar in each centrality and were approximated with a small 1D Gaussian on $\Delta\eta$ with amplitude ± 0.002 and width $\sigma = 0.5$. Including this uncertainty in the data affected the fit model results as listed in Table 6.3.

centrality bin	Dipole	Quadrupole	NS Volume	NS Phi	NS Eta
peripheral	N/A	± 7.0%	± 3.8%	± 1.8%	± 0.9%
mid-central	± 1.9%	± .79%	+1.4%, -0%	± 0.8%	± 17.0%
central	± 8.4%	± 0	+0.7%, -0%	± 2.6%	± 23.0%

Table 6.3: Table of systematic topological cut variations. Note: the central bin quadrupole systematic is not quoted as % error.

Uncertainties in the magnitude of the $D^\star \rightarrow D^0\pi_s$ contamination in the $(\Delta\eta, \Delta\phi) = (0, 0)$ bin were estimated by varying the background subtracted from the $(M_{K\pi\pi_s} - M_{K\pi})$ invariant mass distribution where as much as 20% variation in the $D^\star$ yield was allowed, given the background distribution statistics. This uncertainty only affects the $(\Delta\eta, \Delta\phi)$ = (0,0) angular bin. The resulting uncertainty in the (0,0) bin affected the fit model quantities as listed in Table 6.4.

centrality bin	Dipole	Quadrupole	NS Volume	NS Phi	NS Eta
peripheral	N/A	± 2.4%	± 1.0%	± 2.2%	± 2.9%
mid-central	± 0%	± 0%	± 3.2%	± 4.8%	± 9.2%
central	± 10.5%	± 0	± 18.3%	± 9.2%	± 13.1%

Table 6.4: Table of systematics from D^* background. Note: the central bin quadrupole systematic is not quoted as % error.

Other systematic uncertainties were estimated by varying the analysis parameters and examining the resulting changes in the final correlations. These variations included: (1) adjusting the side-band widths and positions, (2) including or not including the D^0 and hadron reconstruction efficiency corrections, (3) including or not including two-particle reconstruction inefficiency

corrections, (4) adjusting the dE/dx particle identification cuts for the D^0 decay daughter candidates, (5) including or excluding decay daughter candidates which have ambiguous particle identification, (6) adjusting the background in the $(K\pi)$ invariant mass distribution used for the D^0 signal estimate (2-3% variation in signal yield), (7) adjusting the widths of the primary vertex position and event multiplicity sub-bins used for the mixed-event distributions, and (8) including or not including corrections to the assigned event-wise multiplicity (for centrality determination) due to tracking efficiency dependence on primary vertex position in the TPC and beam+beam collision luminosity during each data acquisition run period. Each systematic uncertainty source was studied and found to have negligible effects on the correlations, *i.e.* less than the statistical uncertainties. Systematic effects in the associated particle sample due to multiple-event track pileup in the TPC [67] were suppressed by requiring at least three HFT space points to be assigned to the charged particle track. The fast-response of the HFT detector, specifically the IST layer (a few hundred ns [82]) suppresses pre- and post-trigger event tracks from the associated particle sample. Other systematic effects associated with detector stability during runs, Coulomb multiple scattering in the detector material, and finite momentum resolution were considered previously and found to be negligible [67].

The above systematic uncertainties in the correlation data directly affect the fitting model parameters. Secondary particle contamination is assumed to contribute a $\pm 1.5\%$ uncertainty to each amplitude parameter. The B-meson feed-down contamination adds a $0\% - +4\%$ uncertainty range to each correlation amplitude. The small 1D Gaussian resulting from variations in the D^0 decay daughter kaon DCA cut was added (both ± 0.002 amplitudes

were used) to the correlation data and refitted with the nominal fitting model. The average magnitudes of the parameter changes resulting from the ± 0.002 amplitude perturbation were included in the systematic uncertainties in the model parameters. Similarly, the systematic uncertainty in the (0,0) angular bin due to the $D^\star \to D^0\pi_s$ contamination correction contributed to the model parameter uncertainties.

The choices of fitting model elements also produce systematic uncertainties in the deduced properties of the angular correlations. Defining the model elements in Sec. 5.3 as the base-line, or nominal model, we considered several alternate models which, for the most part, produce similar quality descriptions of the correlation data. These include: (1) adding a sextupole $A_S \cos(3\Delta\phi)$ to the nominal model, (2) replacing the same-side 2D jet-like Gaussian with a Lorentzian $\times$ Gaussian, (3) replacing the same-side peak with a platykurtic raised cosine $\times$ Gaussian function, and (4) replacing the away-side dipole with an away-side 2D Gaussian. The Lorentzian $\times$ Gaussian model element is given by

$$A\frac{(\Gamma_\eta/2)^2}{\Delta\eta^2+(\Gamma_\eta/2)^2}\left(e^{-\Delta\phi^2/2\sigma_\phi^2}+e^{-(\Delta\phi-2\pi)^2/2\sigma_\phi^2}\right) \tag{6.1}$$

with fit parameters A, Γ_η and σ_ϕ. The raised cosine $\times$ Gaussian term is

$$(A/2)\left[1+\cos\left(\Delta\eta\pi/\sigma_\eta\right)\right]\left(e^{-\Delta\phi^2/2\sigma_\phi^2}+e^{-(\Delta\phi-2\pi)^2/2\sigma_\phi^2}\right) \tag{6.2}$$

when $|\Delta\eta| \leq \sigma_\eta$ and zero otherwise. The fit parameters are A, σ_η and σ_ϕ. The same periodic Gaussian distribution on $\Delta\phi$ in the nominal model was assumed here. For the alternate model with an away-side 2D Gaussian the azimuth component is also required to be periodic.

The Lorentzian $\times$ Gaussian model fit to the 50-80% correlations was significantly poorer than the nominal fit and the other alternate model fits.

These alternate fit results were therefore not used. The nominal plus sextupole alternate model fit to the 0-20% data resulted in a χ^2 minimum fit which produced an unphysical dipole correlation (very narrow on $\Delta\eta$) and was discarded. All other alternate model fit results had comparable χ^2 and residuals as the nominal fit model results and did not produce unphysical model elements and were therefore used in the systematic error estimates. No one model element dominated the final uncertainties.

Systematic uncertainties were estimated for the dipole and quadrupole amplitudes, the same-side peak volume per D^0 trigger and its Gaussian width along azimuth (σ_ϕ) and rms width along $\Delta\eta$, and for the peripheral bin the away-side Gaussian volume per D^0 trigger per unit $\Delta\eta$. For each of these quantities the mean and standard deviation of the nominal and alternate model results were calculated. The resulting systematic uncertainties relative to the nominal fit values were adjusted to encompass the mean $\pm$ one standard deviation. The resulting systematic uncertainties are asymmetric.

centrality bin	Dipole	Quadrupole	NS Volume
peripheral	N/A	+16.0%, -2.8%	+1.9%, -10.9%
mid-central	+0%, -0%	+0%, -0%	+1.9%, -1.3%
central	+0.5%, -2.4%	+.00043, -.00007	+0.8%, -4.7%

centrality bin	NS Phi	NS Eta
peripheral	+0.7%, -3.9%	+2.6%, -15.2%
mid-central	+0.2%, -0.3%	+6.1%, -19.0%
central	+0.3%, -2.2%	+3.4%, -20.01%

Table 6.5: Table of systematics from ambiguity in fit model. Note: the central bin quadrupole systematic is not quoted as % error.

An additional contribution to the fitting model uncertainty due to al-

ternate $(\Delta\eta, \Delta\phi)$ bin choices was estimated by fitting the data with 11 $\Delta\eta$ bins and 16 $\Delta\phi$ bins in place of the nominal 13 $\times$ 12 bins. The alternate binning continued to cover 2 units in pseudorapidity and 2π in azimuth. The above correlation properties were calculated using the nominal fitting model in Eq. (5.23) applied to the re-binned data. These results were compared to the nominal correlation quantities and the differences were included in the final systematic uncertainties.

Each of the above positive and negative systematic uncertainties in the correlation quantities resulting from the six sources of systematic uncertainty discussed in this section were added in quadrature, where positive and negative errors were combined separately. The nominal fitting model results, statistical fitting errors and the combined systematic uncertainties are listed in Table 6.6.

centrality bin	Dipole	Quadrupole	NS Volume
peripheral	N/A	+18.9%, -9.7%	+6.1%, -11.7%
mid-central	+4.7%, -2.43%	+6.1%, -4.7%	+32.7%, -32.5%
central	+14.3%, -14.0%	+.00043, -.00007	+20.1%, -20.2%

centrality bin	NS Phi	NS Eta
peripheral	+2.9%, -4.9%	+4.0%, -15.5%
mid-central	+9.6%, -9.6%	+21.1%, -27.7%
central	+10.5%, -10.7%	+27.1%, -33.5%

Table 6.6: Table of total systematics. Note: the central bin quadrupole systematic is not quoted as % error.

The effect of the efficiency correction was evaluated by comparing the final correlations with and without the prescribed efficiency correction in 5.2.2. This comparison was done by calculating the bin-wise residual $n\sigma$ for the nom-

inal (with efficiency correction) correlation and the non-efficiency corrected correlations. Fig. 6.1 depicts this comparison.

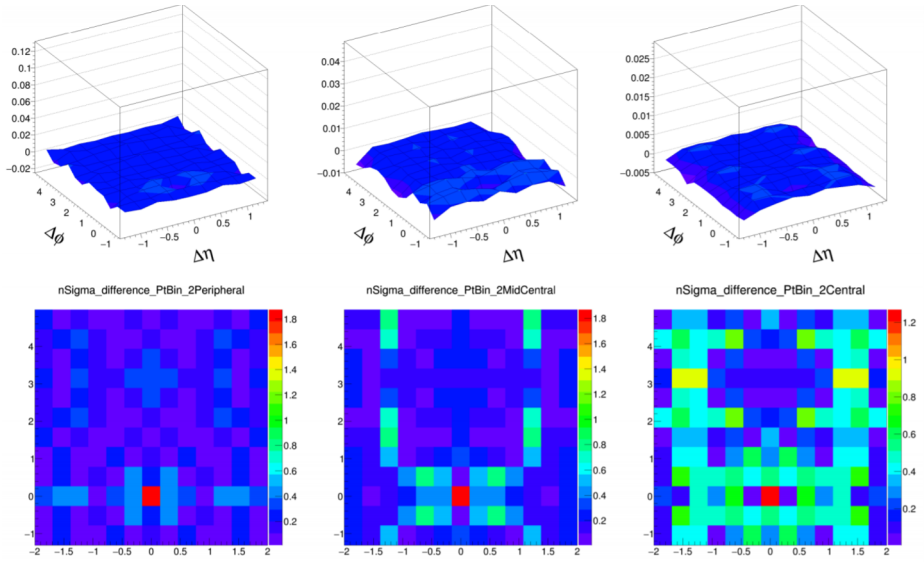

Figure 6.1: Shown here are the comparison plots for the correlations with and without the efficiency correction derived in Sec. 5.2.2. The top row are simple residuals, and the bottom row are the $n\sigma$ residuals for each bin. The nσ fluctuations do not exceed 2σ for any bin, indicating little difference in the correlations with or without the efficiency correction.

These results confirm that the inefficiencies cancel in the ratio ρ_{SE}/ρ_{ME}, as expected.

Chapter 7

Final Results

7.1 Results

The final results of the fitting on the near-side (NS) and the NS associated yield can be seen in figures 7.1, 7.2, and 7.3. The data are shown alongside the PYTHIA 8.23 results (see Sec. 5.5) in all of the figures.

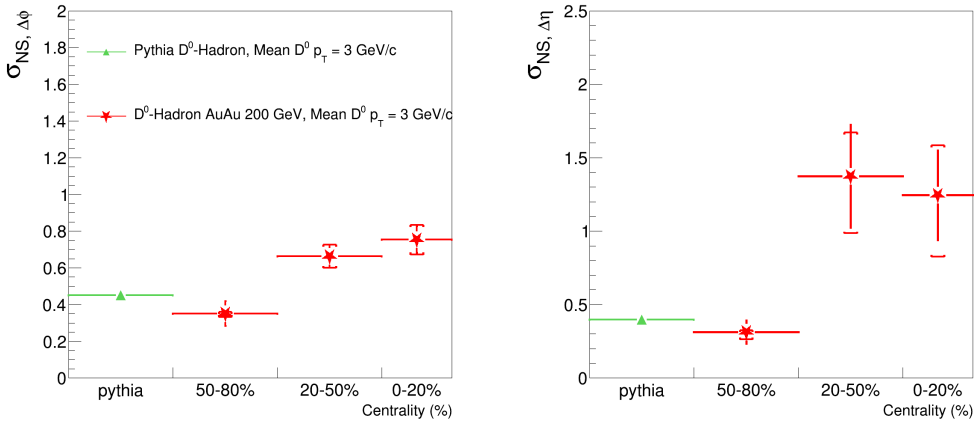

Figure 7.1: Near-side Gaussian $\Delta\phi$ and $\Delta\eta$ width as a function of centrality.

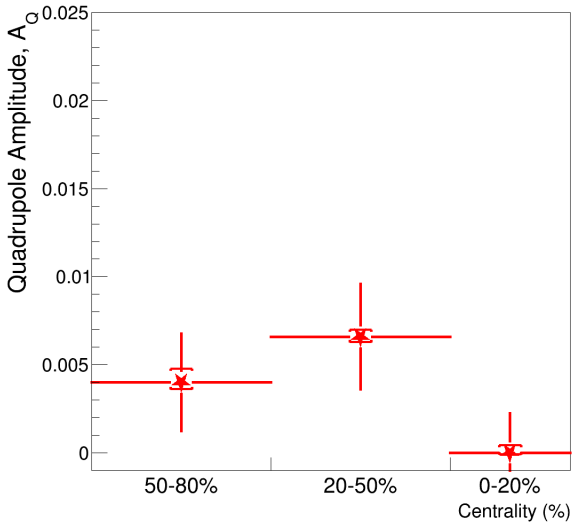

Figure 7.2: Quadrupole amplitude from fit as a function of centrality.

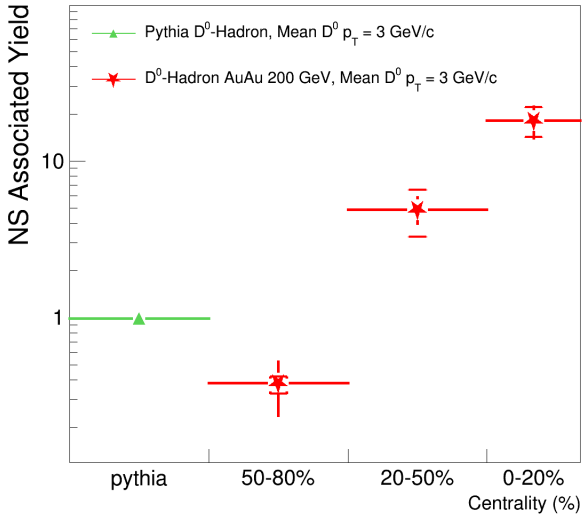

Figure 7.3: Near-side Associated Yield as calculated in Eq. 5.30.

The data indicate broadening on both $\Delta\eta$ and $\Delta\phi$, implying substantial in-

teractions of the charm-jet with the medium for a D^0 with a mean-$p_T \sim 3$ GeV/c with growing system size (centrality). The quadrupole amplitude has a maximum value in the 20-50% centrality bin, which is expected given that a mid-central collision has a maximum ellipticity, which translates to the final state as a larger quadrupole amplitude. The NS associated yield increases over an order of magnitude from peripheral to central collisions, further indicating substantial interactions of the charm-quark or meson with the medium. These interactions are the sum of both the radiative energy loss due to gluon bremsstrahlung, collisional energy loss in the medium, and possible medium effects on the vacuum fragmentation. Due to our limited statistics, approximate separation of the energy loss mechanisms via different p_T bins was not possible (and is not possible exactly, as determination of the exact onset of these mechanisms is not experimentally attainable).

7.2 Comparison to Light-Flavor Di-hadron Correlations

Aside from reporting the evolution of the correlation function and associated fit-parameters with centrality, we can also compare the correlations to a light-flavor unidentified di-hadron correlations, using an unidentified hadron trigger at a similar mean-p_T to our D^0. The light-flavor results used in this section are reported in [83]. The light-flavor di-hadron correlations were computed from STAR Au+Au $\sqrt{s_{\rm NN}} = 200$ GeV collisions contained in the same dataset as in [67]. The only difference between the analysis in [67] and [83] is that the latter analysis was also carried out using trigger-p_T (or rather, y_T) bins, and show the resulting fit parameters as a function of both y_T and centrality. The correlations in [83] were fit with a function similar to that used in [67] and in the present thesis,

$$fit(\Delta\eta, \Delta\phi) = B_0 + B_{2D} exp\Bigg\{ -\frac{1}{2}\Bigg[\left(\frac{\Delta\eta}{\sigma_{\Delta\eta}}\right)^2 + \left(\frac{\Delta\phi}{\sigma_{\Delta\phi}}\right)^2\Bigg]\Bigg\} + B_D\{1+\cos(\Delta\phi-\pi)\}/2 + 2B_Q\cos(2\Delta\phi). \tag{7.1}$$

The results from extracting the fit parameters from [83] are plotted along with the results from this thesis analysis in Figs. 7.4, 7.5, and 7.6.

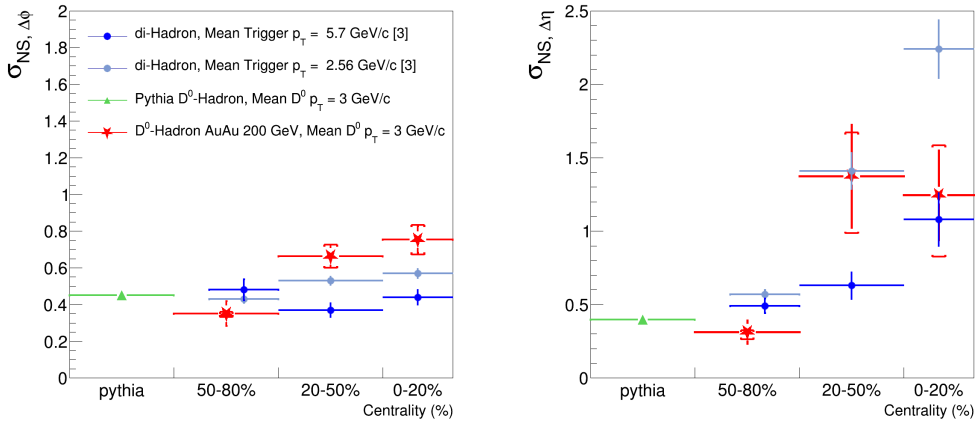

Figure 7.4: NS Gaussian $\Delta\phi$ (left) and $\Delta\eta$ (right) width as a function of centrality. The red data points are from this thesis analysis, while the blue points are from [83].

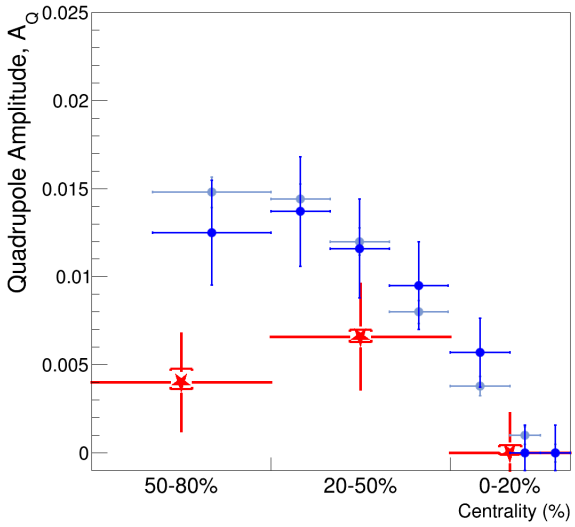

Figure 7.5: Quadrupole amplitude from fit as a function of centrality. The red data points are from this thesis analysis, while the blue points are from [83].

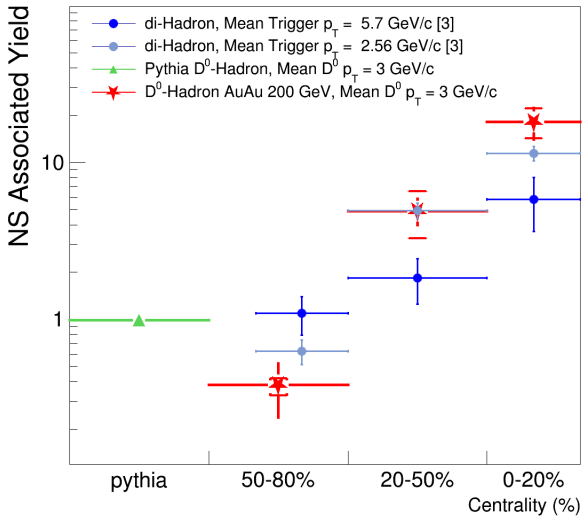

Figure 7.6: NS Associated Yield as calculated in Eq. 5.30. The red data points are from this thesis analysis, while the blue points are from [83].

The trends observed in the present analysis and in [83] exhibit some interesting similarities. The widths on $\Delta\eta$ and $\Delta\phi$ for a LF trigger hadron of similar mean-p_T to our D^0 trigger show a similar amount of broadening from peripheral to mid-central. However, the error bars for the D^0+hadron $\Delta\eta$ width correlation results make conclusions difficult from mid-central to central collisions. The evolution of the NS associated yield, however, shows quite good agreement within errors over all centralities. This indicates that the sum of the interactions experienced by charm in the medium are very similar to that experienced by a LF quark at a similar mean-p_T.

7.3 Discussion

Based on the results for the centrality dependence of the NS widths (related to the charm-jet shape) and associated yield (both are related to the net interactions of the charm-quark with the medium), it is clear that the charm quark experiences significant interactions in the heavy-ion collision medium. This is especially startling given that the NS jet-like correlation peak also experiences some surface bias due to the trigger p_T restriction, where the NS jet sees less medium than the away-side jet. The evolution of the away-side (AS) correlation structure is also indicative of strong medium interactions since broadening on $\Delta\phi$ is observed as a function of centrality. The broadening of the AS correlation structure is indicative of the recoil-jet (which likely contains the other charm-quark from the original $c\bar{c}$ pair) experiencing more medium interactions, reinforcing the idea that the NS is at least partially surface-biased.

The notable similarities between the LF correlations and the D^0+hadron correlations - especially involving the NS associated yield - are interesting be-

cause of the significant mass of the charm-quark compared to the light-quarks. The mass dependence, however, is specifically related to the radiation of gluons (gluon bremsstrahlung) via the dead-cone effect [40]. Given our low D^0 p_T, it is unlikely we are observing much of this effect as our energy-loss is likely dominated by collisional energy-loss in the medium. If we were seeing significantly more energy-loss due to gluon radiation, we would expect to see a suppression of the jet-like correlation structures at small angles on $(\Delta\eta, \Delta\phi)$, since the dead cone effect predicts suppression of radiation at small angles for higher mass quarks. Some higher statistics analysis with a better separation of high and low p_T for the D^0 would certainly aid in our understanding of the energy-loss processes themselves.

Even though charm-quarks are formed in perturbative hard scatterings before medium formation, such as $gg \rightarrow c\bar{c}$, heavy quarks propagating through a partonic medium experience mostly non-perturbative collisional and radiative energy-loss interactions. The early-formation of the charm quarks (requiring pQCD - not *a priori* included in all models), and their higher mass compared to light quarks makes their inclusion in heavy-ion models challenging.

Many models can reproduce nuclear modification factor (R_{AA}) and v_2 results for charged-hadrons (and light quarks) simultaneously, with only a few accomplishing the same feat for charm. Some notable models/groups that can do this for charm are the Parton Hadron String Dynamics (PHSD) model [90], and the larger effort by the Rapid Reaction Task Force (EMMI RRTF) at GSI [92] which aims to bring together many theorists working with heavy flavor for a joint effort to extract heavy flavor transport coefficients from the available data.

What is interesting, however, is that up to this point very few models have used the wealth of correlation data to constrain parameters - most use only the azimuthal anisotropy parameters, such as v_2 and higher-order harmonics, and the nuclear modification factor. These parameters alone have, thus far, not provided the necessary constraints to falsify models with fundamentally different underlying physics assumptions. Two-particle correlation measurements that provide information on both $\Delta\eta$ and $\Delta\phi$ give access to the correlations coming from jets and fragmentation, and collective flow along with the transverse momentum dependence and centrality dependence (as in the case of [67, 83]). Using measured LF correlations, forthcoming correlations on transverse rapidity from STAR [71], and the HF correlations presented in this thesis, a wealth data will be available that are sensitive to the underlying dynamics of heavy-ion collisions that will enable us to hone-in on the correct physical understanding of this complicated system, and further our understanding of QCD in a highly non-perturbative regime.

Chapter 8

Summary and Outlook

8.1 Summary and Conclusions

This thesis presents two-dimensional D^0+hadron angular correlations projected on $(\Delta\eta, \Delta\phi)$ for the first time in heavy-ion collisions. The analysis was done using the $\sqrt{s_{\rm NN}} = 200$ GeV Au+Au collision data collected by the STAR experiment in 2014, using the newly installed HFT for reconstruction of the D^0-meson.

The correlations computed in this thesis exhibit qualitatively similar structures to previous two-particle correlation studies using LF hadrons. Quantitative information was extracted from these correlations using a multi-parameter fit model chosen to reflect the geometric structures present in the correlations and to simultaneously measure the contributions from jets and bulk sources.

The peripheral (50-80%) data indicate that the jets formed from charm are essentially unmodified in shape in our D^0 p_T range (2-10 GeV/c) in Au+Au collisions when compared to PYTHIA, although PYTHIA predicts a larger yield of associated particles from vacuum fragmentation. This unmodified jet shape is in coincidence with a non-zero value for D^0 v_2 in that same centrality bin. The mid-central (20-50%) results indicate modification of the charm-jet structure, seen as broadening in both $\Delta\eta$ and $\Delta\phi$, as well as an increase in the average number of associated hadrons. The D^0 v_2 measured in this centrality

bin is consistent with the published STAR measurement using the event-plane analysis method. The central (0-20%) data similarly indicate strong interactions of the charm-jet with the medium, while the v_2 is consistent with zero.

This analysis shows that jets containing charm quarks indeed experience modification as they traverse the medium formed in heavy-ion collisions. This is not just seen from the broadening of the jet-like peak on the near-side, but from the order-of-magnitude increase in the NS associated yield as a function of centrality, which indicates that the charm quark and/or hadron is interacting substantially with the medium via either collisions with other partons or radiation of gluons. The appearance of the NS $\Delta\eta$ elongation with centrality seen in LF correlations [67] - also known as the "ridge" - is now shown to occur in HF correlations.

Some theory calculations which correctly predict the available measurements of D^0 R_{AA} and v_2 indicate that the dominant energy-loss mechanism at the p_T of the D^0 presented in this thesis is from collisions with partons in the medium. Further differential measurements of correlations as a function of D^0-p_T could help to verify if this is the case.

8.2 Outlook and Future Measurements

The installation of the HFT in STAR enabled measurements with open heavy flavor that would have otherwise been impossible. Almost 1 billion Au+Au collision events were collected in 2014, and yet, that enormous dataset was still only barely able to deliver the necessary statistics for this thesis analysis, and only enabled a minimal amount of differential study (only as a function of centrality). The combination of the other Au+Au dataset containing the HFT (run 2016) with the present 2014 data would enable further differential

study of the correlations, most-notably as a function of D^0 transverse momentum.

With a sufficiently wide range of transverse momentum covered (and the necessary statistics), one could potentially isolate regions more kinematically prone to either the energy loss mechanism of collisions with other partons in the medium (lower p_T), or the radiation of gluons (higher p_T).

The up-and-coming sPHENIX experiment is designed around maximum capability in the reconstruction of jets and open heavy flavor. This could allow for more differential correlation studies with heavy flavor to be carried out, as well as studies using heavy-flavor tagged, fully-reconstructed jets. sPHENIX is being designed to take data at a very high luminosity, which will allow for incredibly high statistics to study these rare probes.

The study of heavy flavor and other hard probes (e.g. jets), in my view, is important for the heavy-ion physics community given that the theory and phenomenology are still sparse with respect to the inclusion of heavy flavor and other hard probes, as well as the interaction of these hard probes with the medium. Hard probes, being formed in the early collision stage and surviving well-after the medium dissipates, makes them perfect probes of the QGP. Heavy flavor quarks are evidently very much affected by the medium formed in heavy-ion collisions, and further experimental analysis will provide more constraints for models in the future, adding to our understanding of this very complicated state of QCD matter.

Appendix

Obtaining v_2 from the Quadrupole Amplitude

v_2 is the amplitude of the second Fourier component and is commonly ascribed to elliptic flow. The Fourier decomposition is performed on the single particle distribution projected on ϕ:

$$\frac{dN}{d\phi} = 1 + 2\sum_{n=1}^{\infty} v_n \cos(n(\phi - \Psi_R)) \tag{1}$$

Averaging the product of the $\frac{dN}{d\phi}$ decompositions for both the hadrons and the D^0 mesons yields,

$$\langle \frac{dN_D}{d\phi} \frac{dN_h}{d\phi} \rangle_{\Psi_R} = 1 + 2\sum_{n=1}^{\infty} v_n^D v_n^h \cos(n(\phi_D - \phi_h)) \tag{2}$$

where $\phi_D - \phi_h = \Delta\phi$. The n = 2 term is exactly the term used in the multi-parameter fit for this analysis.

$$\langle \frac{dN_D}{d\phi} \frac{dN_h}{d\phi} \rangle_{\Psi_R} = 1 + 2v_2^D v_2^h \cos(2\Delta\phi) + ... \tag{3}$$

Bibliography

[1] J. C. Collions and M. J. Perry, *Physical Review Letters* **34**, 1353 (1975)

[2] N. Cabibbo and G. Parisi, *Phys. Letters B* **59**, 67-69 (1975)

[3] M. Gell-Mann, *Physical Review* **3** (1962)

[4] George Zweig, CERN Report 8182/TH.401 (17 January 1964).

[5] V. E. Barnes et al., *Phys. Rev. Lett.* **12**, 204 (1964)

[6] M. Gell-Mann, *Physics Letters* **8**, 3 (1964)

[7] `https://commons.wikimedia.org/wiki/File:Meson_octet.png`

[8] M.Breidenbach et al., *Phys. Rev. Lett.* **23** (1969) 935

[9] R. P. Feynman, Photon-Hadron Interactions (W. A. Benjamin, New York, 1972)

[10] Harald Fritzsch and Murray Gell-Mann, *Proceedings of the XVI International Conference on High Energy Physics*, Chicago, 1972. Volume 2, p. 135

[11] H. D. Politzer, *Physical Review Letters* **30**, 13461349 (1973)

[12] D. J. Gross and F. Wilczek, *Physical Review Letters* **30**, 13431346 (1973)

[13] K. G. Wilson, *Phys. Rev. D* **10** (1974) 2445

[14] J. -E. Augustin et al, *Phys. Rev. Lett.* **33**, 1406 (1974)

[15] J. J. Aubert et al., *Phys. Rev. Lett.* **33**, 1404 (1974)

[16] S. W. Herb et al., *Phys. Rev. Lett.* **39**, 252 (1977)

[17] F. Abe et al. (CDF Collaboration), *Phys. Rev. Lett.* **74**, 2626 (1995)

[18] S. Abachi et al. (D0 Collaboration), *Phys. Rev. Lett.* **74**, 2422 (1995)

[19] G. Aad et al. (ATLAS Collaboration),*Physics Letters B* **716** 1, (2012); S. Chatrchyan et al. (CMS Collaboration), *Physics Letters B* **716** 1, (2012)

[20] MissMJ, `https://commons.wikimedia.org/wiki/File:Standard_Model_of_Elementary_Particles.svg`

[21] J. D. Bjorken, *Phys. Rev. D*, **27**, (1983)

[22] J.W. Harris and B. Muller, *Ann. Rev. Nucl. Part. Sci.* **46** (1996) 71

[23] F. Karsch. *Lattice QCD at High Temperature and Density.* Lecture Notes of Physics, vol. 583, 2002. arXiv:hep-lat/0106019.

[24] *Compact Stars in the QCD Phase Diagram VI*, Conference Poster, `http://indico.jinr.ru/event/csqcd2017`, Sep. 2017

[25] P. Koch, B. Muller, J. Rafelski, *Physics Reports*, **142**, 4 (1986); S. Soff, S. A. Bass, et al., *Physics Letters B* **471** (1999)

[26] E. Andersen et al.(WA97 Collaboration), *Phys. Lett. B* **449**, 401 (1999); M. K. Mitrovski et al. (NA49 Collaboration), *J. Phys. G* **32**, S43 (2006)

[27] T. Matsui, H. Satz, *Physics Letters B*, **178**, 4 (1986); F. Karsch, M.T. Mehr, H. Satz, *Z. Phys. C*, **37** (1988)

[28] M. C. Abreu et al. (NA50 Collaboration), *Physics Letters B*, **477** (2000)

[29] J.D. Bjorken, FERMILAB-PUB-82-59-THY and erratum (unpublished).

[30] C. Adler et al. (STAR Collaboration), *Phys. Rev. Lett.*, **90** (2003)

[31] J. Adams et al. (STAR Collaboration), *Nuclear Physics A*, **757** (2005)

[32] L. Adamczyk, et al. (STAR Collaboration), *Phys. Rev. Lett.* **113**, 142301 (2014).

[33] I. Vitev, T. Goldman and M. B. Johnson, *Phys. Rev. D* **74**, 054010 (2006); I. Vitev, A. Adil and H. van Hees, arXiv:hep-ph/0701188 (2007); R. Sharma, I. Vitev and B.-W. Zhang, *Phys. Rev. C* **80**, 054902 (2009); I. Vitev, *Braz. J. Phys.* **37**, 736 (2007).

[34] M. Nahrgang, J. Aichelin, P. B. Gossiaux and K. Werner, arXiv:1310.2218 (2013).

[35] A. Adil and I. Vitev, *Phys. Lett. B* **649**, 139 - 146 (2007).

[36] R. Sharma et al., *Phys. Rev. C* **80**, 054902 (2009).

[37] J. Adam, et al. (ALICE Collaboration),*J. High Energy Phys.* **JHEP03**, 081 (2016); J. Adam, et al. (ALICE Collaboration),*J. High Energy Phys.* **JHEP09**, 112 (2012).

[38] L. Adamczyk, et al. (STAR Collaboration), *Physical Review Letters* **118**, 212301 (2017).

[39] B. Abelev, et al. (ALICE Collaboration), *Phys. Rev. Lett.* **111**, 102301 (2013).

[40] Yu.L. Dokshitzera and D.E. Kharzeeva, *Phys. Lett. B* **519**, 199 - 206 (2001).

[41] S. Wicks, W. Horowitz, M. Djordjevic, M. Gyulassy, *Nucl. Phys. A* **784**, 426 (2007); A. Adil and I. Vitev, *Phys. Lett. B* **649**, 139 (2007); I. Vitev, A. Adil, H. van Hees, *J. Phys. G* **34**, S769 (2007); S. Cao, G.-Y. Qin, X.-N. Wang, *Phys. Rev. C* **93**, 024912 (2016).

[42] R. Snellings, *New Journal of Physics*, 13(5):055008, 2011

[43] S. Sarkar, H. Satz, B. Sinha (Editors), *The Physics of the Quark-Gluon Plasma: Introductory Lectures*, *Springer* (2010)

[44] Glauber, R.J., *Interscience*, **1** W.E. Brittin and L.G. Dunham (editors), 315 (1959)

[45] M.L. Miller, K. Reygers, S. J. Sanders, and P. Steinberg, *Ann. Rev. of Nuc. and Part. Sci.*, **57** 205-243 (2007)

[46] H. Hahn, E. Forsyth, et al. *Nucl. Inst. Meth. A* **499**, 245 (2003)

[47] J. G. Alessi, D. Barton et al., *Review of Scientific Instruments* **81**, 02A509 (2010)

[48] (Phobos Collaboration), *Nucl. Inst. Meth. A* **499**, 603 (2003)

[49] (BRAHMS Collaboration), *Nucl. Instr. Meth. A* **499**, 437 (2003)

[50] (PHENIX Collaboration), *Nucl. Instr. Meth. A* **499**, 469 (2003)

[51] (STAR Collaboration), *Nucl. Instr. Meth. A* **499**, 624 (2003)

[52] *An Upgrade Proposal from the PHENIX Collaboration*, arXiv:1501.06197v1

[53] M. Anderson, J. Berkovitz, et al., *Nucl. Instr. Meth. A* **499**, 659 (2003)

[54] H. Bichsel, *Nucl. Inst. and Meth. A* **562** (2006) 154197

[55] D. Beavis et al., The STAR Heavy Flavor Tracker Technical Design Report, available at: https://drupal.star.bnl.gov/STAR/starnotes/public/sn0600 (2011).

[56] G. Contin, L. Greiner, J. Schambach, et al, *Nucl. Instr. Meth. A* **907**, 60 (2018)

[57] G. Contin, *JINST*, PIXEL International Workshop, 11 C12068 (2016)

[58] Hao Qiu, *Nucl. Inst. and Meth. A* **931** (2014) 11411146

[59] R. Bellweid, R. Beuttenmuller et al. , *Nucl. Instr. Meth. A* **499**, 640 (2003)

[60] W.J. LLope, et al., *Nucl. Inst. Meth. A* **759**, 21 (2014)

[61] K. Meehan, *APS Far West Section Meeting*, University of California Davis, Oct. 2014

[62] C. Yang, X.J. Huang, AJ et al., *Nucl. Inst. Meth. A* **762** (2014)

[63] Karl Pearson, *Proceedings of the Royal Society of London*, 58 : 240242 (1895)

[64] S. Arrhenius, *The London, Edinburgh and Dublin Phil. Magazine and Journal of Science* **41** 237 (1896)

[65] D. Miskowiec et al. (E877 collaboration), *Nucl. Phys. A* **610**, page 237c (1996)

[66] J. Barrette et al. (E877 collaboration), *Physical Review Letters* **78** 2916 (1997)

[67] G. Agakishiev et al. (The STAR Collaboration), *Phys. Rev. C* **86**, 064902 (2012)

[68] R. Jefferson Porter and Thomas A. Trainor (for the STAR Collaboration), *J. Phys.: Conf. Ser.* **27** 98 (2005)

[69] R. Hanbury Brown and R.Q. Twiss, *The London, Edinburgh, and Dublin Philosophical Magazine and Journal of Science*, Series 7 **45** (1954)

[70] Sjöstrand et al., *Computer Physics Communications* **191**, June 2015, Pages 159-177

[71] R. L. Ray and A. Jentsch, *Phys. Rev. C*, **99** 024911 (2019)

[72] B. I. Abelev et al. (The STAR Collaboration), *Phys. Rev. C*, **79**, 034909 (2009)

[73] S. Shi, X. Dong, and M. Mustafa, *unpublished*, arXiv:1507.00614 (2015)

[74] T. Song, H Berrehrah et al., *Phys. Rev. C*, **92**, 014910 (2015)

[75] R. L. Ray and M. Daugherity, *J. Phys. G*, **35**, 125106 (2008)

[76] Bhattarai, *Two-particle Correlations of Identified Particles in heavy-ion Collisions at STAR*, PhD Thesis, The University of Texas at Austin (2016)

[77] Lanny Ray, *Run 4 Au+Au 200 GeV transverse momentum correlation analysis update*, BNL, May 17th, 2017 `https://drupal.star.bnl.gov/STAR/meetings/star-collaboration-meeting/jetcorr/yt-yt-update`

[78] Xiaolong Chen, *Centrality Definition in Run14 P16id for VPDMB30 and VPDMB-noVtx*, Sept. 2016 https://drupal.star.bnl.gov/STAR/system/files/cent_VPDMB30_and_noVtx.pdf

[79] J.G. Reid and T. Trainor, *Nucl. Inst. Meth. A*, **457** Iss. 1-2, 378-383 (2001)

[80] R. L. Ray and P. Bhattarai, *Nucl. Inst. Meth. A* **821** (2016)

[81] Heavy Flavor Tracker Conceptual Design Report: https://drupal.star.bnl.gov/STAR/starnotes/public/sn0600

[82] Manal Alruwaili, *Performance of the Heavy Flavor Tracker Detector in STAR experiment at RHIC*, PhD Thesis, Kent State University (2015)

[83] D. T. Kettler, D. J. Prindle and T. A. Trainor, Phys. Rev. C **91**, 064910 (2015).

[84] M. Tanabashi et al. (Particle Data Group), *Phys. Rev. D*, **98**, 030001 (2018).

[85] L. Adamczyk, et al. (STAR Collaboration), *Phys. Rev. Lett.* **121**, 229901 (2018).

[86] John A. Nelder, R. Mead, *Computer Journal* **7** (4): 308313 (1965)

[87] G. Agakishiev et al. (STAR Collaboration) *Phys. Rev. C* **85**, 014903 (2012)

[88] B. Abelev et al. (STAR Collaboration) *Phys. Rev. C* **94**, 014910 (2016)

[89] Rene Brun and Fons Rademakers, Proceedings AIHENP'96 Workshop, Lausanne, Sep. 1996, *Nucl. Inst. Meth. A* **389** (1997) 81-86. See also `http://root.cern.ch/`

[90] W. Cassing and E.L. Bratkovskaya, *Phys. Rev. C*, **78** (2008) 034919, arXiv:0808.0022 [hep-ph]; W. Cassing and E.L. Bratkovskaya, *Nucl. Phys. A*, **831** (2009) 215-242, arXiv:0907.5331 [nucl-th]

[91] T. Song, H. Berrehrah, D. Cabrera et al., *Phys. Rev. C*, **92** 014910 (2015)

[92] R. Rapp, P.B. Gossiaux, et al., *Nuclear Physics A*, **979** 21-86 (2018)

Vita

Alex Jentsch was born in 1989 in Houston, Texas. In high school he spent most of his time reading books, building things (and taking them apart to understand how they worked), and playing guitar with various bands. He started college at UT Austin in the Fall of 2007 to become an Electrical Engineer, while still expecting to do some music part-time. He became seriously interested in physics early in his undergraduate education and switched majors, graduating with a bachelor's in physics in May of 2012. Right after graduation, he began working in the UT heavy-ion group under Jerry Hoffmann building detectors as a laboratory assistant. He officially entered graduate school in Fall of 2014, shortly after marrying Claire. He began working on research with Lanny Ray, a research scientist in the group, while still working on the detector projects with Jerry. In 2016, Jerry passed away and Christina Markert graciously took Alex on as a student. He earned his PhD in May of 2019 and continues to do research in nuclear physics at Brookhaven National Laboratory in Long Island, NY.

Permanent address: alex.jentsch@utexas.edu

This dissertation was typeset with LaTeX[†] by the author.

[†]LaTeX is a document preparation system developed by Leslie Lamport as a special version of Donald Knuth's TeX Program.